# Unveiling Quantum Critical Phenomena in Selected Rare Earth Intermetallic Compounds

A Dissertation Presented for the

Doctor of Philosophy

Degree

The University of Tennessee, Knoxville

Lekhanath Poudel

May 2017

© by Lekhanath Poudel, 2017

All Rights Reserved.

Dedicated to my grandmother, Rama Devi Poudel.

# Acknowledgments

I would like to express my eternal gratitude to Dr. Andrew D. Christianson and Dr. David Mandrus for giving me the opportunity to work with them. For me, it was a great privilege to work at the University of Tennessee and Oak Ridge National Laboratory, and to interact closely with leading scientists in material synthesis and neutron scattering. I greatly appreciate Dr. Christianson for his clear guidance in this project and for the generosity to share his knowledge and experience – thank you very much for being so kind to me and for your patience and optimism in dealing with my countless problems over the course of this long project. I am very grateful to Dr. Mandrus for the inspirations and motivation to evolve as an independent researcher. He has been an excellent guiding figure to me with a great experience in nurturing the graduate students. I also had a great opportunity to collaborate with Dr. Jon Lawrence from Los Alamos National Laboratory. I very much appreciate his willingness to help in this project and a quick and detailed response to my questions. His experience and insight in the heavy fermion physics provided a solid foundation for this research and I received an incredible science education from him.

I am indebted to Dr. Nirmal Jeevi Ghimire for his help in material synthesis and for all the personal assistance during my graduate school. Also, many many thanks to Dr. Travis Williams and Dr. Ryan Baumbach for sharing the secrets of the Czochralski process and Dr. Jiaqiang Yan for his mentorship in material synthesis.

I owe sincere thanks to all my collaborators for the fruitful collaboration and their hardship in making this project successful. Thanks to Dr. Andrew E Payzant and Dr. Michael McGuire for the help with x-ray measurements, to Dr. Filip Ronning

for his assistance with low temperature heat capacity measurements, to Dr. Clarina De la Cruz and Dr. Ovidiu Garlia for helping me learn the methods of Rietveld refinement, to Dr. Andrew May for heat capacity and EDS measurements, to Dr. Saikat Mukhopadhyaya, Dr. David Parker, and Dr. David Singh for theoretical insights and calculations, and Dr. Michael Koehler and Dr. Veerla Keppens for RUS measurements. I want to express sincere acknowledgment to all the instrument scientists and scientific associates of HFIR, SNS, and NCNR for their assistance in carrying out the experiments. Thanks to Dr. Songxue Chi, Dr. Wei Tian, Dr. Tao Hong, Dr. Lou Santodonato, Dr. Jose A Rodriguez, Dr. Masaki Matsuda, Dr. Tao Hong, Dr. Huibo Cao, Dr. Daniel Pajerowski, Dr. Georg Ehlers and Dr. Barry Winn for the kind help and the trust in using their instruments. Special thanks to Dr. Yiming Qiu for his flexibility to work until the middle of the night during several neutron scattering experiments. I very much appreciate Harish Agrawal and the entire sample environment team of HFIR for their wonderful effort to initiate the Dilution Fridge measurements.

I wish to thank the senior postdocs of quantum condensed matter division. Thanks to Dr. Stuart Calder, Dr. Alice Taylor and Dr. Liusuo Wu for being great friends and mentors in neutron scattering measurements. I am very thankful to all the members of Mandrus group, particularly to Deepak Sapkota, Ganesh Pokharel, Dr. Ling Li, Amanda Haglund and Dr. Rupam Mukherjee for the teamwork and the fun environment in the lab.

Living away from the family was very difficult and painful, but thanks to the Nepali community in Knoxville for providing me a wonderful family environment. I owe a debt of gratitude to Deepak Bhandari, Bipana Dahal Bhandari, Pramila Bhattarai, Girish Upreti, Indu Upreti, Rajendra Timilsina, Anju Subedi for the kind hospitality in this foreign land. Also, many thanks to Naresh Osti for your brothership and everyday lunch conversations at the SNS.

My heartfelt acknowledgments goes to my parents for their unconditional love, the struggle to raise me, and all the endless encouragement throughout my life.

Thanks to my brothers Rajan and Sajjan, sister-in-law Yasoda, and all my relatives, the entire Poudel family and my in-laws. Also, it is hard to express adequate thanks to my sweet wife Draupada for the love, care, and indulgences during these years – thank you so very much for your understanding, love and patience in my life.

The work presented in this dissertation resulted from an extensive collaboration with many people from Oak Ridge National Laboratory, The University of Tennessee, Argonne National laboratory, Los Alamos National Laboratory, NIST Center for Neutron Research, National High Magnetic Field Laboratory, and the University of Missouri. Most of my collaborators and myself were supported by the Scientific User Facilities Division, Office of Basic Energy Sciences, U.S. Department of Energy (DOE), which also supports the use of the neutron instruments at HFIR and SNS. The use of the advanced photon source at Argonne National Laboratory was supported by the U. S. Department of Energy, Office of Science, Office of Basic Energy Sciences, under Contract No. DE-AC02-06CH11357. Some of my ORNL collaborators were supported by the U. S. Department of Energy, Office of Science, Basic Energy Sciences, Materials Sciences and Engineering Division. Work performed at the National High Magnetic Field Laboratory is supported by National Science Foundation (NSF). Work at the University of Missouri was supported by DOE through the S3TEC Energy Frontier Research Center Award No. DE-SC0001299/DE-FG02-09ER46577. Some of the laboratory XRD work was conducted at the Center for Nanophase Materials Sciences, which is a DOE Office of Science User Facility.

# Abstract

The quantum critical phenomenon of $CeCu_{6-x}Au_x$ ($x$ =0.1) [gold-doped cerium copper six] presents a host of intriguing puzzles: In particular, the dynamic susceptibility showing $E/T$-scaling with a fractional exponent of 0.75 is a surprise and is clearly inconsistent with the established approach developed by Hertz, Millis, and Moriya (HMM). Interestingly, the phase diagram of $CeCu_{6-x}Au_x$ [gold-doped cerium copper six] also suggests a zero temperature structural phase transition, raising the possibility of a structural quantum critical point (QCP). To provide a further insight into the unconventional quantum criticality and to investigate the possibility of a structural QCP, related materials including $CeCu_{6-x}T_x$ ($T$ = Ag, Pd) [palladium/silver-doped cerium copper six] and $LaCu_{6-x}Au_x$ [gold-doped lanthanum copper six] have been studied.

This comprehensive study, largely based on neutron scattering measurements, shows that the series $CeCu_{6-x}T_x$ ($T$ = Ag, Pd) [palladium/silver-doped cerium copper six] are magnetically identical to the $CeCu_{6-x}Au_x$ [gold-doped cerium copper six] despite considerable differences in the doping dependence of the structural properties. Furthermore, in $CeCu_{6-x}Ag_x$ [silver-doped cerium copper six], the dynamic susceptibility fits well with a single phenomenological equation that yields $E/T$ scaling with a similar anomalous exponent, $\alpha$ [$alpha$] = 0.72(1). The key result is rather than a single fluctuation there are two competing magnetic fluctuations that correspond to an incommensurate and a commensurate wave-vector. Only the incommensurate fluctuations appear to go critical at the QCP. While the total dynamic susceptibility displays an unconventional $E/T$ scaling, the critical part of

the dynamic susceptibility is consistent with the framework of the conventional HMM model suggesting that the exotic physical behavior is the consequence of a competing noncritical term in the spectrum.

In $LaCu_{6-x}Au_x$ [gold-doped lanthanum copper six], the orthorhombic-monoclinic structural phase transition temperature is suppressed linearly with Au-doping suggesting the presence of a zero-temperature structural phase transition. Consistent with this observation, the heat capacity is enhanced at the critical composition. First principles calculations indicate that the structural instability is elastic in nature. This suggests a new type of QCP in $LaCu_{6-x}Au_x$ [gold-doped lanthanum copper six] where quantum zero point motion of atoms suppresses an elastically ordered phase of matter.

# Table of Contents


**1 Overview of the Thesis** **1**

**2 Introduction** **5**

2.1 Quantum Critical Point . . . . . 5

2.2 Quantum criticality in Heavy fermion systems . . . . . 8

2.3 Spin Density Wave Quantum Critical Point . . . . . 11

2.4 Properties of $CeCu_{6-x}Au_x$ . . . . . 14

2.5 Quantum Criticality in $CeCu_{6-x}Au_x$ . . . . . 18

2.6 Quantum Critical Point in $CeCu_{6-x}T_x$ ($T$ = Ag, Pd, Pt, Sn) . . . . . 23

2.7 Understanding $E/T$-scaling . . . . . 25

2.7.1 Local QCP . . . . . 25

2.7.2 Strong-coupling QCP . . . . . 27

2.7.3 Dissipative XY QCP . . . . . 29

**3 Research Techniques** **31**

3.1 Material Synthesis . . . . . 31

3.1.1 Arc-melting . . . . . 32

3.1.2 Czochralski Process . . . . . 32

3.2 Neutron Scattering . . . . . 38

3.2.1 Elastic Neutron Scattering . . . . . 42

3.2.2 Magnetic scattering . . . . . 43

3.3 Instrumentation . . . . . 46

3.3.1 Triple axis Spectrometers . . . 47
3.3.2 Time of flight Spectroscopy . . . 49

**4 Phase diagrams of $CeCu_{6-x}T_x$($T$ = Ag, Pd) 52**
4.1 Introduction . . . 53
4.2 Experimental Details . . . 57
4.3 Results . . . 60
4.3.1 Characterization . . . 60
4.3.2 Neutron & x-ray Diffraction . . . 60
4.3.3 Structural Phase Transitions . . . 62
4.3.4 First Principles Calculations . . . 66
4.3.5 Magnetic Phase Transitions . . . 71
4.4 Discussion . . . 77
4.5 Conclusions . . . 79

**5 Elastic QCP in $LaCu_{6-x}Au_x$ 81**
5.1 Introduction . . . 82
5.2 Experimental Details . . . 84
5.3 Results . . . 86
5.3.1 Neutron/x-ray diffraction . . . 86
5.3.2 Heat capacity . . . 96
5.3.3 Density Functional Theory Calculations . . . 96
5.4 Discussion . . . 105
5.5 Conclusions . . . 108

**6 Quantum criticality of $CeCu_{6-x}Ag_x$ 109**
6.1 Introduction . . . 109
6.2 Experimental Details . . . 112
6.3 Results . . . 113
6.3.1 Dynamic Critical Scattering of $CeCu_{5.8}Ag_{0.2}$ . . . 118

6.3.2 $E/T$-scaling . . . . . 118
6.3.3 Unveiling Competing Fluctuations . . . . . 128
6.4 Conclusions . . . . . 137

**7 Conclusions and Overview** **138**

**Bibliography** **142**

**Appendix** **162**

**List of Publications** **163**

**Vita** **165**

# List of Tables


2.1 Temperature dependence of the thermodynamic observables near an HMM QCP. Symbols $\alpha_{cr}$, $C_{cr}$, $\rho_{cr}$ and $\Gamma_{cr}$ represent the critical part of thermal expansion, heat capacity, resistivity and Grüneisen ratio, respectively. Table is taken from Ref. [1]. . . . . 12

4.1 Lattice parameters and atomic coordinates at room temperature of a) $CeCu_6$, b) $CeCu_{5.7}Ag_{0.3}$ and c) $CeCu_{5.7}Pd_{0.3}$ obtained from Rietveld refinements of the structural model for the synchrotron x-ray measurements (See Fig. 4.1). . . . . 54

4.2 Structural parameters of $CeCu_{6-x}T_x$ ($T$ = Ag, Pd) extracted from diffraction measurements at room temperature. The lattice parameters were obtained from Rietveld analysis. . . . . 61

4.3 The relative energies of several configurations for Ag and Pd doping. . 67

4.4 Compositional dependence of the magnetic wave vector in $CeCu_{6-x}Ag_x$ and $CeCu_{6-x}Pd_x$. . . . . 69

4.5 Basis vectors from representational analysis of space group $Pnma$ with $\mathbf{k}$ = (0.62, 0, 0.3). The Ce-site is separated into four orbits given by 1: (0.2586, 0.25, 0.5636), 2: (0.2414, 0.75, 0.06360), 3: (0.7414, 0.75, 0.4364), 4: (0.7586, 0.25, 0.9364). The decomposition of the magnetic representation for each of the four orbits is $\Gamma_{Mag} = 1\Gamma_1^1 + 2\Gamma_2^1$. Symbols $m_{\parallel a}$ $m_{\parallel b}$ $m_{\parallel c}$ denote the projection of the magnetic moment along the $a$, $b$ and $c$-axis respectively. . . . . 72

5.1 Room temperature structural parameters of a) $LaCu_6$ and b) $LaCu_{5.7}Au_{0.3}$. The parameters are obtained from the fits to the diffraction patterns shown in Fig. 5.7. . . . . 97

5.2 The goodness of fit parameters at different stages of Rietveld refinement of $LaCu_{5.7}Au_{0.3}$. The best set of parameters (shown in bold) was obtained when the Au atoms were constrained to the Cu2 site. . . . . 98

# List of Figures

2.1 Examples of phase diagrams showing (a) a classical phase transition and (b) a QCP. The classical phase transition occurs as the thermal fluctuations lead to a random orientation of the spins. A QCP occurs as a non-thermal parameter $g$ tunes the phase transition to occur at zero temperature. Dashed lines indicate the boundary of the quantum critical region. The quantum critical region near the QCP is dominated by fluctuations that are quantum mechanical in nature. This figure is taken from ref. [2]. . . . . 6

2.2 Doniach phase diagram. When the Kondo energy scale is smaller than the RKKY energy scale ($T_K < T_{RKKY}$), the ground state is antiferromagnetically ordered. When the Kondo energy scale overcomes the RKKY energy scale($T_K > T_{RKKY}$), a non-magnetic heavy fermion state is formed. A QCP occurs between these two regimes. Figure taken from Ref. [3]. . . . . 12

2.3 Room temperature crystal structure of $CeCu_6$ reproduced using the parameters from Ref. [4]. . . . . 15

2.4 Phase diagram of $CeCu_{6-x}Au_x$ showing structural and magnetic phase transitions. The structural transition temperatures ($T_S$) decrease upon alloying with Au. The extrapolation of $T_S$ with $x$ suggests that the monoclinic structure is completely suppressed near $x \approx 0.13$. Antiferromagnetic order emerges with Au-substitution with a magnetic QCP occurring at $x \approx 0.1$. $T_S$ and $T_N$ are taken from several sources[5, 6, 7, 8]. . . . . 19

2.5 Two dimensional contour plots showing the dynamic magnetic correlations in (a) the parent compound $CeCu_6$, (b) QCP composition $CeCu_{5.9}Au_{0.1}$, and (c) the magnetically ordered composition ($T_N \approx 0.2$ K) $CeCu_{5.8}Au_{0.2}$. $CeCu_6$ and $CeCu_{5.8}Au_{0.2}$ were measured with an energy transfer of $E = 0.15$ meV. $CeCu_{5.9}Au_{0.1}$ was measured with $E = 0.1$ meV. For all compositions, a similar diffuse pattern of magnetic correlations is observed with the rod shaped structure. This plot is taken from Ref. [9]. . . . . 21

2.6 Constant energy scans along [0 0 1] for (a) the parent compound $CeCu_6$ scanned at $E = 0.15$ meV (b) QCP composition $CeCu_{5.9}Au_{0.1}$ scanned at $E = 0.1$ meV. (c) A magnetically ordered composition ($T_N \approx 0.2$ K) $CeCu_{5.8}Au_{0.2}$ scanned at $E = 0.15$ meV. This plot is taken from Ref. [9]. . . . . 22

2.7 Phase diagram of $CeCu_{6-x}Ag_x$ showing the dependence of magnetic order with field and Ag composition. At zero filed, a magnetic QCP in $CeCu_{6-x}Ag_x$ occurs at $x = 0.2$. Taken from Ref. [10]. . . . . 24

3.1 A *Compact Arc Melter MAM-1* commercially available from Edmund Bühler GmbH. The picture is taken from the web page of Edmund Bühler GmbH. . . . . 33

3.2 The tri-arc arrangement in the synthesis laboratory of the Mandrus Research group. . . . . 34

3.3 Single crystal of $CeCu_{5.9}Pd_{0.05}$ grown by the Czochralski process. The diameter of top portion of the crystal is intentionally made as small as possible. The crystal below the neck is verified to be a single crystal from neutron diffraction measurements. . . . . 37

3.4 Scattering triangle showing geometry of neutron scattering. The neutron is deflected at an angle of $2\theta$ from the incident direction. For elastic scattering, $|\mathbf{k_i}| = |\mathbf{k_f}|$. . . . . 39

3.5 Schematic digam of HB3 spectrometer at HFIR of ORNL. . . . . 48

3.6 Schematic of the cold neutron chopper spectrometer (CNCS) at the SNS of ORNL, Oak Ridge, Tennessee. Picture taken from Ref. [11] . . . . . 50

4.1 a) Room temperature x-ray powder diffraction pattern (black dots) plotted along with the Rietveld refinement (red line) for a) $CeCu_6$, b) $CeCu_{5.7}Ag_{0.3}$ and c) $CeCu_{5.7}Pd_{0.3}$. Vertical green marks are the positions of the structural reflections. The diffraction patterns were collected at beamline 11-BM at the advanced photon source (APS) of Argonne National Laboratory (ANL). The values of the refined parameters are tabulated in tables 4.1 and 4.2. The difference ($I_{obs}$ – $I_{calc}$) is offset for clarity. Note: the x-axis (Q) is in a logarithmic scale. 55

4.2 Inverse susceptibilities of $CeCu_{6-x}T_x$ (T = Ag, Pd) showing Curie-Weiss behavior. The red solid line is a Curie-Weiss fit to the data. The effective moments estimated from the Curie-Weiss fits are given in the text. . . . . 58

4.3 The structural transition of $CeCu_{5.95}Ag_{0.05}$ characterized using a) powder x-ray diffraction with wavelength, $\lambda \approx 1.54$ Å: The (122), (220) and (221) structural peaks in the orthorhombic phase split in the monoclinic phase as described in the text. Note that peaks indexed as (h 0 l) or (0 k l) in the orthorhombic phase are unaltered, aside from a change of indexing, by the monoclinic distortion. b) Single crystal neutron diffraction with $\lambda \approx 1.003$ Å: The structural peak (2 2 0) of orthorhombic phase splits into two structural peaks (2 0 2) and (– 2 0 2) of monoclinic phase at $T_S$. c) RUS: the square of the resonant frequencies change slope at $T_s$. A vertical line in the plot shows $T_s$. All measurements indicate that the structural phase transition takes place in $CeCu_{5.95}Ag_{0.05}$ at $T_S \approx 125(5)$ K. . . . . 63

4.4 Monoclinic order parameter $((a_m c_m \cos(\beta))^2)$ of $CeCu_{5.92}Ag_{0.08}$ obtained from neutron diffraction measurements. An extrapolation of the order parameter gives $T_s$ = 62(3) K. A continuous change in the monoclinic order parameter is observed near $T_S$. . . . . 64

4.5 The phase diagrams of a) $CeCu_{6-x}Pd_x$ and b) $CeCu_{6-x}Ag_x$. The concentration for the occurrence of the magnetic QCP is taken to be the same as in [12, 13] and is $x_{QCP} \approx 0.2$ for $CeCu_{6-x}Ag_x$ and $x_{QCP} \approx 0.05$ for $CeCu_{6-x}Pd_x$. In $CeCu_{6-x}Ag_x$, the termination of the structural phase transition occurs at $x_S \approx 0.1$. No suppression of the structural phase transition was observed in $CeCu_{6-x}Pd_x$ for $x \leq 0.4$. . . . . 65

4.6 The calculated DOS of $CeCu_6$ in the orthorhombic and monoclinic structures. . . . . 67

4.7 a) The magnetic reflection at Q = 0.480(3) from a polycrystalline sample with a composition of $CeCu_{5.75}Pd_{0.25}$. The inset shows the magnetic reflection from a a single crystal of $CeCu_{5.85}Pd_{0.15}$ near the wave vector **Q** = (0.6243(1) 0 0.2503(1)). b) and c) Single crystal diffraction measurement of the the (0.62 0 0.3) magnetic reflection of $CeCu_{5.25}Ag_{0.75}$ along (0.62 0 L) and (H 0 0.3) at 0.05 K. The red line is a Gaussian fit to the data constrained by the instrumental resolution. The horizontal black lines are the calculated instrumental resolution. . 68

4.8 Temperature dependence of the intensity of the magnetic peak ((0.62 0 0.25) for $CeCu_{6-x}Pd_x$ and (0.64 0 0.3) for $CeCu_{6-x}Ag_x$) normalized to the structural (0 0 2) peak in (a-e) $CeCu_{6-x}Pd_x$ and (f-j) $CeCu_{6-x}Ag_x$. The red line is a fit to the the data with a power law equation of the form $y = y_0 + A(T - T_N)^{2\beta}$. $\beta$ was fixed to the mean field value of 0.5 and $T_N$ was allowed to vary in order to estimate the transition temperature. The estimated values of $T_N$ are a) 1.20(1) K, b) 1.07(2) K, c) 0.88(3) K, d) 0.52(1) K, e) 0.43(1) K, f) 0.74(2) K, g) 0.51(1) K, h) 0.38(1), i) 0.24(1) K, j), and 0.14(1) K. . . . . 73

4.9 a) The magnetic structure of $CeCu_{5.5}Ag_{0.5}$. Each box represents a structural unit cell that contains four Ce-atoms as indicated by the red spheres. The length and direction of the arrows shows the magnitude and direction of the moment, respectively. All Ce-moments point along the $c$-axis of the orthorhombic unit cell. The amplitude of the moment is modulated along the wave vector (0.62 0 0.3). The observed and calculated intensities for the magnetic structure is displayed in b) and c) for $CeCu_{5.5}Ag_{0.5}$ and $CeCu_{5.6}Pd_{0.4}$ respectively. d) Compositional dependence of the ordered moments in $CeCu_{6-x}T_x$ ($T$ = Ag, Pd). The magnetic structure determined for $CeCu_{5.5}Ag_{0.5}$ and $CeCu_{5.6}Pd_{0.4}$, was assumed to be the same for the remaining members of each series. The QCP occurs at $x = 0.05$ for $CeCu_{6-x}Pd_x$ and $x = 0.2$, for $CeCu_{6-x}Ag_x$. A point shown as a triangle indicates a composition for which the magnetic moment was not completely saturated and thus the full moment value will be somewhat larger. . . . . 74

5.1 Orthorhombic lattice parameters (a) $a$, (b) $b$, (c) $c$ in $LaCu_{6-x}Au_x$ at room temperature. The lattice parameters were obtained from the Rietveld refinements of laboratory x-ray diffraction measurements. The compositions $x = 0$ and 0.1 were refined in monoclinic structure (space group: $P2_1/c$). All other compositions ($x \geq 0.2$) were refined to the orthorhombic phase (space group: $Pnma$). . . . . 85

5.2 Temperature dependence of the monoclinic lattice parameters (a) $a_m$, (b) $b_m$, (c) $c_m$, and (d) $\beta_m$ in $LaCu_{6-x}Au_x$. . . . . 87

5.3 (a) X-ray diffraction data showing the splitting of selected Bragg peaks at the structural transition in $LaCu_{5.8}Au_{0.2}$. The following indexing scheme describes the splitting of the peaks: (122)→(22±1), (220)→(20±2), (221)→(21±2). The peak between (21±2) at low temperature is the orthorhombic (303) reflection, which becomes the monoclinic (033) reflection (no splitting). The vertical dotted line indicates the temperature where the peaks begin to separate. Note: Each pixel represents a triangulation-based linear interpolation of the measurement performed with 10 K steps in temperature. (b) The temperature dependence of $\cos^2\beta_m$ in $LaCu_{6-x}Au_x$ determined from neutron diffraction data. $\cos^2\beta_m$ varies smoothly with temperature near $T_S$. For each composition, $T_S$ was estimated from a linear extrapolation (red line) of $\cos^2\beta_m$. . . . . 90

5.4 The monoclinic $ac$ plane (dotted parallelogram) showing the geometry of a shear. The solid rectangle is the extrapolation of monoclinic $ac$ plane when $\theta = 0$ (no shear). . . . . 91

5.5 Structural phase diagram of $LaCu_{6-x}Au_x$. The open circle represents the point where no structural phase transition is observed above 2 K. The statistical error bars for $T_S$ are smaller than the symbol size. Linear extrapolation of $T_S$ with temperature indicates $x_c = 0.3$. . . . 92

5.6 The variation of $\cos^2\beta_m$ in $LaCu_{6-x}Au_x$ with Au-composition at 20 K. An extrapolation (dotted red line) of $\cos^2\beta_m$ with Au-composition indicates that the suppression of the monoclinic ground state occurs at $x = 0.28$. . . . . 93

5.7 Synchrotron x-ray diffraction pattern of (a) $LaCu_6$, (b) $LaCu_{5.7}Au_{0.3}$ at 300 K. The fit (black) to the diffraction pattern (red) is obtained with the Rietveld analysis. The vertical green bars represent structural Bragg peaks. $I_{calc} - I_{obs}$ is offset for clarity. Note: x-axis is in logarithmic scale. . . . . 94

5.8 (a) Heat capacity data showing $T^3$ behavior at low temperature for $LaCu_6$ ($x = 0$) and $LaCu_{5.7}Au_{0.3}$ ($x_c$=0.3). The solid lines are a fit to the data of the form $C = \gamma T + \beta T^3$. (b,c) The variation of (b) $\beta$ and (c) $\gamma$ obtained from the fits to the heat capacity measurements as a function of Au-composition. The vertical dotted lines indicate the critical composition ($x_c$ = 0.3). In all panels, the values are reported per formula unit. . . . . 95

5.9 Heat capacity measurement of $LaCu_{5.75}Au_{0.25}$. No anomaly is observed near the structural phase transition ($T_S$ = 80(5) K). Inset is a zoom near $T_S$ . . . . . 98

5.10 Heat capacity measurement of $LaCu_{5.7}Au_{0.3}$ showing Debye-$T^3$ behavior at low temperatures (0.7 K ≥ T ≥ 3.5 K). The straight line (red) is the fit of the equation $C/T = \gamma + \beta T^2$ to the data. . . . . 99

5.11 Calculated phonon dispersions of $LaCu_6$ with the $Pnma$ crystal structure. The imaginary phonon mode frequency from Γ to $X$ indicates the instability of the orthorhombic structure. . . . . 101

5.12 Calculated phonon dispersion of $LaCu_6$ with monoclinic (space group: $P2_1/c$) crystal structure. All the phonon modes are stable with monoclinic structure. . . . . 102

5.13 Electronic DOS of $LaCu_6$ in orthorhombic and monoclinic phases. . . . 103

5.14 Fermi surfaces of $LaCu_6$ in orthorhombic and monoclinic phases. . . . 104

6.1 (a) A Single crystal of $CeCu_{5.8}Ag_{0.2}$ synthesized by the Czochralski process. (b) Single crystal mounted in a copper sample holder prior to the INS measurement. The sample is protected by an extra cover of copper foil which acts as a heat shield to ensure the temperature of the sample is uniform. (c) Elastic neutron scattering measurement showing structural Bragg peaks in (h 0 l) scattering plane. All major Bragg peaks are visible and can be indexed. (d) Heat capacity at zero magnetic field displaying a divergence of C/T at lower temperatures. The measurement closely agrees with previous studies[14]. Solid lines are the fit of functions shown in the Legend to the data. . . . . 111

6.2 (a) Constant energy slice at 50 K averaged over the energy range e =[0.2,0.4] and $k$ =[-0.2,0.2]. The scattering is mostly attributed to the background from different sources in addition to weak magnetic scattering. The scattering at $\mathbf{Q}$ = (1 0 ± 1), $\mathbf{Q}$ = (1 0 2), $\mathbf{Q}$ = (2 0 ±1) and $\mathbf{Q}$ =(0 0 2) is due to the low frequency tail of the structural Bragg peaks. (b) The temperature dependence of cuts along the energy axis at the wave-vector $\mathbf{Q}$ = (0 0 1.2). The intensity of the scattering is independent of temperature. The $\mathbf{Q}$ independent background is taken from this wave-vector. (c) Cuts along the energy axis at the wave-vectors $\mathbf{Q}$ = (1 0 1.2) and (1 0 2.5) at 50 K. The cuts at two wave-vectors are similar. (d) The cuts along energy axis near the structural Brag peak $\mathbf{Q}$ = (2 0 0). The intensity of the scattering increases at higher temperature due the thermal population of phonons. . . . . 114

6.3 (a) Constant energy slice at 50 K. Note: this plot is a copy of Fig. 6.2(c). (b) A constant energy slice obtained by replicating the cuts along L-axis. (c) Cuts of constant energy slices(a,b) along the H-axis near (1 0 0). (d) Cuts of the constant energy slices (a,b) along the L-axis near (1 0 0). . . . . 115

6.4 Constant energy slices of the neutron scattering data for $CeCu_{5.8}Ag_{0.2}$ in (h 0 l) scattering plane. (a-d) displays the energy dependence of the scattering at 0.25 K, and (e-h) displays the temperature dependence at 0.1 meV. In all panels, the data collected at 50 K is used as the background and is subtracted from the data. Each pixel in the plot represents the integrated intensity in the area of dimension $(0.05)^2$ r.l.u.$^2$. . . . . 117

6.5 (a-c) Scaling analysis of the imaginary part of dynamic susceptibility in different regions of reciprocal space. The solid lines are the fit of the phenomenological equations 6.1 to the data. (d) The fit yields the $\mathbf{q}$-dependent term $\theta(q)$. Near $\mathbf{q} = 0$, $\theta(q) \approx \mathbf{q}^2$ (red line). (e) Dynamic susceptibility at 0.25 K scaled as a function of $E/\theta(q)$. As anticipated from equation 6.3, the susceptibility at different $\mathbf{Q}$s collapse onto a single curve showing $E/\theta(q)$-scaling. The solid line is the fit of equation 6.3 to the data. (f) The variation in the goodness of fit parameter $\chi^2$ with the scaling exponent $\alpha$. The best fit is obtained near $\alpha$=0.72. . . . 120

6.6 Scaling analysis of equation 2.15 to the data. (a-f) Measurement at different temperatures scaled as a function of $E/T$. The solid lines are the fit of equation 2.15 to the data. The fitted lines at different temperatures converge only at the center of the scattering, $\mathbf{Q}$ = (1 0 0) and deviate away from the center. The $\mathbf{Q}$-dependent function in equation 2.15 is considered as a fitting parameter. (g) The variation of $f(\mathbf{Q}-\mathbf{Q}_0)$ as a function of $\mathbf{Q}-\mathbf{Q}_0$. Near $Q_0$, the function is quadratic in $\mathbf{Q}-\mathbf{Q}_0$. (h) The goodness of fit parameter ($\chi^2$) as a function of scaling exponent, $\alpha$. The best goodness of fit parameter is obtained when $\alpha$ = 0.73(1). . . . . 122

6.7 Scaling analysis with reference to the strong-coupling model. Solid lines represent a fit of equation 2.24 to the data. The **Q**-dependent function S($\mathbf{Q}-\mathbf{Q}_0$) is taken as a fitting parameter. Panels(a-f) represent different regions of the magnetic scattering. . . . . 123

6.8 Dependence of S($\mathbf{Q}-\mathbf{Q}_0$) on ($\mathbf{Q}-\mathbf{Q}_0$). The values of S($\mathbf{Q}-\mathbf{Q}_0$) were obtained from a global fit of equation 2.20 to the data as presented in FIg. 6.7. . . . . 124

6.9 (a) Cuts along (0 1 0) axis at **Q** = (1 0 0) at two energy transfers normalized to the peak value. A fit of simple Lorentzian function was performed to estimate the widths of the peaks. The change in the widths of the cuts is not expected from the XY-dissipation model. (b) The variation of widths of the cuts with energy transfers. The widths increase with energy. . . . . 125

6.10 Scaling analysis of Ag with reference to the XY-dissipation model. Each panel corresponds to the wave-vectors in different regions of the scattering. The y-axis is the dynamic susceptibility scaled by $F_u(E/E_c) \propto \frac{1}{\sqrt{1+(E/E_c)^2}}$. The **Q** -dependent function, $F(\mathbf{Q}-\mathbf{Q}_0)$, is fitted as a parameter. The dotted line represents hyperbolic tangent of $E/2T$. 126

6.11 Variation of $F(\mathbf{Q}-\mathbf{Q}_0)$ obtained from the fit of the equation 2.29. The fits are as presented in Fig. 6.10. The solid red line is fit of the Lorentzian function. . . . . 127

6.12 Reciprocal space geometry showing the relative orientation of correlation length vector $\xi$ with the **Q**. $\xi_\parallel$ and $\xi_\perp$ are the parallel and perpendicular components of correlation length vector. The parallel axis is at an angle $\theta_0$ from reciprocal [H 0 0] axis (crystallographic $a$ axis in real space). The fit of constant energy slice yields $\theta_0$ = 71°. The magnetic correlation is centered at $\mathbf{Q}_0 = (Q_{h0},\ 0,\ Q_{l0}$. Wave-vector $\mathbf{Q} = (Q_h,\ 0,\ Q_l)$ is a variable in the scattering pane. . . . . 130

6.13 (a) Constant energy slice at 0.25 K averaged over an energy range e =[0.15,0.25] after a 50 K background subtraction. (b) The parametrization of slice as a superposition of two independent magnetic fluctuations shown in (c) and (d). (c) Magnetic fluctuation centered at the **Q** =[0.65 0 0.3] and symmetry related regions. Panel (d) The magnetic fluctuation centered at **Q** = (1 0 0). (e,f) Cuts along (e) (H 0 0) and (f) (0 0 L) axis each integrated within E = [0.15,0.25] meV. The red line is the fit of two Lorentzian functions described in the text. The blue and green dotted lines represent the contribution from the magnetic fluctuations centered at commensurate and incommensurate wave-vectors, respectively. . . . . 131

6.14 (a) Constant energy slice at 0.25 K cut within the energy interval of e = [0.075,0.275]. A background collected at 50 K is subtracted from the data. (b,c) The best fit of equation 6.4 to the **Q** slice obtained by (b) constraining the correlation lengths to differ by an order of magnitude (c) without any constrains in the correlation lengths. (d,e) Plots showing one dimensional cuts of slice (a,b,c). The black circles represent slice shown in (a). The red and blue lines represent the cuts of the pattern shown in (b) and (c), respectively. . . . . 132

6.15 Spectral weights and the real space correlation lengths extracted from the fit of a two dimensional Lorentzian function. (a) The spectral weight of the fluctuations centered at an incommensurate wave-vector $\mathbf{Q}_1$ = (0.65 0 $\pm$0.3) (b,c) Real space correlation lengths along (b) parallel and (c) perpendicular to the axis. (d) Spectral weight of the non-critical fluctuations centered at $\mathbf{Q}_2$ = (1 0 0). Subplot (e) and (f) are the real space correlation lengths along the $a$ and $c$-axis of crystal structure. . 134

6.16 Scaling analysis of the critical dynamic susceptibility with reference to the conventional approach provided by HMM. The critical part of the dynamic susceptibility is extracted from the fit of a sum of two overlapping Lorentzians as shown in Fig. 6.13. . . . . 136

# Abbreviations

| | |
|---|---|
| QCP | Quantum Critical Point |
| SDW | Spin Density Wave |
| INS | Inelastic Neutron Spectroscopy |
| HMM | Hertz-Millis-Moriya |
| LGW | Landau-Ginzburg-Wilson |
| TOF | Time of Flight |
| TAS | Triple Axis Spectrometer |
| ORNL | Oak Ridge National Laboratory |
| HFIR | High Flux Isotope Reactor |
| SNS | Spallation Neutron Source |
| CNCS | Cold Neutron Chopper Spectrometer |
| RUS | Resonant Ultrasound Spectroscopy |
| EDS | Energy-Dispersive x-ray Spectroscopy |
| ANL | Argonne National Laboratory |
| APS | Advanced Photon Source |
| LDA | Local Density Approximation |
| DMFT | Dynamic Mean Field Theory |
| RKKY | Ruderman-Kittel-Kasuya-Yosida |
| SCR | Self Consistent Renormalization |
| SQCP | Structural Quantum Critical Point |
| EDMFT | Extended Dynamical Mean Field Theory |
| MPMS | Magnetic Property Measurement System |
| PPMS | Physical Property Measurement System |

| | |
|---|---|
| GGA | Generalized Gradient Approximation |
| DOS | Density of State |
| NSP | Non-Spin Polarized |
| SP | Spin Polarized |
| IR | Irreducible Representation |
| DFT | Density Functional Theory |
| PBE | Perdew, Burke and Enzerhof |
| LAPW | Linearized Augmented Planewave |

# Chapter 1

# Overview of the Thesis

Matter exists in different phases and the transition from one phase to another is a common phenomenon in our daily life. For example, ice melts into a liquid when heated, and a permanent magnet loses its magnetization above a critical temperature. The phase transitions that we experience in everyday life are driven by the thermal fluctuations of atoms or spins. The phenomenon of a continuous thermal phase transition can be explained by classical statistical mechanics, which are also called *classical phase transitions*. Several aspects of a classical continuous phase transition can be explained by a conventional approach proposed by Landau-Ginzburg[15]. This approach is based on the idea of an order parameter – a local observable quantity that is finite in the ordered state and measures the relative order of the ordered state near the critical point. The order parameter is zero in the disordered phase. Near the critical point, the order parameter is small; therefore, the thermodynamic potential can be written as a Taylor expansion of the order parameter.

While the Landau-Ginzburg approach provides an analytical way to characterize a phase transition, it fails to describe the temperature dependence of the thermodynamic quantities in many systems. One of the major weaknesses of this approach is that the role of long wavelength fluctuations is completely ignored in the

critical phenomenon. However, at the continuous phase transition, the divergence of correlation length is expected and the collective critical behavior depends on the correlations integrated over an infinitely large region. This issue was partly addressed by a renormalization group approach proposed by Wilson, incorporating the role of long wavelength fluctuations up to the correlation lengths[16]. The theory of phase transition developed by Landau, Ginzburg and Wilson (LGW) is still widely used to understand thermal phase transitions.

Using the idea of the Landau-Ginzburg theory and the renormalization methods proposed by Wilson, Hertz later pioneered the theoretical foundation for the *Quantum phase transition*[17]. Unlike the classical phase transition, quantum phase transitions are driven by quantum fluctuations and take place in the absence of thermal energy (i.e., at zero temperature). Of particular interest here is the idea of a continuous quantum phase transition that occurs at a quantum critical point (QCP). Theoretical understanding of the antiferromagnetic quantum critical point (QCP) was further advanced by Millis[18, 19, 20]. Moriya developed a self-consistent renormalization (SCR) method to study the properties of QCPs at finite temperature[21, 22]. The collective version of the approach suggested by Hertz, Millis, and Moriya (HMM) is considered the conventional model of a metallic QCP.

In the past few decades, many magnetic systems that host a QCP have been studied, and it has been clear from the experiments that several aspects of QCPs do not fit into the paradigm established by HMM model[1]. In the meantime, a number of alternative theoretical perspectives have been developed for a more complete understanding of the quantum critical phenomenon. Despite considerable interest in understanding QCPs, the situation even within the limited scope of Ce-based heavy fermion QCPs is decidedly unclear. For instance, in the heavy fermion system $CeCu_{6-x}Au_x$, the standard approach developed by HMM fails to account for experimental observation[23, 24, 25]. In particular, the fractional exponent $\alpha = 0.75$ in the $E/T$ scaling of the dynamic susceptibility in $CeCu_{6-x}Au_x$ ($x = 0.1$) is clearly inconsistent with the conventional HMM model[24, 25]. While there are a

few different theoretical interpretations of this unconventional behavior, a broader experimental assessment in these systems is essential. Another important issue is that previous studies were focused within the limited examples of the magnetic QCPs and other areas of QCPs that can provide a much broader context to the quantum critical phenomenon remain unexplored. To fill some of these voids, this dissertation seeks to solve some of the puzzles in understanding the quantum critical phenomenon.

This dissertation provides a comprehensive study of the structural and magnetic properties of the heavy fermion series $CeCu_{6-x}T_x$ ($T$ = Ag, Pd). These systems are magnetically similar to the unconventional QCP system $CeCu_{6-x}Au_x$. Consistent with the previous thermodynamic measurements[10, 13], neutron diffraction measurements demonstrate that $CeCu_{6-x}Ag_x$ and $CeCu_{6-x}Pd_x$ host a magnetic QCP at $x \sim 0.2$ and $x \sim 0.05$, respectively. However, the doping dependence of the structural properties is notably different between $CeCu_{6-x}Ag_x$, and $CeCu_{6-x}Pd_x$. In $CeCu_{6-x}Ag_x$, the structural phase transition decreases with Ag-composition until the monoclinic phase is completely suppressed at $x = 0.1$. In contrast, the structural phase transition is almost unperturbed by Pd-substitution in $CeCu_{6-x}Pd_x$. Inelastic neutron scattering measurements of the magnetic QCP composition $CeCu_{5.8}Ag_{0.2}$ show a strange pattern of dynamic magnetic correlations in the (H 0 L) scattering plane. The dynamic susceptibility at the different temperature, wave-vector, and energy fits well with a single phenomenological equation that yields $E/T$ scaling with an almost identical exponent $\alpha = 0.72(1)$. This phenomenology provides a superior fit to the measurements as compared to available theoretical models. A further analysis of the inelastic neutron scattering (INS) measurements provides insight into the origin of the peculiar structure observed in $CeCu_{5.8}Ag_{0.2}$. The diffuse pattern of magnetic scattering comprises of at least two different antiferromagnetic correlations at two wave-vectors $\mathbf{Q}_1$ = (0.65 0 0.3) and $\mathbf{Q}_2$ = (1 0 0). Only the fluctuations at $\mathbf{Q}_1$ appear to be critical at the QCP. The critical part of the dynamic susceptibility shows an agreement with the conventional HMM

model. This observation suggests that the unconventional behavior observed in the $CeCu_{6-x}Ag_x$ can be due to the additional noncritical term in the spectrum. From the study of the non-magnetic series $LaCu_{6-x}Au_x$, the possibility of a new type of quantum critical phenomenon – an elastic QCP – has been experimentally identified. Notably, the elastic QCP in $LaCu_{6-x}Au_x$ can be decoupled from electronic properties and, therefore, is an ideal system to further study the general behavior of a QCP without the additional complication.

The organization of this dissertation is as follows: Chapter 2 gives an overview of QCPs in the heavy fermion system. The unconventional quantum criticality of the heavy fermion series $CeCu_{6-x}Au_x$ is described in detail. A summary of potential theoretical models is presented. Chapter 3 deals with the methods of sample preparation and neutron scattering techniques. Chapter 4 describes a comprehensive study of the structural and magnetic phase transitions in $CeCu_{6-x}T_x$ ($T$ = Ag, Pd). Chapter 5 describes the discovery of an elastic QCP in $LaCu_{6-x}Au_x$. Chapter 6 presents an investigation of the critical spin dynamics of the critical composition $CeCu_{5.8}Ag_{0.2}$ in addition to comparisons to theoretical models.

# Chapter 2

# Introduction

## 2.1 Quantum Critical Point

A phase transition that occurs at zero temperature is called a *quantum phase transition*, which requires a non-thermal control parameter such as pressure, magnetic field, and chemical doping. A point in the phase diagram where a continuous quantum phase transition occurs is known as a QCP. Although the QCP is at zero temperature, the influence of quantum fluctuations remains up to the finite temperature within the limit where the characteristic quantum energy scale $\hbar\omega_Q$ dominates the thermal energy scale $k_BT$. The region near the QCP where the influence of quantum fluctuations is dominant is called the *quantum critical region* (Fig. 2.1). In this region, the inherent quantum nature of the fluctuations engenders fundamentally different critical behavior than that of a classical critical point. Therefore, many interesting properties not arising in the classical systems emerge in the proximity of a QCP.

Several aspects of QCPs are intimately related to other interesting physics problems. Particularly interesting examples belong to the materials in which the correlation between electrons is important. The following are a few examples: many exotic properties of matter emerge in the vicinity of a QCP[26, 27, 28];

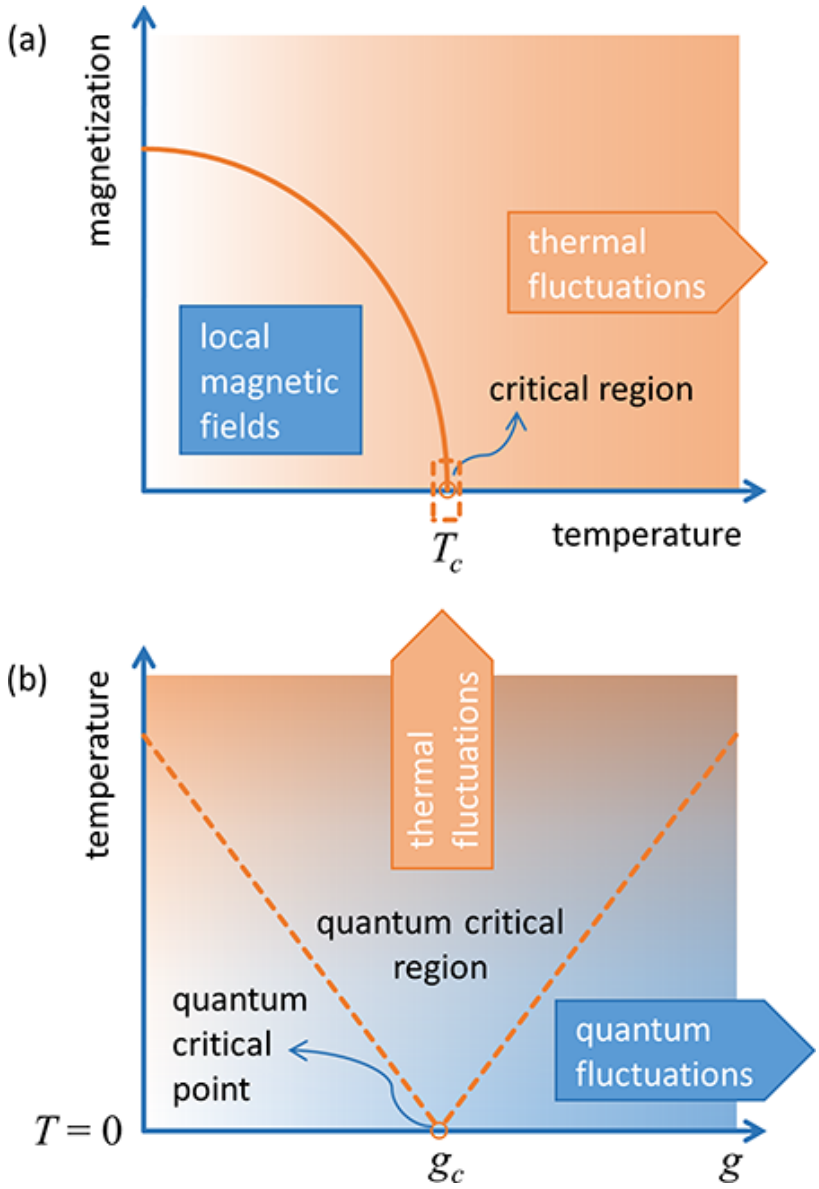



Figure 2.1: Examples of phase diagrams showing (a) a classical phase transition and (b) a QCP. The classical phase transition occurs as the thermal fluctuations lead to a random orientation of the spins. A QCP occurs as a non-thermal parameter $g$ tunes the phase transition to occur at zero temperature. Dashed lines indicate the boundary of the quantum critical region. The quantum critical region near the QCP is dominated by fluctuations that are quantum mechanical in nature. This figure is taken from ref. [2].

the unconventional superconducting state in many heavy fermion systems occurs in the proximity of a magnetic QCP[29, 30]; and, some authors have proposed that high-$T_c$ superconductivity in pnictides and cuprates are associated with a QCP hidden beneath their superconducting dome[31, 32, 33], *etc*. In all these systems, the underlying physics is dominated by a QCP and understanding quantum critical phenomena is crucial to explicating the mechanism behind these complicated problems.

A QCP is fundamentally different from a classical critical point. For the latter, the static and dynamic properties are independent, and the static properties determine the universality class of the phase transition. However, for a QCP, the dynamic critical behavior is inseparable from the static critical behavior.

At a QCP, both the correlation time $\xi_\tau$ and correlation length $\xi_L$ diverge as follows,

$$\xi_L \sim |r|^{-\nu}, \quad \xi_\tau \sim \xi^z \tag{2.1}$$

where $r$ is the distance from QCP and represents the temperature or a non-thermal control parameter. The critical exponents $\nu$ and $z$ characterize the quantum critical behavior of the system. These critical exponents also appear in other thermodynamic ratios. For example, in a pressure tuned QCP, the ratio of thermal expansion to molar specific heat capacity can be defined as Grüneisen ratio ($\Gamma$) at constant pressure [34].

$$\Gamma = \frac{\alpha}{C_p} \tag{2.2}$$

Here, $V_m$ is the molar volume. For T $\rightarrow$ 0, the divergence relation can be expressed as,

$$\Gamma_{cr}(T = 0, r) = G_r |r|^{-1} \tag{2.3}$$

$$\Gamma_{cr}(T, r = 0) = G_T |T|^{-1/\nu z} \tag{2.4}$$

The temperature exponent of a Grüneisen ratio gives the value of the product $\nu z$, providing an alternate route to characterize the QCP.

## 2.2 Quantum criticality in Heavy fermion systems

The phrase *Heavy fermion* is related to the huge effective mass of electronic quasiparticles. The quasiparticles are the pseudoparticles that represent electronic excitations near the Fermi surface. Due to the interaction among electrons, quasiparticles acquire a large effective mass in a heavy fermion material. The large effective mass of the quasiparticles is manifested in thermodynamic properties, in which a large value of the Sommerfeld coefficient is observed in electronic heat capacity. For metals, the electronic heat capacity is expected to be linear with temperature. i.e.,

$$C_{el}/T \approx \gamma \tag{2.5}$$

where the measurement of the Sommerfeld coefficient ($\gamma$)

$$\gamma = \frac{\pi^2 k_B^2 g(E_F)}{3} = \frac{k_B^2 k_F m^*}{3} \propto m^* \tag{2.6}$$

is the most straightforward way to measure the effective mass $m^*$. The Sommerfeld coefficient in a common metal such as copper or aluminum is in the order of 1-10 mJ mol$^{-1}$ K$^{-2}$. For a heavy fermion material, the Sommerfeld coefficient is much larger. For example, in $CeCu_6$, $\gamma$ = 1500 mJ mol$^{-1}$ K$^{-2}$. This value is three orders of magnitude larger than that of common metals.

### Local moments and Kondo Effect

A simple model for heavy fermion behavior considers the dual nature of the electrons. In some instances, the electrons exhibit localized behavior in which case the electrons are restricted to a region around the ion cores and are not allowed to wander. The

spins of the localized electrons appear as tiny magnets called *local moments*. The second aspect is the itinerant character of electrons in which electrons are free to wander and propagate through a material. Such itinerant electrons are also called *conduction electrons*. The interaction between local moments and conduction electrons at a high temperature is generally negligible; therefore, the spins are randomly oriented to form a paramagnetic state. At a low temperature, the strength of interaction dramatically increases, and the strong hybridization of the local moments and conduction electrons leads to heavy fermion behavior.

This hybridization, however, does not typically drive a magnetic order, but rather the conduction electrons form a cloud of opposite spin via a mechanism known as *Kondo effect*, which occurs due to an exchange interaction between an isolated local moment $\mathbf{S}$ and conduction electron spin $\mathbf{s}$[35]. The interaction Hamiltonian can be written in the following form,

$$H = J\mathbf{S}.\mathbf{s} \tag{2.7}$$

where $J$ is the exchange coupling between local moments and conduction electrons. This interaction often causes the spins of conduction electrons to align antiparallel to a local moment. Therefore, the local moments are screened by an antiferromagnetically aligned cloud of conduction electron spins. This screening results in a *Kondo singlet*.

J. Kondo showed that the strength of the Kondo interaction grows logarithmically with decreasing temperature[35].

$$J(T) = J + 2J^2\rho ln\left(\frac{D}{T}\right) \tag{2.8}$$

where $\rho$ is the density of state (DOS) for conduction electron and $D$ is the band width. Equation 2.8 provides an explanation of why some metals with dilute magnetic impurities show an upturn in resistivity with decreasing temperature[35].

### Doniach Phase Diagram

A heavy fermion material consists of a periodic arrangement of local moments interacting with the conduction electrons. This interaction forms a dense array of Kondo singlets, which is called *Kondo lattice*. The conceptual framework of a Kondo lattice was created by Doniach, who explained the Kondo lattice problem using an example of a one dimensional system[36, 37]. Doniach argued that the interplay of the local moments and conduction electrons can be categorized into two distinct interactions. First is the Kondo effect, which favors a nonmagnetic ground state. The second is an indirect exchange interaction between local moments through conduction electrons known as the Ruderman-Kittel-Kasuya-Yosida (RKKY) interaction, which favors a magnetically ordered ground state. Within the Doniach framework, the two scales representing the Kondo and the RKKY interactions are expressed as the following[36].

$$T_K = De^{-1/(|2J_\rho|)} \tag{2.9}$$

$$T_{RKKY} = J^2\rho \tag{2.10}$$

When $J\rho$ is small, $T_{RKKY}$ becomes larger than $T_K$, and the system favors an antiferromagnetically ordered ground state. For a large value of $J\rho$, the Kondo temperature ($T_K$) is larger than $T_{RKKY}$, and the system favors a non-magnetic ground state. When the exchange coupling $J$ is varied, there should be a continuous transition at zero temperature that separates an antiferromagnetic ground state with a Kondo dominated state. The competition between Kondo and RKKY interaction is portrayed in the *Doniach diagram* as shown in Fig. 2.2. The competition between these two interactions provides a natural way to tune a particular system to a magnetic QCP. Experimentally, various techniques including pressure, field, and chemical substitution can be employed to tune heavy fermion materials to a magnetic QCP.

Many heavy fermion materials are found close to a magnetic QCP. As the energy scales are low and crystal quality is often high, several heavy fermion materials have become prototype examples of quantum criticality. For example, $CeCu_6$, $CeCu_2Si_2$, $CeNi_2Ge_2$, $YbRh_2Si_2$ can be tuned to a QCP[1].

## 2.3 Spin Density Wave Quantum Critical Point

Hertz proposed a theoretical explanation of a ferromagnetic QCP in metallic systems using the classical Landau-Ginzburg theory and the Wilson renormalization group methods. This approach is based on the concept that the statics and dynamics are intricately mixed at the QCP and can not be solved separately[17]. The generalized free energy functional is a function of both space and imaginary time; the later being in the interval [0 -i/$T$][17]. This additional dimension enters the free energy functional as an extra spatial dimension $z$, where $z$ is a dynamic exponent[17]. Loosely speaking, a QCP in $d$ dimensions is similar to a classical critical point in $d+z$ dimensions. When the effective dimension exceeds the upper critical dimension $d_c = 4$, the spin fluctuations display a mean field behavior at the QCP[17].

Subsequent work by Millis expanded the theoretical framework of the Hertz model to antiferromagnetic QCPs[18, 19]. Further, Moriya developed a SCR formalism that can be implemented to solve QCP problems[21, 22]. The approach suggested by Millis and Moriya provides a way to determine the dependence of bulk thermodynamic observables on external parameters. The temperature dependence of some thermodynamic properties is given in Table 2.1.

For an antiferromagnetic QCP, the dynamic exponent $z$ = 2, and the magnetic susceptibility can be written as[19, 22],

$$\chi(T) \propto \begin{cases} T, & \text{For 2D} \\ T^{3/2}, & \text{For 3D} \end{cases} \tag{2.11}$$

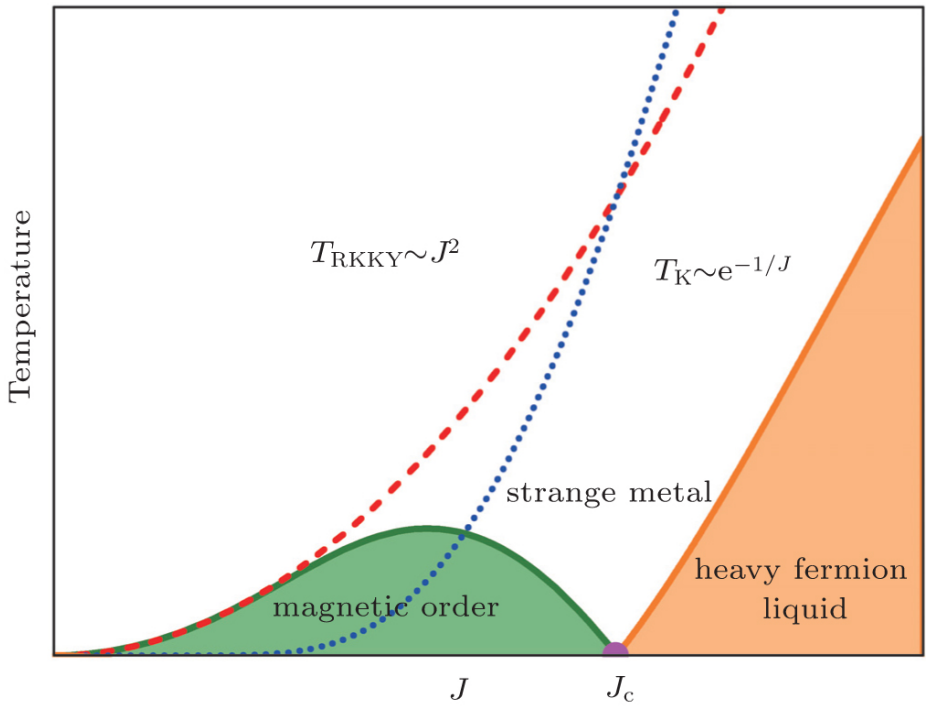



Figure 2.2: Doniach phase diagram. When the Kondo energy scale is smaller than the RKKY energy scale ($T_K < T_{RKKY}$), the ground state is antiferromagnetically ordered. When the Kondo energy scale overcomes the RKKY energy scale($T_K > T_{RKKY}$), a non-magnetic heavy fermion state is formed. A QCP occurs between these two regimes. Figure taken from Ref. [3].

Table 2.1: Temperature dependence of the thermodynamic observables near an HMM QCP. Symbols $\alpha_{cr}$, $C_{cr}$, $\rho_{cr}$ and $\Gamma_{cr}$ represent the critical part of thermal expansion, heat capacity, resistivity and Grüneisen ratio, respectively. Table is taken from Ref. [1].

| | $d$=2<br>$z$=2 | $d$=3<br>$z$=2 | $d$=2<br>$z$ =3 | $d$ = 3<br>$z$=3 |
|---|---|---|---|---|
| $\alpha_{cr} \sim$ | $\ln\ln\frac{1}{T}$ | $T^{1/2}$ | $\ln\frac{1}{T}$ | $T^{1/3}$ |
| $C_{cr} \sim$ | $T\ln\frac{1}{T}$ | $-T^{3/2}$ | $T^{2/3}$ | $T\ln\frac{1}{T}$ |
| $\rho_{cr} \sim$ | $T$ | $T^{3/2}$ | | $T^{5/3}$ |
| $\Gamma_{r,cr} \sim$ | $\frac{\ln\ln\frac{1}{T}}{T\ln\frac{1}{T}}$ | $-T^{-1}$ | $T^{-2/3}\ln\frac{1}{T}$ | $\left(T^{2/3}\ln\frac{1}{T}\right)^{-1}$ |

When the dynamics of the system are considered, the dynamic susceptibility takes the form

$$\chi(E,T) = \frac{1}{\Gamma(T) - iE} \tag{2.12}$$

where $\Gamma(T)$ is the spin relaxation rate. In antiferromagnetic systems, $\Gamma(T)$ varies as

$$\Gamma(T) \propto \begin{cases} T, & \text{For 2D} \\ T^{3/2}, & \text{For 3D} \end{cases} \tag{2.13}$$

Using equations 2.12 and 2.13, the dynamic susceptibility takes the following form,

$$\chi(E,T) \propto \begin{cases} \frac{T^{-1}}{1-iE/T} = T^{-1}\, g(E/T), & \text{For 2D} \\ \frac{T^{-3/2}}{1-iE/T^{3/2}} = T^{-3/2} f(E/T^{3/2}), & \text{For 3D} \end{cases} \tag{2.14}$$

The functions $g(x)$ and $f(x)$ in the equation 2.14 are the scaling functions that characterize two-dimensional and three-dimensional SDW QCPs, respectively.

The approach proposed by HMM is considered the conventional approach to a metallic QCP. In this case, only the fluctuations of the order parameter are involved in the critical phenomena. This approach considers scattering of quasiparticles by spin fluctuations and does not incorporate the role of electronic degrees of freedom in the quantum critical phenomena. Therefore, the evolution of Fermi surface is continuous and the Kondo temperature remains finite at the QCP[38]. The QCP is formed as a spin density wave (SDW) type of instability is developed at the QCP*. Therefore, a HMM QCP is also called a *spin density wave QCP*.

Many aspects of heavy fermion QCPs are consistent with the 3D SDW QCP. The experimental realization of this theory is observed in several thermodynamic quantities. Some heavy fermion systems exhibiting a QPT completely satisfy the predictions of the HMM model. For example, an antiferromagnetic QCP showing

*Here, the phrase *spin density wave* should not be confused with an antiferromagnetic order associated with the nesting of the Fermi surface. Instead, it refers to the strong scattering of quasiparticles at the hot-spots of the Fermi surface

a divergence of Grüneisen ratio with an exponent $x$ = 1[39]; a ferromagnetic QCP $Ni_xPd_{1-x}$ showing a power law dependence of resistivity $\rho \propto T^n$ with exponent $n$ = 5/3[40]; a field induced antiferromagnetic QCP in $CeCu_2Ge_2$ showing $E/T^{3/2}$ scaling of dynamic susceptibility[41]; are all consistent with the HMM model. However, under certain circumstances, the model proposed by Hertz does not completely describe the characteristics of a system[23, 24, 25]. One of the best examples that flouts the predictions of the HMM model is the $CeCu_{6-x}Au_x$, in which a different type of critical behavior is observed at the quantum phase transition. The details of this system are explained in the following section.

## 2.4 Properties of $CeCu_{6-x}Au_x$

At room temperature, the end member $CeCu_6$ crystallizes in an orthorhombic structure as shown in the Fig. 2.3[4]. The orthorhombic unit cell contains four formula units of $CeCu_6$ in which Ce and Cu atoms occupy one general and five special sites. Ce atoms sit in one of the special 4$c$ sites. Cu atoms occupy the 8$d$ site (Cu1) and four 4$c$ sites (Cu2, Cu3, Cu4 and Cu5)[4]. This orthorhombic structure undergoes a monoclinic distortion (space group: $P2_1/c$) near 220 K. The distortion results in a loss of mirror symmetry for the Cu1 site, while the point symmetry of the remaining sites is preserved in the monoclinic structure. Resonant ultrasound spectroscopy (RUS) measurements indicate that the structural phase transition takes place with a gradual softening of transverse elastic constant $C_{66}$ [42] and that the corresponding transverse acoustic phonon mode becomes soft at the phase transition[43]. These observations suggest the structural phase transition is continuous $CeCu_6$.

The ground state of $CeCu_6$ is a non-magnetically ordered state[44, 45]. The absence of magnetic ordering is due to the strong hybridization between localized 4$f$ and itinerant 3$d$-electrons, which is intimately related to the heavy fermion behavior. Heavy fermion behavior in $CeCu_6$ is apparent in thermodynamics and transport measurements, which show a high value ($\gamma$ = 1.45 J/K mol) of electronic

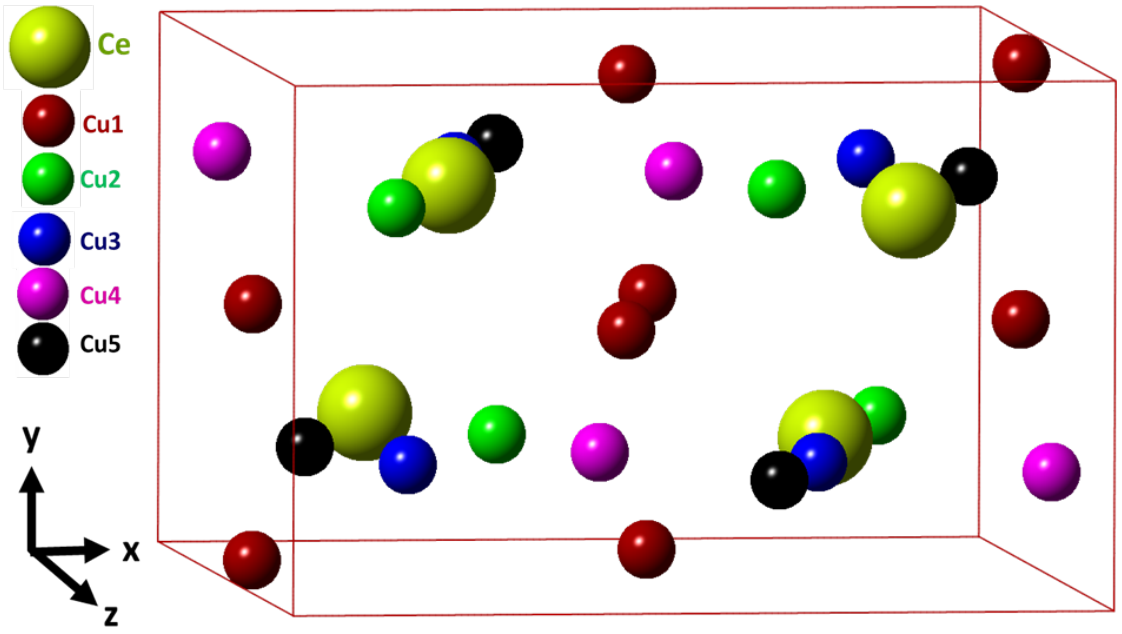



Figure 2.3: Room temperature crystal structure of $CeCu_6$ reproduced using the parameters from Ref. [4].

heat capacity, $T^2$ dependence in resistivity ($\rho$), and the occurrence of residual positive mangetoresistivity[46]. All these properties of $CeCu_6$ are the characteristics of a non-magnetically ordered heavy fermion compound.

INS measurements of $CeCu_6$ show the presence of strong dynamic magnetic correlations at low temperature[47, 48, 49]. The correlations appear as a diffuse pattern in the (H 0 L) scattering plane[9]. The magnetic scattering is almost everywhere in reciprocal space and can be categorized as an overlap of two independent terms: The first term is due to the single site spin fluctuations that arise from excitation of $Ce^{3+}$ local moments. This term constitutes almost 90% of the spectral weight[47, 48, 49]. The localized component of the excitation spectrum appears as a $\mathbf{Q}$−independent term in the reciprocal space and is quasielastic. The Lorentzian width of the quasielastic scattering is 0.42 meV at 25 mK, which corresponds to a Kondo temperature of ~5 K. This estimation is fairly close to the values obtained from other techniques[50]. The second term is due to the correlated fluctuations that represent the intersite correlation of $Ce^{3+}$ moments. This term is peaked at two wave-vectors: $\mathbf{Q}$ = (0.85 0 0) and $\mathbf{Q}$ = (0 1 0)[†]. At both wave-vectors, the fluctuations are peaked at an energy transfer of 0.25 meV at low temperatures[47, 48]. The correlation lengths and time saturate below 1 K[47, 48, 49]. This lack of divergence is consistent with the non-magnetic ground state[44, 45].

The correlated fluctuations are predominately longitudinal, and no transverse fluctuations are reported in the literature[47, 48, 49]. The absence of transverse fluctuations suggests that the ground state of $CeCu_6$ has a local Ising anisotropy along $c$-axis. This anisotropy is consistent with the field dependence of magnetic fluctuations, which shows that a small magnetic field of 2.5 T applied along $c$-axis dramatically suppresses the correlations. Furthermore, thermodynamic and

[†]Note that the wave-vectors have been translated to orthorhombic notation for easy comparison with other compositions.

transport measurements of $CeCu_6$ indicate a strong anisotropy with the magnetization being in the ratio of 1:2:10 along with $b : a : c$-axis of orthorhombic structure[46, 50, 51].

Although the end member $CeCu_6$ does not magnetically order, magnetic order can be induced by partially substituting Cu with a larger element such as Au. Long range incommensurate magnetic order develops near $x_c \approx 0.1$ in $CeCu_{6-x}Au_x$. The magnetic structure consists of $Ce^{3+}$ moments along the $c$-axis. The amplitude of the spins is modulated with an incommensurate propagation vector. The size of the ordered moment near the QCP is roughly 0.1 $\mu_B$/Ce, but increases up to 1 $\mu_B$/Ce at higher Au-compositions[52]. While this magnetic structure is considered to be valid throughout the series, the propagation vector of magnetic structure changes dramatically with Au doping[52, 53, 54, 55, 56]. For $x = 0.2$ (i.e, the composition nearest to the QCP studied by neutron diffraction), short range order at the wave-vector $\mathbf{Q}$ = (0.8 0 0) with a long range incommensurate order at $\mathbf{Q}$ = (0.625 0 0.275) is reported[‡][6, 8, 52, 57]. For a slightly higher Au-doping, $x = 0.3$, the short range order disappears and only long range incommensurate order at $\mathbf{Q}$ = (0.625 0 0.275) is observed[6, 8, 52]. For higher doping ($x$ >0.5), long range order continues to exist, although the wave-vector crosses over to $\mathbf{Q}$ = (0.59 0 0) [6, 8, 52, 58]. A similar evolution of the propagation vectors is observed in the pressure dependence of magnetic structure in $CeCu_{6-x}Au_x$[59].

From the perspective of the crystal structure, the evolution of long range order appears to be due to the expansion of unit cell volume. When Cu is partially substituted by Au, the expansion along the $a$ and $c$ axis results in an overall increase in the unit cell volume proportional to Au composition. Interestingly, an Au atom in $CeCu_{6-x}Au_x$ sits in only one of the special sites Cu2 until this particular site is fully occupied[60]. The reason behind this exclusive site preference is not fully understood

[‡]Note that the short range order in $CeCu_{5.8}Au_{0.2}$ can also be due to the inelastic contribution to the diffraction.

although it appears to be due to the larger volume around Cu2 site as compared to other Cu sites[7].

The orthorhombic-monoclinic transition observed in $CeCu_6$ is a common feature of the $RCu_6$ (R = Rare earth) series. Studies in various members of $RCu_6$ have demonstrated that this type of transition is continuous[7, 42, 43, 61, 62]. In the phase diagram of $CeCu_{6-x}Au_x$, the continuous orthorhombic-monoclinic phase transition can be tuned to occur at zero temperature (Fig. 2.4), raising the intriguing possibility that zero temperature structural transition gives rise to a new type of quantum phase transition: the structural quantum critical point (SQCP).

A prominent aspect of the $CeCu_{6-x}Au_x$ phase diagram that has not received enough attention is the doping dependence of the structural phase transition. The structural transition temperature in $CeCu_{6-x}Au_x$ falls linearly with Au concentration and disappears at x $\sim$ 0.13[5]. This composition is very close to the magnetic QCP described earlier. Thus, structural degrees of freedom may play an important role in the anomalous quantum critical behavior of the $CeCu_{6-x}Au_x$ system. Because of this, Robinson *et al* suggested that the structural critical point and magnetic QCP coexist at $x$ = 0.1, which suggests the possibility that $CeCu_{6-x}Au_x$ hosts a quantum multicritical point and that both the structural and magnetic degrees of freedom are coupled[5]. The role of structural degrees of freedom is one of the key questions this dissertation addresses.

## 2.5 Quantum Criticality in $CeCu_{6-x}Au_x$

As shown in the Figs. 2.5 and 2.6, the diffuse patterns of dynamic magnetic correlations do not significantly change with Au-substitution[9]. For both compositions — at the QCP and at the magnetically ordered region of the phase diagram — the pattern of dynamic scattering is very similar to the parent compound[9], which rules out the possibility that a doping induced disorder is the origin of the peculiar structure[9]. This diffuse pattern is widely interpreted as evidence of the

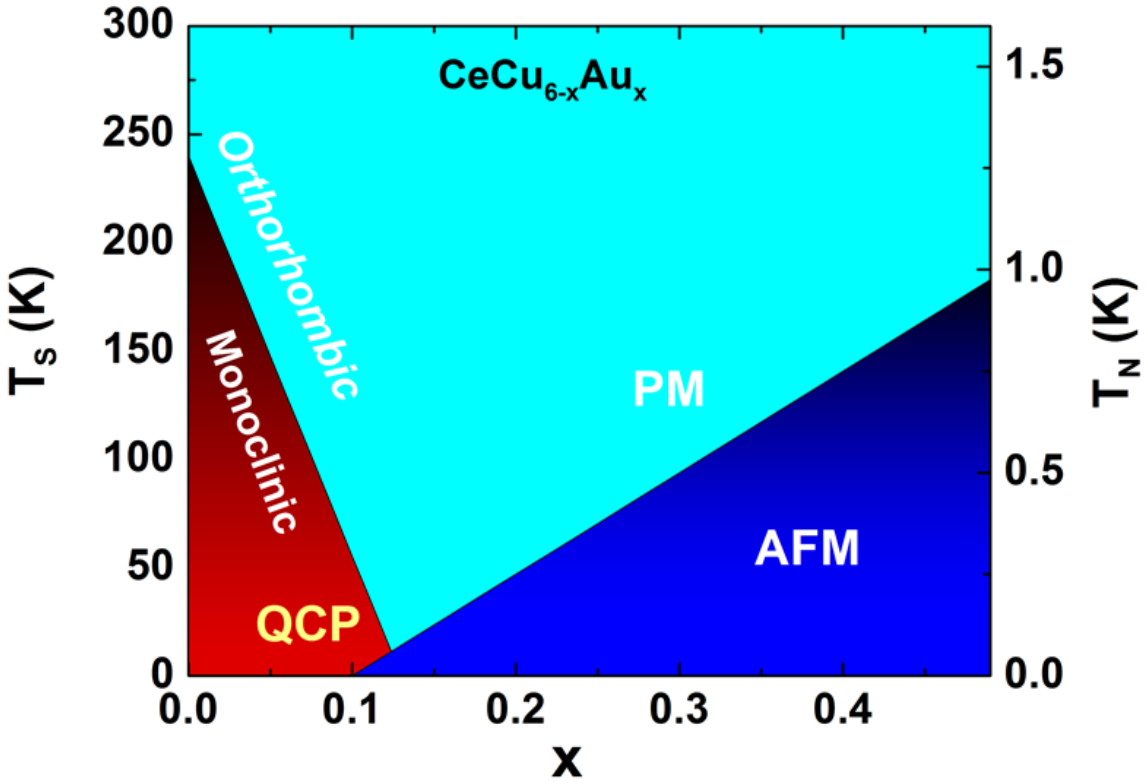



Figure 2.4: Phase diagram of $CeCu_{6-x}Au_x$ showing structural and magnetic phase transitions. The structural transition temperatures ($T_S$) decrease upon alloying with Au. The extrapolation of $T_S$ with $x$ suggests that the monoclinic structure is completely suppressed near $x \approx 0.13$. Antiferromagnetic order emerges with Au-substitution with a magnetic QCP occurring at $x \approx 0.1$. $T_S$ and $T_N$ are taken from several sources[5, 6, 7, 8].

two-dimensional character of the magnetic fluctuations[54, 63]. Interestingly, the intensity of the dynamic scattering is peaked at the wave-vectors that correspond to the propagation of the long range magnetic order for different compositions of $CeCu_{6-x}Au_x$. However, it is not clear whether the peculiar structure originates from the multiple critical wave-vectors[54, 63].

Many aspects of the QCP in $CeCu_{6-x}Au_x$ are unique among heavy fermion systems[24, 25]. The defining signature of the unique behavior is the fractional exponent in $E/T$ scaling of dynamic susceptibility. The QCP composition $x$ = 0.1 fits well with a phenomenological scaling relation in the form $\chi''(E,T) = T^{-\alpha} g\left(\frac{E}{k_B T}\right)$ giving an anomalous fractional exponent $\alpha$ = 0.75[24, 25]. Thermodynamic and transport measurements consistently attest the unconventional nature of the QCP: the heat capacity over temperature diverges logarithmically; and the resistivity varies linearly with temperature, contrary to the expectations for a 3D HMM QCP. Although the $E/T$ scaling can be understood within a 2D SDW picture, the fractional value of a scaling exponent is not expected for both 2D and 3D HMM QCP[24, 25].

While the quantum critical phenomenon of $CeCu_{6-x}Au_x$ is unconventional, the magnetic field tuned QCP in the same series appears to be more consistent with a three dimensional SDW QCP[64, 65, 66]. In $CeCu_{6-x}Au_x$, a field tuned QCP can be achieved by suppressing the magnetic order with the field. Thermodynamic and transport measurements show that the nature of the field driven QCP in $CeCu_{6-x}Au_x$ is characteristically different from the composition tuned QCP. In the field tuned QCP, resistivity scales as $\rho \propto T^{3/2}$ at low temperatures, and the heat capacity over temperature shows a power law behavior with equation $C/T \propto \sqrt{T}$[66] results which are significantly different from the composition tuned QCP described earlier. Furthermore, the dynamic susceptibility scales with the relation $\chi''(E,T) = T^{-\alpha} f\left(\frac{\omega}{k_b T^{\beta}}\right)$ with (a = 1.5, $\beta$ = 1.5) is consistent with the three dimensional SDW QCP in $CeCu_{6-x}Au_x$[64, 65].

The above discussion of dynamics of spin fluctuations in $CeCu_{6-x}Au_x$ points to several unresolved questions that if answered will lead to new understanding.

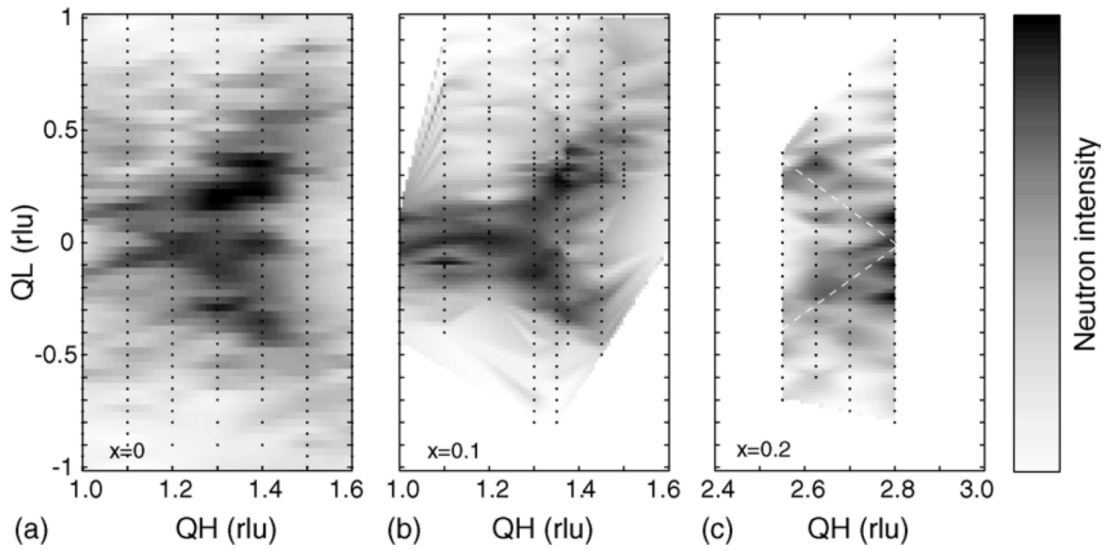



Figure 2.5: Two dimensional contour plots showing the dynamic magnetic correlations in (a) the parent compound $CeCu_6$, (b) QCP composition $CeCu_{5.9}Au_{0.1}$, and (c) the magnetically ordered composition ($T_N \approx 0.2$ K) $CeCu_{5.8}Au_{0.2}$. $CeCu_6$ and $CeCu_{5.8}Au_{0.2}$ were measured with an energy transfer of $E = 0.15$ meV. $CeCu_{5.9}Au_{0.1}$ was measured with $E = 0.1$ meV. For all compositions, a similar diffuse pattern of magnetic correlations is observed with the rod shaped structure. This plot is taken from Ref. [9].

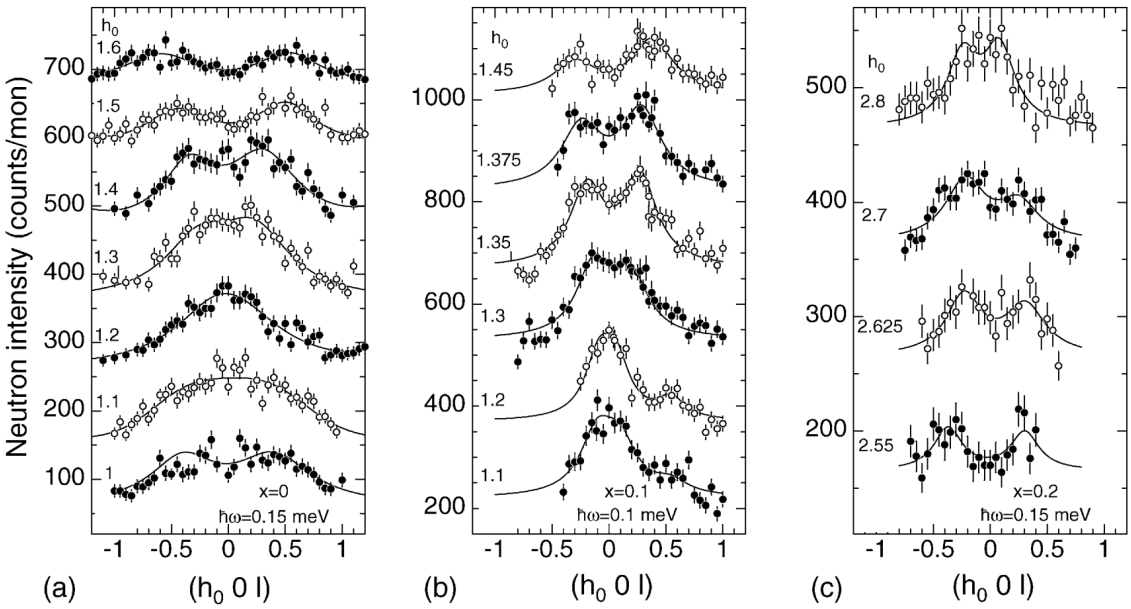



Figure 2.6: Constant energy scans along [0 0 1] for (a) the parent compound $CeCu_6$ scanned at $E$ = 0.15 meV (b) QCP composition $CeCu_{5.9}Au_{0.1}$ scanned at $E$ = 0.1 meV. (c) A magnetically ordered composition ($T_N \approx 0.2$ K) $CeCu_{5.8}Au_{0.2}$ scanned at $E$ = 0.15 meV. This plot is taken from Ref. [9].

Previous studies suggest that while the critical fluctuations associated with the field tuned QCP in $CeCu_{6-x}Au_x$ are three dimensional, the fluctuations in composition tuned QCP are considered two dimensional. Furthermore, in the composition tuned QCP, some aspects attributed to unconventional character are based on the assumption that the fluctuations are two-dimensional. This assumption, however, heavily relies on the rod shaped structure of diffuse magnetic correlations observed during INS measurements; but no compelling experimental evidence exists to support this assumption. This lack of evidence raises an important question regarding whether the correlations are truly two dimensional, or if the diffuse pattern has a different origin.

## 2.6 Quantum Critical Point in $CeCu_{6-x}T_x$ ($T$ = Ag, Pd, Pt, Sn)

Similar to Au doping, magnetic order in $CeCu_6$ evolves with partial substitution of Cu by other transition metal elements. Previous work suggests that magnetic order can be induced by partially substituting Cu with heavier transition elements such as in $CeCu_{6-x}Ag_x$, $CeCu_{6-x}Pd_x$, $CeCu_{6-x}Sn_x$, $CeCu_{6-x}Pt_x$ [10, 13, 67]. In all these systems, the crossover from a non-magnetic heavy fermion state to an antiferromagnetic ground state takes place with the appearance of non-Fermi liquid behavior, which is a common hallmark of heavy fermion systems at a QCP[10, 13, 67]. The evolution of magnetic order in these series is attributed to the expansion of unit cell volume, which stabilizes the $Ce^{3+}$moment. For the same reason, Ni substitution in $CeCu_{6-x}Ni_x$ decreases the crystallographic unit cell volume and does not lead to magnetic order[13].

Being isoelectronic to the well-known QCP system $CeCu_{6-x}Au_x$, the doping series $CeCu_{6-x}Ag_x$ has earned more attention than the remaining $CeCu_6$-derived QCPs. $CeCu_{6-x}Ag_x$ hosts a composition tuned QCP and the field tuned QCPs, which are

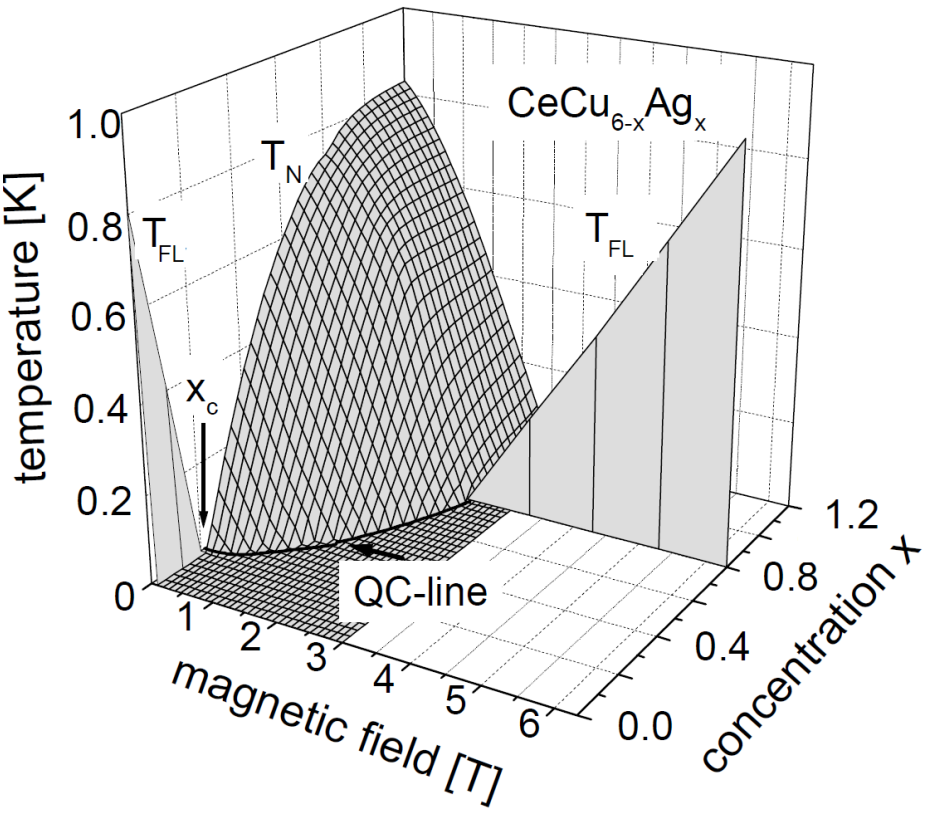



Figure 2.7: Phase diagram of $CeCu_{6-x}Ag_x$ showing the dependence of magnetic order with field and Ag composition. At zero filed, a magnetic QCP in $CeCu_{6-x}Ag_x$ occurs at $x = 0.2$. Taken from Ref. [10].

shown in the three dimensional phase diagram (Fig. 2.7). Similar to $CeCu_{6-x}Au_x$, the field tuned QCP $CeCu_{6-x}Ag_x$ is characteristically different from the composition tuned QCP. In the field tuned QCP of $CeCu_{6-x}Ag_x$, the $C/T$ varies as a square root of temperature and resistivity is proportional to $T^{1.5}$, which is very similar to the field tuned QCP in $CeCu_{6-x}Au_x$ and is generally understood as a 3D SDW QCP[12]. At the composition tuned QCP $CeCu_{5.8}Ag_{0.2}$, the heat capacity displays a logarithmic divergence of $C/T$ with decreasing temperature; and resistivity is proportional to $T^2$ at low temperatures, similar to the composition tuned QCP in $CeCu_{6-x}Au_x$[10]. Furthermore, the ratio of heat capacity to thermal expansion, the *Grüneisen ratio*, diverges more weakly than expected for a 3D SDW QCP, suggesting that the critical behavior of the composition tuned QCP in $CeCu_{6-x}Ag_x$ is inconsistent with the conventional 3D SDW QCP[§][14]. In summary, the physical behavior of the $CeCu_{6-x}Ag_x$ and the $CeCu_{6-x}Au_x$ series is broadly consistent.

## 2.7 Understanding $E/T$-scaling

The observation of $E/T$ scaling with an anomalous fractional exponent at the composition tuned QCP in $CeCu_{6-x}Au_x$ has prompted a debate as to correcting the understanding of the quantum critical phenomenon. Recently, several theoretical approaches have been proposed to explain this observation. This section provides a brief introduction to the theoretical models and summarizes the scaling equations derived on the basis of their formalism.

### 2.7.1 Local QCP

This approach considers a continuous disappearance of a *local energy scale* at the QCP[68, 69]. Here, the local energy scale represents the local moments that couple

[§]Note that the Grüneisen ratio measurement was performed on a polycrystalline sample[14] and that the strongly anisotropic character of $CeCu_{6-x}Ag_x$ may be responsible for the deviation from conventional behavior. A similar study on a single crystal would be illuminating.

with electrons to form a Kondo singlet in the paramagnetic side of the phase diagram. Due to the hybridization of local moments and conduction electrons, the paramagnetic side of the phase diagram is characterized by a large Fermi surface, and heavy fermion behavior is apparent in the thermodynamic and transport measurements. Due to the breakdown of the local energy scale at the QCP, there is a substantial change in the degree of hybridization of local moments and conduction electrons. Hence, in the magnetically ordered side of the phase diagram, local moments can interact with each other. The change in the hybridization results in a sudden change in the Fermi surface, and discontinuities in the electronic properties are expected at the QCP. This type of critical behavior is only expected when the fluctuations are 2D[68, 69]. For a system with three dimensional fluctuations, magnetic coupling along a third direction does not allow a complete suppression of local energy scale and leads to a conventional HMM behavior[70].

The locally critical phenomenon is due to the contribution of critical fluctuations that arise from a continuous disappearance of local energy scale in addition to the long wavelength fluctuations of the order parameter[68, 69].

Using an extended dynamical mean field theory (EDMFT) calculation, the magnetic susceptibility is given by[68, 69],

$$\chi(\mathbf{Q},E,T) = \frac{1}{f(\mathbf{Q}-\mathbf{Q}_0) + AT^{\alpha}\mathscr{M}(E/T)} \tag{2.15}$$

where $Q_0$ is an ordering wave-vector. The scaling function $\mathscr{M}$ has a form[68, 69].

$$\mathscr{M}(E/T) = exp[\alpha\psi(1/2 - iE/2\pi T)] \tag{2.16}$$

Here, $\psi$ is the *diagamma function*. The exponent $\alpha$ is expected to be a non-integer. Depending on the details of the approximations used, the exponent $\alpha$ is predicted to be between 0.72 to 0.83[71, 72, 73]. The dynamic susceptibility is expected to be distributed over a large region of the $\mathbf{Q}-$space. The $\mathbf{Q}$ dependent term near the

antiferromagnetic wave-vector is expected to vary as[68, 69],

$$f(\mathbf{Q}-\mathbf{Q}_0) \approx \frac{1}{(\mathbf{Q}-\mathbf{Q}_0)^2} \tag{2.17}$$

Using equation 2.15, the static susceptibility can be written as,

$$\chi(T) = \frac{1}{\Theta + AT^{\alpha}} \tag{2.18}$$

which demonstrates that the same scaling exponent $\alpha$ appears as a power law exponent in the static susceptibility. Here, $\Theta$ is a positive constant that carries a similar meaning as that to the Weiss temperature in Curie-Weiss law.

At an ordering wave-vector, $\mathbf{Q} = \mathbf{Q}_0$, the $\mathbf{Q}-$dependent term $f(\mathbf{Q}-\mathbf{Q}_0)$ in equation 2.15 vanishes. The dynamic susceptibility in this case takes the following form,

$$\chi(\mathbf{Q}_0, E, T) = \frac{1}{AT^{\alpha}\mathscr{M}(E/T)} \tag{2.19}$$

which yields $E/T-$scaling.

### 2.7.2 Strong-coupling QCP

In the conventional approach described by HMM, the role of electronic degrees of freedom is completely ignored. This issue is addressed by the *strong coupling* approach, which assumes strongly interacting quasiparticles with the long wavelength fluctuations of the order parameter. Based on this approach, the Kondo temperature remains finite at the QCP and local moments survive in the magnetically ordered state. Due to strong coupling between quasiparticles and long wavelength fluctuations of the order parameter, the critical behavior is modified from HMM behavior.

The strong-coupling of the magnetic fluctuations and quasiparticles leads to a scaling equation[74, 75],

$$\chi''(\mathbf{q}, E, T) = \xi^2 \phi(x, y) \tag{2.20}$$

where, $\xi \propto T^{-1/z}$, $x = E/T$, $y = q\xi$, and

$$\zeta = (x^2 + a^2)^{\eta/2} \tag{2.21}$$

$$\phi(x, y) = \frac{x/\zeta^2(x)}{(1 + S(\mathbf{Q} - \mathbf{Q}_0)T^{-3/4})^2 + [x/\zeta^2(x)]^2} \tag{2.22}$$

For $d$-dimensional spin fluctuations, the dynamic critical exponent and the exponent $\eta$ is related by,

$$z = \frac{2}{(1 - 2\eta)} = \frac{4d}{3} \tag{2.23}$$

The $\mathbf{Q}$-dependent function $S$ is expected to be a quadratic function of $\mathbf{Q} - \mathbf{Q}_0$, where $\mathbf{Q}_0$ is an antiferromagnetic wave-vector. At $\mathbf{Q} = \mathbf{Q}_0$ the equation 2.20 reduces to an $E/T$ scaling.

$$\chi''(E, T) = T^{-3/4} f(E/T) \tag{2.24}$$

where the scaling function,

$$f(E/T) = \frac{(E/T)/[((E/T)^2 + a^2)]^{1/8}}{1 + (E/T)/[((E/T)^2 + a^2)]^{1/8}} \tag{2.25}$$

reduces to an $(E/T)^{3/4}$ scaling when $E/T >> a$. Here, $a$ is a constant, which is expected to be in the order of unity.

This model predicts the temperature dependence of some thermodynamic quantities. The heat capacity at QCP should follow the power law equation in the following form

$$C/T \propto T^{(2d+1-2z)/z} \tag{2.26}$$

The critical part of susceptibility can be written as

$$\chi - \chi(H_c, 0) \propto -T^{1-1/\nu z} \tag{2.27}$$

The temperature dependence of Grüneisen ratio takes the following form

$$\Gamma_G \propto T^{(z-2d-1)/z} \tag{2.28}$$

### 2.7.3 Dissipative XY QCP

The *dissipative XY* model presents a fundamentally new type of quantum critical behavior[76]. This model evaluates critical behavior in terms of topological excitations, which is a significantly different approach compared to the local QCP and the strong coupling approach that are based on renormalized spin fluctuations. The critical point according to the dissipative XY model is driven by a topological pseudoparticle called *warps*. A warp is a charge neutral entity, which consists of a charge monopole symmetrically surrounded by antimonoples. A QCP occurs with the dissipation of warps[77].

This model predicts that the magnetic fluctuations are separable in space and time[76, 78], i.e. the magnetic fluctuations are separable function of $E, T$ and $\mathbf{Q}$. This prediction implies that the $E/T$ scaling is expected to occur everywhere in the scattering plane[76, 78]. The separability of $\mathbf{Q}$ and $E, T$ also suggest that the correlation lengths remain independent of energy transfer at fixed temperature[76, 78].

The dynamic susceptibility according to XY-dissipation model takes the form[76, 78],

$$\chi''(\mathbf{Q}, E, T) = -\chi_0 \tanh\left(\frac{E}{2T}\right) F(\mathbf{Q} - \mathbf{Q}_0)\, F_u\left(\frac{T}{\kappa_E}\right) F_l\left(\frac{E}{E_c}\right) \tag{2.29}$$

where, the function $F_u\left(\frac{T}{\kappa_E}\right)$ represents a deviation from a QCP. At the QCP, $F_u\left(\frac{T}{\kappa_E}\right) = 1$. The $\mathbf{Q}$ dependent term takes a Lorentzian form expressed as,

$$F(\mathbf{Q}-\mathbf{Q}_0) \propto \frac{1}{\kappa_q^2 + |\mathbf{Q}-\mathbf{Q}_0|^2} \tag{2.30}$$

# Chapter 3

# Research Techniques

This chapter focuses on the fundamentals of material preparation and neutron scattering techniques. The polycrystalline samples for various composition of $CeCu_{6-x}T_x$ (T = Ag, Pd) and $LaCu_{6-x}Au_x$ were prepared using arc melting. Single crystals were synthesized using a Czochralski process in a tri-arc furnace. The details on the synthesis of large single crystals are described. An overview of neutron scattering techniques is presented with a brief introduction of typical instruments used in the dissertation research described in the following chapters.

## 3.1 Material Synthesis

Single crystals and polycrystalline samples of $CeCu_{6-x}T_x$ (T = Ag, Pd) and $LaCu_{6-x}T'_x$ (T′ = Au, Ag) were synthesized for this research using the techniques described below. The polycrystalline samples were measured for structural characterization and thermodynamic measurements. Single crystals were measured using neutron diffraction for a more extensive characterization of crystal structure and for the determination of magnetic structures. Selected single crystals were measured using INS measurements to understand the spin dynamics.

### 3.1.1 Arc-melting

Polycrystalline samples were prepared by arc melting stoichiometric compositions of elements. An electric arc melting furnace* (Fig. 3.1) was used for this purpose. The furnace consists of a melting chamber where an electric spark can be produced in an inert atmosphere. The arc produced in the furnace can easily melt up to 20 g of starting material and reach high temperatures (3500 °C), which is well above the melting point of most elements. To protect from excessive heat and damage, the interior of the hearth and the furnace wall are water cooled. The furnace chamber is connected to a vacuum pump and a source of high purity argon supply.

To prepare a polycrystalline sample, a stoichiometric proportion of the starting elements was placed at the center of the hearth. The cold water supply was turned on to protect the hearth and furnace from excessive heat. The melting chamber was purged several times using ultra high purity argon and vacuum pump. A piece of zirconium metal placed at a corner of the hearth was melted to eliminate the remaining oxygen from the furnace. The starting elements were then melted, flipped and remelted at least three times for homogeneity.

### 3.1.2 Czochralski Process

Named after a Polish scientist, who developed the technique in 1916[79], the Czochralski process is an ideal way of growing a large single crystal of materials, particularly those having a high melting point. This process is extensively used in the large scale manufacturing of single crystal silicon. A Czochralski setup requires a furnace in which a polycrystalline form of the material can be melted in a crucible.

A tri-arc furnace was utilized for the Czochralski process described here. The furnace consists of upper and lower water-cooled sections separated by a quartz window. The upper section contains three drilled holes for holding copper rods. The electrodes that generate the arc are made of thoriated tungsten rods of diameter

*This furnace is commercially available from Edmund Bühler GmbH.



Figure 3.1: A *Compact Arc Melter MAM-1* commercially available from Edmund Bühler GmbH. The picture is taken from the web page of Edmund Bühler GmbH.



Figure 3.2: The tri-arc arrangement in the synthesis laboratory of the Mandrus Research group.

$\frac{3}{32}$". The electrodes are inserted and attached to the end of copper rods. The copper rods are mounted with swivel balls that allow vertical as well as angular movements of the electrodes. Current in the electrodes is controlled by a separate electrical circuit *resistor box*, which maintains uniformity of current among the electrodes. An O-ring fitting system at the center of this section allows a seed rod to slide and rotate without disturbing the inert atmosphere of the chamber. Lower section of the furnace consists of a tapered opening in the center, where a hearth can be inserted and tightly clamped. The hearth consists of a cylindrical graphite platform surrounded by a tapered copper cylinder. The graphite platform can rotate with a motor connected at the bottom of the platform. The rotation of the hearth is externally controlled by a motor controller, which can rotate the hearth at the speed of 1 revs/min to 100 revs/min. The periphery of the hearth and the furnace is connected to a cold-water circuit that protects the hearth from excessive heat. During the growth, the furnace is purged continuously with ultra high purity of argon. A short video clip demonstrating the growth of $CeCu_6$ can be seen at https://www.youtube.com/watch?v=DPdc7A5lTes.

I designed a separate crystal puller assembly that can rotate and pull the seed rod during the growth (Fig. 3.2). The assembly is made of three independent motors. The first motor rotates the seed rod at a fixed speed of ~ 40 rev/min. The second motor is for the vertical motion of the seed rod during the growth. The pulling speed is externally controlled by the circuit, which can precisely control the speed within the range of 0.1 mm/hr to 45 mm/hr. This pulling speed is not always practical, for example, if an initial adjustment of the seed rod is desired at a much faster rate. For these proposes, a third motor, which can move much faster (~1 mm/sec) is used.

Prior to the Czochralski process, a large button (~ 10 g or more) of polycrystalline material is prepared using arc melting as described in the section 3.1.1. The polycrystalline button is placed in the center of the graphite hearth. It is always useful to put the polycrystalline button exactly at the center of the hearth and adjust the stingers equidistant from the center so that the melting is symmetric. The

chamber is then purged for 30 minutes with ultra high purity argon additionally purified by passing through a gas purifier. An electric arc is produced by electric contact of the stinger with the hearth. When the sample is completely melted, the seed rod[†] is lowered down to the melt. The seed rod touches the melt and serves as a nucleation site for crystal growth. The seed rod is then pulled vertically upward at a uniform speed of ~ 20 mm/hr. It is important to note that the tip of the tungsten seed rod may nucleate multiple crystals that are randomly oriented. To maintain single crystallinity within a large sample, the nucleated rod is necked down to a smaller diameter. This necking process eliminates unwanted grains inside a large crystal by allowing only a single grain to nucleate along the neck. Having a long neck with as small cross section as possible is desirable. The neck and the crystal grown using this method are shown in the Fig. 3.3.

Since the starting elements (i.e., Ce, La, and Cu) are extremely sensitive to oxygen, commercial grade ultra-high purity argon, which contains more than a few parts per million of oxygen, results in the formation of oxides of cerium and copper during the growth. These metallic oxides have much higher melting temperatures; and due to their lower density, a layer of oxide forms at the top of the melt during growth. The oxides nucleate crystals in random directions, and many tiny crystals are formed at the end of the growth. For single crystallinity, it is therefore crucial to maintain a high degree of inert atmosphere in the melting chamber. For this purpose, a PPM grade dual column inert gas purifier system is used. This purifier system contains two units. The first unit eliminates oxygen impurities to less than 0.1 parts per million, and the second unit reduces moisture to less than 1 ppm. These units are connected in series between the furnace chamber and the argon cylinder.

[†]I used tungsten rod of $\frac{3}{32}$" diameter as a seed rod.




Figure 3.3: Single crystal of $CeCu_{5.9}Pd_{0.05}$ grown by the Czochralski process. The diameter of top portion of the crystal is intentionally made as small as possible. The crystal below the neck is verified to be a single crystal from neutron diffraction measurements.

## 3.2 Neutron Scattering

Because neutron scattering techniques are particularly important to the investigations described in this dissertation, the following sections provide an overview of some of the most important concepts relevant to the technique. This overview draws extensively from more comprehensive descriptions as can be found in the references [80, 81, 82, 83, 84].

The use of neutron scattering has several advantages in the diverse area of research that involves magnetic materials. Neutrons carry magnetic moment, which interacts with the spins of unpaired electrons in a material. The ability to interact with the spins makes neutron scattering a perfect tool for magnetic measurements. As neutrons do not carry a charge, they can deeply penetrate inside materials. Neutrons are also suited for diffraction as the interatomic spacing of solids is comparable to the De-Broglie wavelength of thermal neutrons. Furthermore, the energy of neutrons is comparable to magnetic and lattice excitations in a solid. All these properties of neutrons are useful for exploring physics in a wide variety of materials.

A neutron scattering experiment requires a beam or pulse of the neutrons incident on a target material. During this process, the neutron exchanges energy and momentum with the target material. The energy and momentum of neutrons are conserved during this process, i.e., the amount of energy and momentum lost or gained by neutrons equals to the energy and momentum of an excitation inside a material. Thus, by measuring the energy and momentum of scattered neutrons, an excitation inside the target material can be examined. Scattering can also occur without an exchange of energy and as such is called *elastic scattering*. The elastic scattering provides information on the static properties of the material such as crystal and magnetic structure.

If $\mathbf{k_i}$ and $\mathbf{k_f}$ are the wave-vector of incident and scattered neutron respectively. The principle of conservation of momentum ensures that the momentum transferred

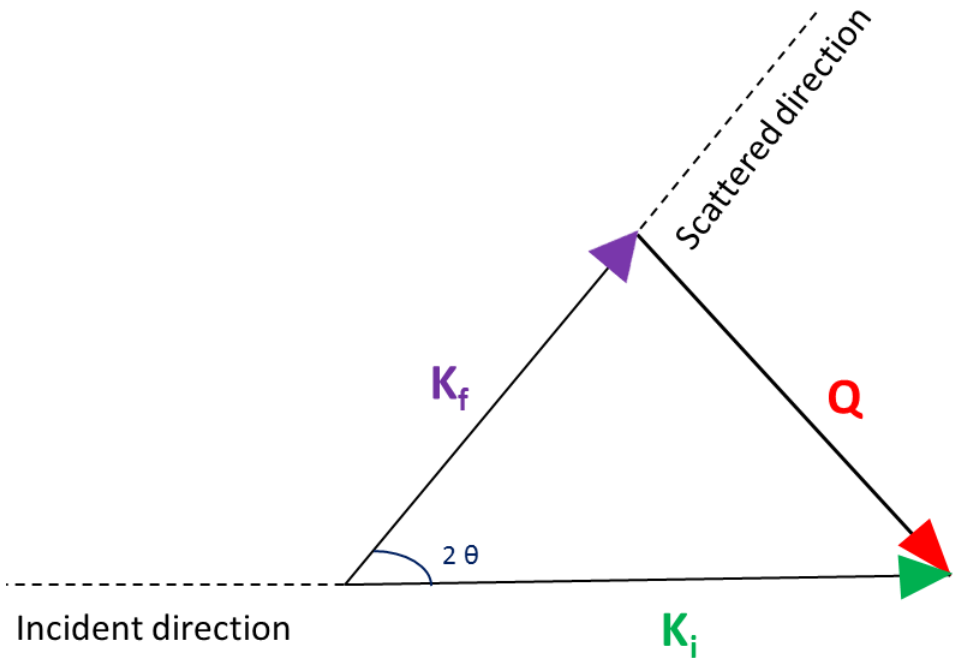



Figure 3.4: Scattering triangle showing geometry of neutron scattering. The neutron is deflected at an angle of $2\theta$ from the incident direction. For elastic scattering, $|\mathbf{k_i}| = |\mathbf{k_f}|$.

into the target material is

$$\hbar\mathbf{Q} = \hbar(\mathbf{k_i} - \mathbf{k_f}) \tag{3.1}$$

The quantity $\mathbf{Q}$ is the scattering vector. The relationship between $\mathbf{k_i}$, $\mathbf{k_f}$ and $\mathbf{Q}$ is shown in the scattering triangle (Fig. 3.4). The angle $2\theta$ shown in the scattering triangle is the angle by which the neutron is scattered from the direction of incident neutrons. Using the principle of conservation of energy, the energy transferred to the target material is

$$E = \frac{\hbar^2(k_i^2 - k_f^2)}{2m} \tag{3.2}$$

where, m is the mass of the neutron.

The angle of the scattered neutron can be calculated using the cosine rule.

$$Q^2 = k_i^2 + k_f^2 - 2k_i k_f \cos(2\theta) \tag{3.3}$$

For elastic neutron scattering measurements (e.g., neutron diffraction), $k_i = k_f$, which gives $|\mathbf{Q}| = 2k_i \sin(\theta) = \frac{4\pi \sin(\theta)}{\lambda}$ (Bragg's law).

The goal of a neutron scattering experiment is to measure the intensity of neutrons scattered (per incident neutron) by the sample as a function of energy and momentum transfer. The probability of scattered neutrons at a particular angle $\theta$, $\phi$ from the incident direction is expressed in terms of the scattering cross section ($\sigma$). If $\phi$ is the incident flux of incident neutrons, the partial differential cross section is defined as[81],

$$\frac{d^2\sigma}{d\Omega dE'} = \frac{N_{\theta,\phi,E'}}{\Phi d\Omega dE'} \tag{3.4}$$

where $N_{\theta,\phi,E'}$ is the number of neutrons scattered per second into a small solid angle dΩ along angle $\theta, \phi$ with final energy E, and dΩ is an angle subtended by the counter at the target.

The differential cross section can be obtained by integrating the above equation

$$\frac{d\sigma}{d\Omega} = \int_0^{\infty} (\frac{d^2\sigma}{d\Omega dE'}) dE' = \frac{N_{\theta,\phi}}{\Phi d\Omega} \tag{3.5}$$

where $N_{\theta,\phi}$ is the number of neutron scattered per second into solid angle dΩ along $\theta,\phi$ from incident beam.

In the language of quantum mechanics, the scattering of neutrons from a target nucleus causes a transition from an initial quantum state $|\,\mathbf{k_i}\lambda_i\rangle$ to a different quantum state $|\,\mathbf{k_f}\lambda_f\rangle$. Using the Born approximation, the probability that a neutron with an incident wave vector $\mathbf{k_i}$ interacts with a potential $V(\mathbf{r})$ and scatters with a wave vector $\mathbf{k_f}$ is proportional to

$$\Big|\int e^{i\mathbf{k_i}.\mathbf{r}} V(\mathbf{r}) e^{i\mathbf{k_f}.\mathbf{r}} d\mathbf{r}\Big|^2 = \Big|\int e^{i\mathbf{Q}.\mathbf{r}} V(\mathbf{r}) d\mathbf{r}\Big|^2 \tag{3.6}$$

where the potential $V(\mathbf{r})$ is the Fermi pseudo-potential given by,

$$V(\mathbf{r}) = \frac{2\pi\hbar^2}{m} \sum_j b_j \delta(\mathbf{r} - \mathbf{r}_j) \tag{3.7}$$

Here, $\delta(\mathbf{r})$ is a Dirac delta function, and $b_j$ is the scattering length. Van Hove determined that the differential scattering cross section can be written as[85]

$$\frac{d^2\sigma}{d\Omega dE_f} = \frac{k_f}{k_i} \frac{1}{2\pi\hbar} \sum_{i,j} b_i b_j \int_{-\infty}^{\infty} \mathrm{d}t \langle e^{-i\mathbf{Q}.\mathbf{r}_i(0)} e^{i\mathbf{Q}.\mathbf{r}_j(t)} \rangle e^{-iwt} \tag{3.8}$$

Here, the angular bracket ($\langle..\rangle$) represents a thermodynamic average over all the available states. The scattering function $S(Q,\omega)$ is related to the double scattering cross section by

$$S(Q,\omega) = \frac{1}{N} \frac{k_i}{k_f} \frac{d^2\sigma}{d\Omega dE_f} \tag{3.9}$$

Equation 3.8 implies that the intensity of scattering is proportional to the Fourier transform of a function that gives the probability of finding two atoms (or spins) at a certain distance at a given time. In practice, the dependence of the scattering

function on energy and $\mathbf{Q}$ can be compared to theoretical calculations and other measurements.

### 3.2.1 Elastic Neutron Scattering

The elastic diffraction of neutrons tells us how atoms or spins are periodically arranged in materials. In the elastic scattering process, neutrons do not exchange energy with the sample. Therefore, the scattered neutrons carry no information about the dynamics of the system.

Similar to x-ray diffraction, Bragg's law provides the condition for elastic neutron diffraction.

$$2d\sin(\theta) = n\lambda \tag{3.10}$$

Here, $d$ is the spacing of the planes, $\lambda$ is the wavelength, $\theta$ is the glancing angle of neutrons, and $n$ is an integer.

Considering only the scattering from nucleus, the intensity of scattered neutrons is proportional to the structure factor $S(\mathbf{Q})$[81],

$$S(\mathbf{Q}) = \frac{1}{N}\left|\sum_i^N b_i e^{(i\mathbf{Q}.\mathbf{r}_i)}\right|^2 \tag{3.11}$$

here, the sum is over all the atoms, and $b_i$ is the scattering length of an atom at position $\mathbf{r}_i$. In a crystalline material, the periodicity of the crystal structure implies that the structure factor is non zero only for the integral values of $h$, $k$ and $l$. Therefore, equation 3.11 can be written in the following form:

$$S(\mathbf{Q}) = \frac{2\pi}{nV}\sum_G \delta(\mathbf{Q}-\mathbf{G}_{hkl})\left|\sum_i^N b_i e^{(i\mathbf{Q}.\mathbf{r}_i)}\right|^2 \tag{3.12}$$

The delta function in this equation ensures that the intensity is peaked at $\mathbf{Q} = \mathbf{G}_{hkl}$. The peak in scattering intensity at $\mathbf{G}_{hkl}$ is commonly called the Bragg peak.

While a diffraction measurement is only intended for elastic measurements, a non-negligible contribution to the measurement arises due to the motion of atoms. If

$\mathbf{u}_i$ denotes the displacement of an atom located at $\mathbf{r}_i$, the structure factor in equation 3.12 is modified to the following[81],

$$S(\mathbf{Q}) = N\frac{(2\pi)^3}{v_0}\sum_G \delta(\mathbf{Q}-\mathbf{G}_{hkl})\,\Big|\sum_i^N b_i e^{(i\langle \mathbf{Q}.\mathbf{u}_i\rangle)} e^{(i\mathbf{Q}.\mathbf{r}_i)}\Big|^2 \tag{3.13}$$

here, the factor $e^{(i\langle \mathbf{Q}.\mathbf{u}_i\rangle)}$ is also called as Debye-Waller factor.

Neutron diffraction can be performed for a single crystal or a polycrystalline sample. For a single crystal diffraction measurement, the sample and detector are moved to achieve $\mathbf{Q} = \mathbf{G}_{hkl}$, and the intensities of different Bragg peaks are recorded. For the measurement of polycrystalline samples, the structure factor is averaged over all possible crystalline orientations. The Bragg peaks are observed at angles that satisfy the condition $|\mathbf{G}_{hkl}| = \frac{4\pi\sin(\theta)}{\lambda}$. The crystal structure is then determined by comparing model structures to the measured diffraction pattern.

### 3.2.2 Magnetic scattering

Magnetic neutron scattering results from the interaction of the magnetic moment of neutron with the magnetic field produced by unpaired electrons in the sample. If $\mathbf{B}(\mathbf{r})$ is the local magnetic field of unpaired electrons due to both the spin and the orbital moment of unpaired electrons, the interaction potential in reciprocal space can be obtained by a Fourier transform of $V_m(\mathbf{r})$.

$$V_m(\mathbf{Q}) = -\boldsymbol{\mu}_n.\mathbf{B}(\mathbf{Q}) \tag{3.14}$$

where $\boldsymbol{\mu}_n$ is the magnetic moment of neutron. Disregarding the detailed mathematical calculations, the component of the local magnetic field in reciprocal space becomes[81]

$$\mathbf{B}(\mathbf{Q}) = -\mu_0\hat{\mathbf{Q}}\times\mathbf{M}(\mathbf{Q})\times\hat{\mathbf{Q}} \tag{3.15}$$

Here, $\mathbf{M}$ is the Fourier transform of magnetization in momentum space. The quantity in the right side of above equation represents the component of magnetization perpendicular to the scattering vector $\mathbf{Q}$. The calculation of $\mathbf{M}(\mathbf{Q})$ is complicated; thus for most purposes, an approximation known as *dipole approximation* is adopted. The approximation for a $4f$ electron system gives magnetization in the following form:

$$\mathbf{M}(\mathbf{Q}) = -gJ\mu_B f(\mathbf{Q})\mathbf{J} \tag{3.16}$$

Here, $gJ$ is the Landé splitting factor. $f(\mathbf{Q})$ is known as *magnetic form factor*. The magnetic form factor represents the spatial distribution of magnetization inside the sample.

Following the equations 3.6 and 3.8, it appears that the form factor is squared in the partial difference cross section for the magnetic scattering. The form factor dependence of the cross section implies that the intensity of magnetic scattering decreases as a square of $f(Q)$. An exact derivation of $f(Q)$ is complicated and beyond the scope of this dissertation.

With the help of equations 3.8 and 3.9, the partial differential cross section for magnetic scattering; it can be written in the following form,

$$\left(\frac{d^2\sigma}{d\Omega dE_f}\right)_m = (\gamma r_0)^2 g^2 f^2(Q)\frac{k_f}{k_i} S_m^{\alpha\beta}(\mathbf{Q},E) \tag{3.17}$$

and

$$S_m^{\alpha\beta}(\mathbf{Q},E) = \sum_{\alpha\beta}(\delta_{\alpha\beta} - \hat{\mathbf{Q}}_\alpha\hat{\mathbf{Q}}_\beta)\delta(\mathbf{Q}-\boldsymbol{\tau}_m)\langle S_0^\alpha\rangle\langle s_t^\beta\rangle \tag{3.18}$$

The variables $\alpha,\beta$ represents the Cartesian components $x$, $y$ and $z$. The quantity $S_m^{\alpha\beta}(\mathbf{Q},E)$ is the Fourier transform of time dependent spin-spin correlation functions

The scattering function obtained from an INS measurement relates to the imaginary part of dynamic susceptibility by the *fluctuation dissipation theorem* by

$$\chi''(\mathbf{Q},E) = \pi\left(1-\mathrm{e}^{-E/k_BT}\right)S(\mathbf{Q},E) \tag{3.19}$$

where $\chi''$ is the imaginary part of generalized susceptibility $\chi = \chi' + i\chi''$. The quantity $(1 - e^{-E/k_B T})$ is the Bose factor.

Also, the real part of the dynamic susceptibility can be derived from the imaginary part using the Kramers-Kronig relation

$$\chi'(\mathbf{Q}, E) = \frac{1}{\pi} \int_{-\infty}^{\infty} \frac{\chi''(\mathbf{Q}, E')}{E'} dE' \tag{3.20}$$

Following equation 3.17 and 3.18, the scattering cross section for elastic magnetic scattering is expressed as

$$\left(\frac{d\sigma}{d\Omega}\right)_{em} = (\gamma r_0)^2 N \frac{(2\pi)^3}{V_{m0}} \frac{1}{2} g f(\mathbf{Q}))^2 e^{(-2w)} \sum_{\alpha\beta} (\delta_{\alpha\beta} - \hat{\mathbf{Q}}_\alpha \hat{\mathbf{Q}}_\beta) \delta(\mathbf{Q} - \boldsymbol{\tau}_m) \langle S_0^\alpha \rangle \langle s_l^\beta \rangle \tag{3.21}$$

where $\boldsymbol{\tau}_m$ represents the wave-vector of the magnetic sublattice.

Similar to nuclear scattering, the scattered neutrons from a magnetically ordered system constructively interfere to form a Bragg peak. The position of the magnetic Bragg peaks depends on the periodicity of the magnetic structure. The relative intensities of Bragg peaks depend on the magnitude and direction of unpaired electrons within the crystal structure. The condition for a magnetic Bragg peak is represented by the relation $\mathbf{Q} = \mathbf{G}_{hkl} \pm \boldsymbol{\tau}_m$, where $\boldsymbol{\tau}_m$ is the wave-vector of the magnetic sublattice. For example, for a simple antiferromagnetically ordered structure having a magnetic unit cell twice as large as the crystallographic unit cell, the magnetic Bragg peaks occur at half integer wave-vectors.

Some features of magnetic scattering are considerably different from nuclear scattering. First, magnetic scattering occurs due to electromagnetic interaction, which is a long ranged interaction. Therefore, the spatial distribution of magnetization therefore gives the form factor in the cross section of the magnetic scattering; hence the scattering intensity decreases with $Q$. In other words, scattering at a higher Brillouin zone is less intense as compared to scattering at the first Brillouin zone. On the other hand, nuclear scattering occurs via strong interaction,

which is a short range ($\sim 10^{-15}$ m) interaction. Second, magnetic scattering is strongly temperature dependent, whereas nuclear scattering is almost independent of temperature[‡]. Third, the magnetic scattering only captures the component of spins perpendicular to $\hat{\mathbf{Q}}$. All these differences are useful in discerning the source of scattering in a neutron diffraction measurement.

## 3.3 Instrumentation

Elastic and INS measurements were performed at three different neutron sources: The High Flux Isotope Reactor (HFIR) and the Spallation Neutron Source (SNS) located inside Oak Ridge National Laboratory (ORNL) at Oak Ridge, Tennessee, and the NIST Center for Neutron Research (NCNR) located at Gaithersburg, Maryland. Neutrons at the HFIR are produced by nuclear fission at the reactor; this is a conventional technique to produce neutrons for scattering experiments. The SNS utilizes a technique of neutron production called *spallation*. The spallation process begins with the production of protons from a particle accelerator. Pulses of protons strike a mercury based target system to release neutrons using spallation. The beam or pulse of neutrons produced from the source is moderated to optimize for the desired neutron energy.

A wide variety of the instruments are designed to address a diverse set of scientific problems. The instruments used in this study can be classified into two main categories: triple axis spectrometer (TAS) and time of flight (TOF) spectrometer. A brief description of these techniques and the instrument is in the following sections.

[‡]The only temperature dependent term in the scattering cross section (equation 3.13) is the Debye-Waller factor, which does not dramatically change the scattering cross section

### 3.3.1 Triple axis Spectrometers

TASs were initially designed and used by Bertram Brockhouse, who was later awarded a Nobel Prize in physics for his pioneering work. The phrase *Triple axis* refers to three different axes in the instrument: monochromator, sample, and analyzer. These three axes can be independently controlled for a measurement. The first axis, the monochromator, selects neutrons of specific energy from a polychromatic beam of neutrons produced by the reactor. A monochromator is crystal oriented at a specific angle that can select neutrons of a specific energy through Bragg diffraction. An ideal monochromator crystal is expected to have large scattering lengths, a small incoherent cross section, and a low neutron absorption coefficient. Several common monochromator materials include crystals of copper, silicon, beryllium, germanium, and pyrolytic graphite. The beam of neutrons diffracted from the monochromator is incident on the sample. The second axis is the crystallographic axis of the sample to be measured in an experiment. Generally, the rotation of the sample is restricted in a horizontal plane; therefore, crystals aligned in the specific scattering plane is desired. The sample scatters neutrons in different directions. Those neutrons are diffracted once more by the third axis – called an *analyzer* axis – which selects the final energy of the scattered neutrons. The analyzer is typically a crystal similar to the monochromator crystal and utilizes Bragg diffraction to choose neutrons having a specified energy to scatter to the detector.

Figure 3.5 is a schematic diagram of the TAS HB3 located at HFIR of ORNL. The instrument has three choices for monochromators. The most commonly used is a pyrolytic graphite monochromator that uses Bragg diffraction from the (002) plane. For a measurement at higher energies with high resolution, a beryllium monochromator with (101) reflection can be used. A third option is a silicon monochromator which reflects via (111) Bragg peak and is free from a higher order contamination. Additional filters can be used to remove higher order contamination

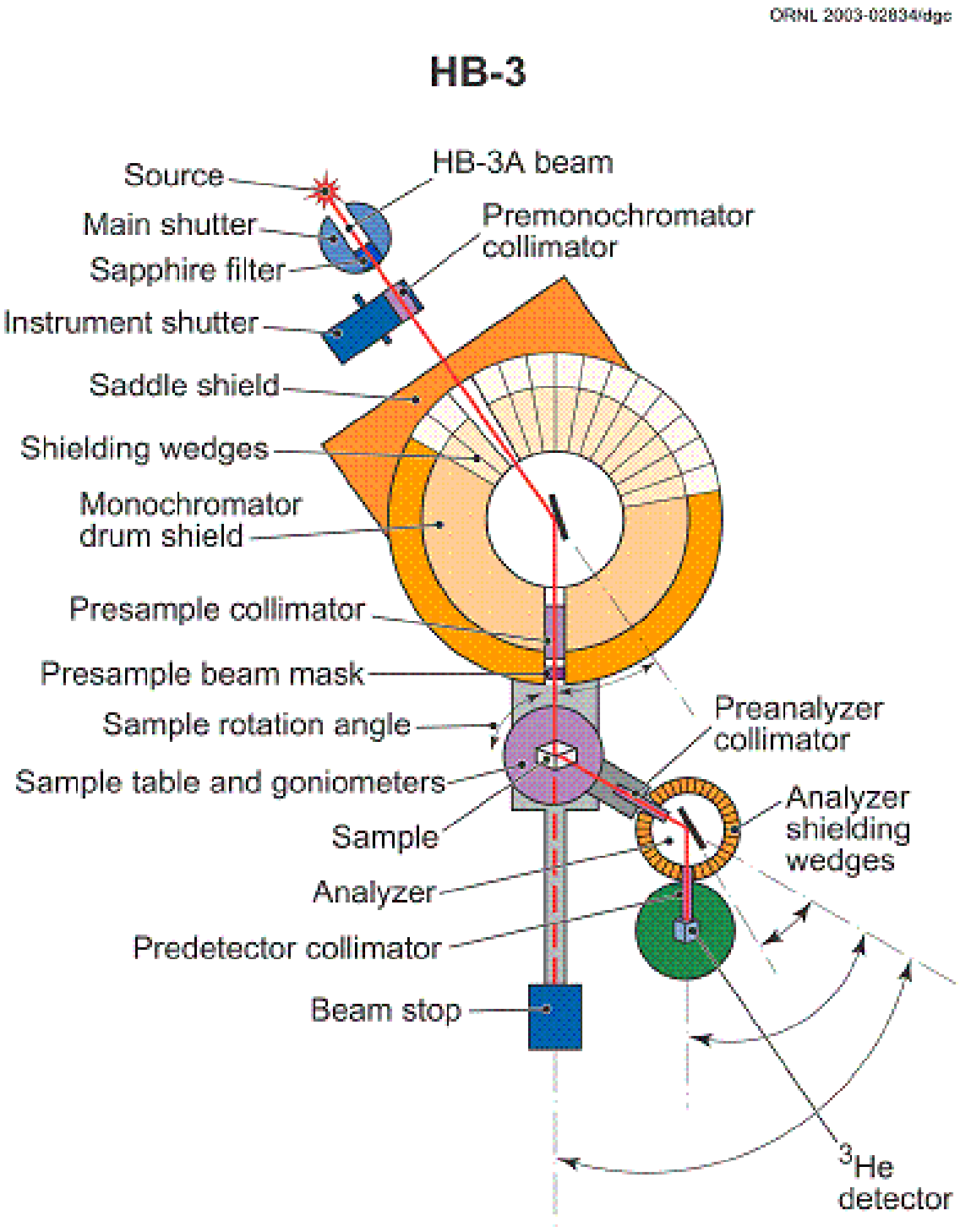



Figure 3.5: Schematic digam of HB3 spectrometer at HFIR of ORNL.

for pyrolytic graphite and beryllium monochromators. The instrument has four collimator positions arranged as shown in Fig. 3.5. Made of parallel blades of steel coated with cadmium, a collimator ensures that neutrons beyond a desired divergence are absorbed and eliminated from the beam. A tighter collimation increases the resolution of the instrument and in some cases lowers background, although at the expense of neutron intensity. Therefore, a proper combination of collimators should be chosen to optimize flux and resolution for each experiment.

The spectrometer can be moved to a specific value of $\mathbf{Q}$ and energy by computer controlled motors, and the intensity of scattered neutrons can be measured as a function of $\mathbf{Q}$ and energy. The measurement is performed either with a fixed incident wave-vector $\mathbf{k_i}$ while varying the scattered wave-vector $\mathbf{k_f}$ or a with fixed scattered wave-vector $\mathbf{k_f}$ while varying $\mathbf{k_i}$. In practice, scans with fixed-$\mathbf{k_f}$ are more commonly used.

### 3.3.2 Time of flight Spectroscopy

TOF spectroscopy is most commonly used with pulsed neutron sources. As the neutrons interact with the sample, they exchange energy and momentum with the sample. As a result, the velocity of the scattered neutron is changed and the neutron arrives at the detector at a different time. If the neutron loses energy, it spends more time during the flight; if it absorbs energy from the sample, it takes less time during the flight. The time of flight (i.e. the time taken by neutrons to travel from sample to detector) is used to calculate the energy lost by the neutron.

The initial energy of neutrons is selected by a chopper, which is made of neutron absorbing discs or cylinders with each having a slit or window. When the discs are rotated in a coupled way, only the neutrons having selected energy can pass through the discs. By varying the speed and phase of the discs, incident energy of neutrons can be controlled. The neutrons that pass through the chopper have almost equal energy.

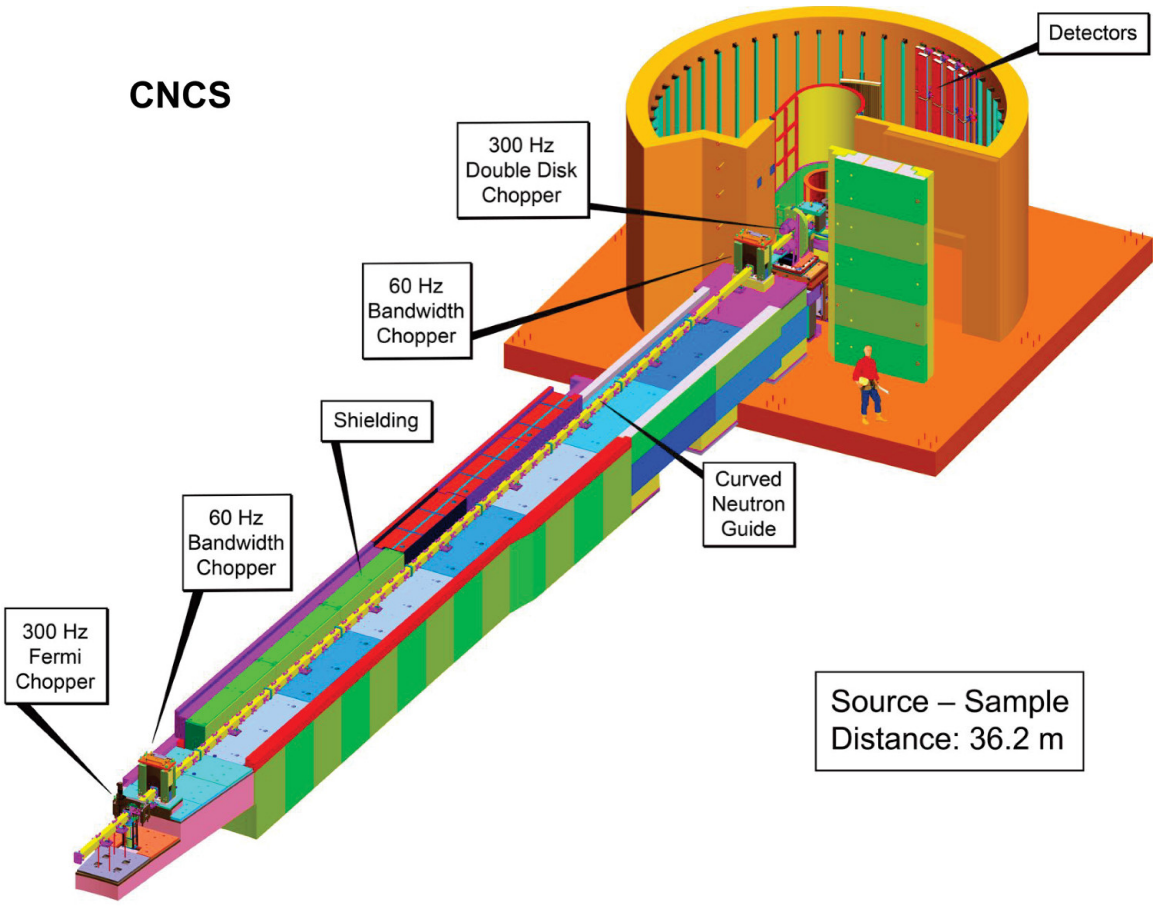



Figure 3.6: Schematic of the cold neutron chopper spectrometer (CNCS) at the SNS of ORNL, Oak Ridge, Tennessee. Picture taken from Ref. [11]

The cold neutron chopper spectrometer (CNCS) of SNS is an example of a TOF chopper spectrometer. The layout of the instrument is shown in the Fig. 3.6. There are four choppers that can be paired in several ways to control the energy of the incident neutron and the resolution of the instrument. The instrument consists of an approximately 35 m long neutron guide, in the middle of which is a curved section that transmits thermal and cold neutrons, but does not pass higher energy neutrons. The sample area is capable of holding heavy sample environment equipment. A curved array of detectors is 3.5 m away from the sample position. The detector array is made of 400 position sensitive $^{3}$He tubes that cover the scattering angles from -50° to 135°.

# Chapter 4

# Phase diagrams of $CeCu_{6-x}T_x$($T$ = Ag, Pd)

A similar version of this chapter is published as, "Structural and magnetic phase transitions in $CeCu_{6-x}T_x$ ($T = Ag, Pd$) ($T$ = Ag, Pd)", L. Poudel, C. de la Cruz, A. E. Payzant, A. F. May, M. Koehler, O. V. Garlea, A. E. Taylor, D. S. Parker, H. B. Cao, M. A. McGuire, W. Tian, M. Matsuda, H. Jeen, H. N. Lee, T. Hong, S. Calder, H. D. Zhou, M. D. Lumsden, V. Keppens, D. Mandrus and A. D. Christianson, Phys. Rev. B **92**, 214421 (2015) (Reference [86])

This chapter provides the details of structural and the magnetic properties of $CeCu_{6-x}Ag_x$ ($0 \leq x \leq 0.85$) and $CeCu_{6-x}Pd_x$ ($0 \leq x \leq 0.4$) as a function of Ag/Pd-composition. The structural and magnetic phase diagrams of $CeCu_{6-x}Ag_x$ and $CeCu_{6-x}Pd_x$ as a function of Ag/Pd composition are reported. The end member, $CeCu_6$, undergoes a structural phase transition from an orthorhombic ($Pnma$) to a monoclinic ($P2_1/c$) phase at 240 K. In $CeCu_{6-x}Ag_x$, the structural phase transition temperature ($T_s$) decreases linearly with Ag concentration and extrapolates to zero at $x_S \approx 0.1$. The structural transition in $CeCu_{6-x}Pd_x$ remains unperturbed with Pd substitution within the range of our study. The lattice constant $b$ slightly decreases with Ag/Pd doping, whereas, $a$ and $c$ increase with an overall increase in the unit cell

volume. Both systems, $CeCu_{6-x}Ag_x$ and $CeCu_{6-x}Pd_x$, exhibit a magnetic QCP, at $x \approx 0.2$ and $x \approx 0.05$ respectively. Near the QCP, long range antiferromagnetic ordering takes place at an incommensurate wave vector ($\delta_1$ 0 $\delta_2$) where $\delta_1 \sim 0.62$, $\delta_2 \sim 0.25$, $x = 0.125$ for $CeCu_{6-x}Pd_x$ and $\delta_1 \sim 0.64$, $\delta_2 \sim 0.3$, $x = 0.3$ for $CeCu_{6-x}Ag_x$. The magnetic structure consists of an amplitude modulation of the Ce-moments which are aligned along the $c$-axis of the orthorhombic unit cell.

## 4.1 Introduction

Understanding the nature of a QCP remains one of the most topical questions in condensed matter physics. As explained in the chapter 2, the HMM model is not sufficient to explain many properties observed in a number of systems near a QCP[23, 68, 87, 88, 89, 90], and a substantial subset of these systems are interpreted as hosting a "Local QCP"[23, 38, 68, 90, 91], where the breakdown of the Kondo-screening leaves the local-moments free to form a magnetic ground state. Probably, the most interesting example of the "local QCP" is the heavy fermion series $CeCu_{6-x}Au_x$ (x $\approx$ 0.1)[9, 24, 25, 54, 65]. In $CeCu_{5.9}Au_{0.1}$, the nature of the spin fluctuation is peculiar and not consistent with the conventional theory that successfully describes several aspects of many Ce-based heavy fermion materials[9, 24, 25, 54, 65].

While great attention has been given to the evolution of magnetic properties with Au doping into $CeCu_6$, less attention has been paid to the evolution of the structural properties. The $CeCu_{6-x}Au_x$ system exhibits a structural phase transition from orthorhombic ($Pnma$) to monoclinic ($P2_1/c$) that can be tuned by pressure or chemical doping[5, 7]. Previous studies have reported different values of the structural transition temperature ($T_s$) for the end member, $CeCu_6$, but are all within the range 168 K - 230 K[5, 7, 42, 92, 93]. In $CeCu_{6-x}Au_x$, $T_s$ decreases linearly with Au concentration and the structural phase transition disappears beyond the critical concentration, $x_S \approx 0.14$, which is close to the magnetic QCP, $x_{QCP} \approx 0.1$[7, 94].

Table 4.1: Lattice parameters and atomic coordinates at room temperature of a) $CeCu_6$, b) $CeCu_{5.7}Ag_{0.3}$ and c) $CeCu_{5.7}Pd_{0.3}$ obtained from Rietveld refinements of the structural model for the synchrotron x-ray measurements (See Fig. 4.1).

**a) $CeCu_6$**

$R_p$: 18.5 $R_{wp}$: 21.0 $R_{exp}$: 14.3 $\chi^2$: 2.1

a = 8.1105(1) b = 5.1000(1) Å c = 10.1622(2) Å

| Atom | Wyck. | x/a | y/b | z/c | Occupancy |
|---|---|---|---|---|---|
| Ce | 4*c* | 0.2595(4) | 0.2500 | 0.5646(4) | 1 |
| Cu1 | 8*d* | 0.0639(5) | 0.5085(12) | 0.3075(6) | 1 |
| Cu2 | 4*c* | 0.1469(8) | 0.2500 | 0.8597(6) | 1 |
| Cu3 | 4*c* | 0.3199(8) | 0.2500 | 0.2522(5) | 1 |
| Cu4 | 4*c* | 0.0604(10) | 0.2500 | 0.0993(7) | 1 |
| Cu5 | 4*c* | 0.4063(9) | 0.2500 | 0.0134(7) | 1 |

**b) $CeCu_{5.7}Ag_{0.3}$**

$R_p$: 14.2 $R_{wp}$: 16.1 $R_{exp}$: 9.43 $\chi^2$: 2.93

a = 8.1702(1) Å b = 5.0979(1) Å c = 10.2388(1) Å

| Atom | Wyck. | x/a | y/b | z/c | Occupancy |
|---|---|---|---|---|---|
| Ce | 4*c* | 0.2605(5) | 0.2500 | 0.5644(3) | 1 |
| Cu1 | 8*d* | 0.0631(5) | 0.5007(8) | 0.3119(3) | 1 |
| Cu2 | 4*c* | 0.1459(4) | 0.2500 | 0.8593(3) | 0.66(1) |
| Ag2 | 4*c* | 0.1459(4) | 0.2500 | 0.8593(3) | 0.34(1) |
| Cu3 | 4*c* | 0.3149(3) | 0.2500 | 0.2512(3) | 1 |
| Cu4 | 4*c* | 0.0608(4) | 0.2500 | 0.1006(4) | 1 |
| Cu5 | 4*c* | 0.4029(5) | 0.2500 | 0.0146(4) | 1 |

**c) $CeCu_{5.7}Pd_{0.3}$**

$R_p$: 15.9 $R_{wp}$: 27.9 $R_{exp}$: 9.4 $\chi^2$: 4.82

a = 8.13412(2) Å b = 5.09530(1) Å c = 10.19498(1) Å

| Atom | Wyck. | x/a | y/b | z/c | Occupancy |
|---|---|---|---|---|---|
| Ce | 4*c* | 0.2605(5) | 0.2500(0) | 0.5648(3) | 1 |
| Cu1 | 8*d* | 0.0641(6) | 0.5062(15) | 0.3093(6) | 0.96(2) |
| Pd1 | 8*d* | 0.0641(5) | 0.5062(15) | 0.3093(6) | 0.04(2) |
| Cu2 | 4*c* | 0.1443(8) | 0.2500 | 0.8583(6) | 0.80(2) |
| Pd2 | 4*c* | 0.1443(8) | 0.2500 | 0.8583(6) | 0.20(2) |
| Cu3 | 4*c* | 0.3167(9) | 0.2500 | 0.2528(5) | 1 |
| Cu4 | 4*c* | 0.0586(10) | 0.2500 | 0.0980(8) | 0.94(4) |
| Pd4 | 4*c* | 0.0586(10) | 0.2500 | 0.0980(8) | 0.06(4) |
| Cu5 | 4*c* | 0.4030(10) | 0.2500 | 0.0158(7) | 1 |

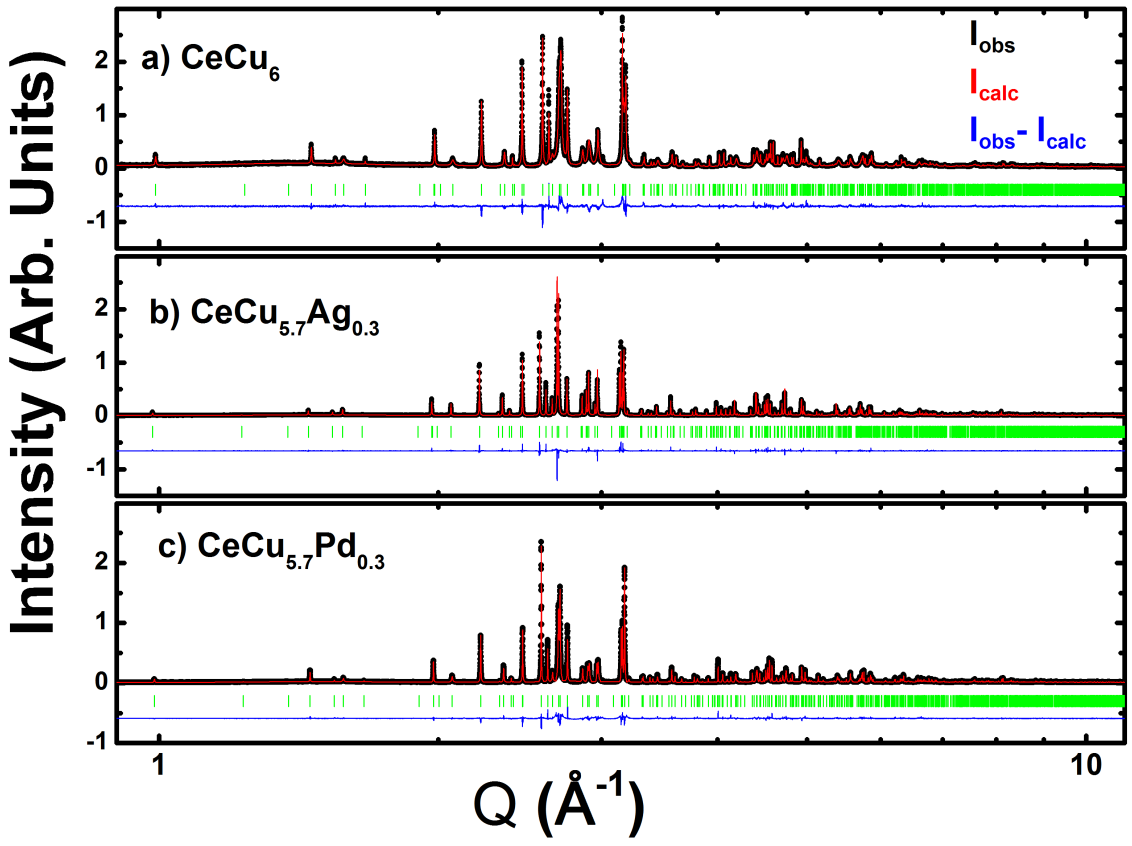



Figure 4.1: a) Room temperature x-ray powder diffraction pattern (black dots) plotted along with the Rietveld refinement (red line) for a) $CeCu_6$, b) $CeCu_{5.7}Ag_{0.3}$ and c) $CeCu_{5.7}Pd_{0.3}$. Vertical green marks are the positions of the structural reflections. The diffraction patterns were collected at beamline 11-BM at the advanced photon source (APS) of Argonne National Laboratory (ANL). The values of the refined parameters are tabulated in tables 4.1 and 4.2. The difference ($I_{obs}$ – $I_{calc}$) is offset for clarity. Note: the x-axis (Q) is in a logarithmic scale.

Moreover, one study indicates that the structural transition disappears and magnetic order emerges at nearly the same point in the phase diagram, raising the possibility that a quantum multi-critical point at $x^{S}_{QCP} \approx 0.13$ is the origin of the unusual quantum critical behavior in $CeCu_{6-x}Au_x$ [5]. Consequently, further investigation of the influence of the structural phase transition on the unconventional nature of the QCP in $CeCu_{6-x}Au_x$ is of interest.

Doping $CeCu_6$ with transition metals other than Au offers the opportunity to explore the nature of the QCP in an expanded parameter space where the structural and magnetic degrees of freedom can potentially be decoupled. For example, $CeCu_{6-x}Ag_x$[95, 96, 97], $CeCu_{6-x}Pd_x$[13], $CeCu_{6-x}Pt_x$[13] and $CeCu_{6-x}Sn_x$[67] all exhibit an antiferromagnetic order that evolves with doping. In the Ag/Pt/Pd-doped systems, deviation from Fermi-liquid behavior is reported at the QCP[12, 13, 98]. Furthermore, in $CeCu_{6-x}Ag_x$, thermal expansion measurements indicate that the divergence of the Grüneisen ratio is much weaker than that expected from the HMM model suggesting that the critical behavior is unconventional[14].

In this chapter, the first comprehensive neutron and x-ray diffraction investigation of the structural and magnetic properties of the $CeCu_{6-x}Ag_x$ and the $CeCu_{6-x}Pd_x$ systems are presented. The structural properties were studied using neutron diffraction, RUS, and x-ray diffraction measurements for different compositions of $CeCu_{6-x}Ag_x$ and $CeCu_{6-x}Pd_x$. Elastic neutron scattering measurements were performed for several members of $CeCu_{6-x}Ag_x$ and $CeCu_{6-x}Pd_x$ to build a detailed understanding of the evolution of the antiferromagnetic phase with doping. The Neel temperatures ($T_N$) obtained from neutron diffraction measurements in both systems are in agreement with previously published work[12, 13]. The values of $T_s$ in $CeCu_{6-x}Ag_x$ decrease linearly with Ag-composition, until the structural phase transition disappears at the critical concentration, $x_S \approx 0.1$. In $CeCu_{6-x}Pd_x$, no change in the structural transition temperature is observed for $0 \leq x \leq 0.4$.

## 4.2 Experimental Details

Single crystals and polycrystalline samples were synthesized for this study as described in the section 3.1.1 and 3.1.2. Some polycrystalline samples were annealed at 750°C for a week inside a silica tube back filled with argon. No change due to annealing was observed in the room temperature x-ray diffraction pattern or magnetization measurements.

For analysis of the antiferromagnetic phase, neutron diffraction measurements were performed on several compositions of $CeCu_{6-x}Ag_x$ (single crystals with $x$ = 0.3, 0.35, 0.4, 0.5, 0.75 and polycrystalline samples with $x$ = 0.65, 0.85) and $CeCu_{6-x}Pd_x$ (single crystals with $x$ = 0.125, 0.15, 0.4, and polycrystalline samples with $x$ = 0.25, 0.35, 0.4). Approximately 10 g of polycrystalline sample was used for each measurement. The polycrystalline samples were ground inside a glove box and held inside a cylindrical aluminium container loaded in a $^3$He refrigerator. The single crystal measurements were performed with ≈ 0.5 g samples. Each single crystal was pre-aligned using the neutron alignment station (CG-1B) at the HFIR of ORNL. All the samples were measured using the TASs HB-1A, HB-1, HB-3, and CG-4C at HFIR (ORNL) using fixed incident and final energies of 14.7 meV (HB-1A), 13.5 meV (HB-1), 14.7 meV (HB-3), and 5 meV (CG-4C). A dilution refrigerator provided the sample environment for these measurements.

The structural phase transitions were characterized using RUS, x-ray, and neutron diffraction. High-resolution synchrotron x-ray diffraction patterns were obtained at room-temperature for $CeCu_6$, $CeCu_{5.7}Ag_{0.3}$, and $CeCu_{5.7}Pd_{0.3}$ from 11-BM at APS of ANL using x-rays of incident wavelength, $\lambda \approx 0.41$ Å. X-ray diffraction patterns on polycrystalline samples of $CeCu_{6-x}Ag_x$ ($x$ = 0.015, 0.025, 0.065, 0.075) and $CeCu_{6-x}Pd_x$ ($x$ = 0.025, 0.25, 0.3) were collected using a PANalytical X'Pert Pro MPD powder diffractometer. Full patterns were collected at 300 K and 20 K, following which selected peaks were scanned from 10-300 K in 10 K steps for the characterization of the phase transition. To provide a clear distinction when

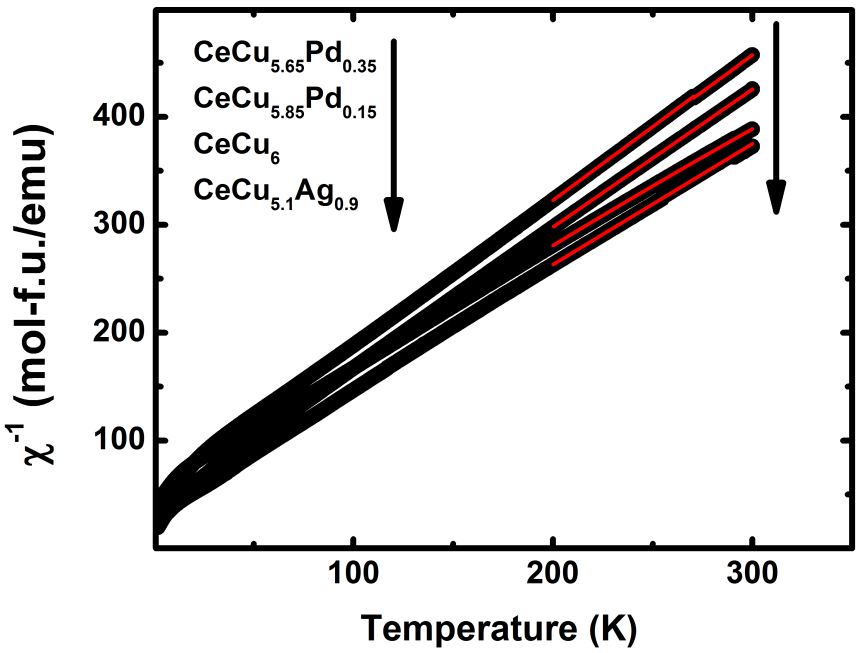



Figure 4.2: Inverse susceptibilities of $CeCu_{6-x}T_x$ (T = Ag, Pd) showing Curie-Weiss behavior. The red solid line is a Curie-Weiss fit to the data. The effective moments estimated from the Curie-Weiss fits are given in the text.

discussing the details of the crystal structure: a, b, and c are used for the lattice constants in the orthorhombic unit cell whereas $a_m$, $b_m$, and $c_m$ are used for the lattice constants in the monoclinic unit cell.

To further investigate structural properties, neutron diffraction measurements on polycrystalline samples of $CeCu_{6-x}Ag_x$ ($x$ = 0, 0.035, 0.1) and $CeCu_{6-x}Pd_x$ ($x$ = 0.05, 0.1, 0.4) were performed using the HB-2A powder diffractometer at HFIR using incident neutrons with wavelength of $\lambda$ = 1.54 Å. In each case, ~5 g of polycrystalline sample was held in a cylindrical vanadium can with Helium as an exchange gas. The vanadium can was loaded in a top loading closed cycle refrigerator. Diffraction patterns above and below $T_s$ were collected. A single crystal of $CeCu_{5.95}Ag_{0.05}$ was measured using the HB-3A four-circle diffractometer at HFIR with an incident wavelength of $\lambda$ = 1.003 Å. The temperature dependence of the several structural peaks was measured to estimate $T_s$.

The magnetic susceptibilities of several polycrystalline samples ($x$ = 0.05, 0.3, 0.9 and 1.2 of $CeCu_{6-x}Ag_x$, and $x$ = 0.05, 0.15, 0.25, 0.35 and 0.4 of $CeCu_{6-x}Pd_x$) were measured using a Quantum Design magnetic property measurement system (MPMS) between 2 K - 300 K with an applied field of 1 kOe. RUS measurements were obtained for polycrystalline samples of $CeCu_{6-x}Ag_x$ ($x$ = 0.025, 0.05, 0.09) using a custom-designed probe in a Quantum Design physical property measurement system (PPMS). The temperature dependence of the resonances was measured within the frequency range 500-1000 kHz.

Rietveld analysis of the x-ray and neutron diffraction patterns was performed using the FullProf software package[99]. A representational analysis was performed using SARAh[100] to illuminate symmetry allowed magnetic structures.

## 4.3 Results

### 4.3.1 Characterization

Energy-Dispersive x-ray Spectroscopy (EDS) analysis performed on several samples indicate that the samples are homogeneous and the elemental composition is in good agreement with their nominal values. Room-temperature laboratory x-ray diffraction was used for phase identification and as a check of sample purity. Synchrotron x-ray diffraction measurements on the sample compositions noted above were utilized as an additional check of the phase purity of the samples. The only evidence of an impurity phase in the samples studied here is the presence in the synchrotron x-ray diffraction patterns of a single unidentified peak smaller than 0.25% of the most intense structural peak of $CeCu_6$. This peak was not observed in the neutron diffraction or the laboratory x-ray measurements.

DC magnetic susceptibility measurements of several samples are shown in Fig. 4.2. A linear dependence of the inverse magnetic susceptibility is observed over a large region of temperature indicating Curie-Weiss behavior. Using the Curie-Weiss relation, $\chi = \chi_0 + \frac{N_A \mu_{eff}^2}{3k_B(T-\theta_{CW})}$, the effective values of the magnetic moment are estimated from the fits of susceptibility data between 200 K – 300 K. The magnetic moments for different compositions of $CeCu_{6-x}T_x$ (T = Ag, Pd) are close to the expected value ($\mu_{eff}$ = 2.54 $\mu_B$) of the $Ce^{3+}$ moment and are 2.42(1) $\mu_B$, 2.43(1) $\mu_B$, 2.67(1) $\mu_B$ and 2.50(1) $\mu_B$ for $CeCu_6$, $CeCu_{5.65}Pd_{0.35}$, $CeCu_{5.1}Ag_{0.9}$ and $CeCu_{5.85}Pd_{0.15}$ respectively.

### 4.3.2 Neutron & x-ray Diffraction

The crystal structure of $CeCu_6$ is known to be orthorhombic with space group $Pnma$ at room-temperature[4, 60]. The orthorhombic unit cell consists of one general 8$d$ site and five 4$c$ sites. The Cerium atoms occupy one of the 4$c$ positions whereas the Cu atoms are distributed among the general 8$d$ and four 4$c$ sites[4, 60]. This

Table 4.2: Structural parameters of $CeCu_{6-x}T_x$ ($T$ = Ag, Pd) extracted from diffraction measurements at room temperature. The lattice parameters were obtained from Rietveld analysis.

| | $x$ | | a (Å) | b (Å) | c (Å) | Volume (Å$^3$) |
|---|---|---|---|---|---|---|
| $CeCu_6$ | | x-ray | 8.1105(1) | 5.1010(1) | 10.1622(2) | 420.43(1) |
| $CeCu_{6-x}Ag_x$ | 0.035 | neutron | 8.1215(9) | 5.0976(6) | 10.1775(8) | 421.35(3) |
| | 0.1 | neutron | 8.1266(6) | 5.0972(3) | 10.1846(5) | 421.87(2) |
| | 0.3 | x-ray | 8.1702(1) | 5.0979(1) | 10.2388(1) | 426.46(1) |
| $CeCu_{6-x}Pd_x$ | 0.05 | neutron | 8.1103(6) | 5.0998(4) | 10.1649(3) | 420.43(2) |
| | 0.1 | neutron | 8.1177(8) | 5.0996(5) | 10.1727(9) | 421.11(3) |
| | 0.3 | x-ray | 8.1341(2) | 5.0953(1) | 10.1950(1) | 422.54(1) |
| | 0.4 | neutron | 8.1444(8) | 5.0899(4) | 10.2042(8) | 423.01(2) |

crystal structure is used as a model for the analysis of the diffraction patterns of $CeCu_{6-x}Ag_x$ and $CeCu_{6-x}Pd_x$. All the compositions of $CeCu_{6-x}Ag_x$ and $CeCu_{6-x}Pd_x$ that are studied here are isomorphous to the parent compound $CeCu_6$ at room temperature. The lattice parameter $b$ slightly decreases with Ag/Pd substitution while the parameters $a$ and $c$ increase along with an overall expansion of the unit cell volume in both systems. The synchrotron x-ray diffraction patterns and the fit obtained from the Rietveld refinements of $CeCu_6$, $CeCu_{5.7}Ag_{0.3}$ and $CeCu_{5.7}Pd_{0.3}$ are shown in Fig. 4.1, and the results of the fit are summarized in Tables 4.1 and 4.2.

The coherent neutron scattering lengths of the dopants, Ag (= 5.92 fm) and Pd (= 5.91 fm), are close to that of copper (= 7.72 fm). This low contrast coupled with the small amount of dopants present renders the determination of the site occupancy with neutron scattering inconclusive. Therefore, high-resolution synchrotron x-ray diffraction was used for this purpose. Rietveld refinement of the synchrotron x-ray diffraction measurement indicates that the Ag-atoms in $CeCu_{6-x}Ag_x$ are not distributed between different copper sites, but prefer the Cu2 site of the $Pnma$ structure. This is similar to $CeCu_{6-x}Au_x$ system, where Au-atoms occupy the Cu2 site until the site is fully occupied[60, 101]. A different situation occurs in $CeCu_{6-x}Pd_x$, where the Pd-atoms occupy multiple Cu sites. The analysis of the synchrotron x-ray diffraction pattern shows that the majority of the Pd atoms occupy

the Cu2 site and the remaining Pd atoms are distributed on Cu1 and Cu4 sites. The precise value of the Pd-occupancies on all other sites except Cu2 is difficult to determine as the occupancies on these sites are very small and are near the limit of what is possible for this analysis. The Pd-occupancies that give the best fit of the diffraction pattern are shown in Fig. 4.1(c) and are tabulated in the Table 4.1(b).

### 4.3.3 Structural Phase Transitions

Fig. 4.3 illustrates the different methods used for the characterization of the structural phase transitions: x-ray diffraction, neutron diffraction, and RUS. To check the consistency in these measurements and the quality of the samples, $CeCu_{5.95}Ag_{0.05}$ was grown in both polycrystalline and single crystal forms and measured by all three techniques. A small part of the Czochralski-grown single crystal was measured with neutron diffraction, and different batches of the polycrystalline samples were measured by x-ray diffraction and RUS. The transition temperature ($T_s$) of $CeCu_{5.95}Ag_{0.05}$ was estimated to be at $T_s$ = 125(1) K using neutron diffraction. The RUS and x-ray diffraction measurements of the polycrystalline $CeCu_{5.95}Ag_{0.05}$ yield $T_s$ = 122(1) K and $T_s$ = 125(5) K respectively. This attests to the consistency of the measurement techniques.

The monoclinic order parameter ($(a_m c_m \cos(\beta))^2$) changes smoothly with temperature near $T_s$ (Fig. 4.4). The structural peaks that are indexed as (h k l) in space group $Pnma$ split into two structural peaks which are indexed as ( – k l h) and (k l h) in the monoclinic space group $P2_1/c$. The splitting of the structural peaks at $T_s$ can be explicitly observed in the temperature dependence of the diffraction pattern as shown in Fig. 4.3(a), where the peaks in $Pnma$ phase split into $P2_1/c$-peaks as (1 2 2) → (– 2 2 1) + (2 2 1), (2 2 0) → ( – 2 0 2) + (2 0 2) and (2 2 1) → ( – 2 1 2) + (2 1 2). The splitting of these peaks is also confirmed by single crystal neutron diffraction measurements, a part of which is shown in Fig. 4.3(b).

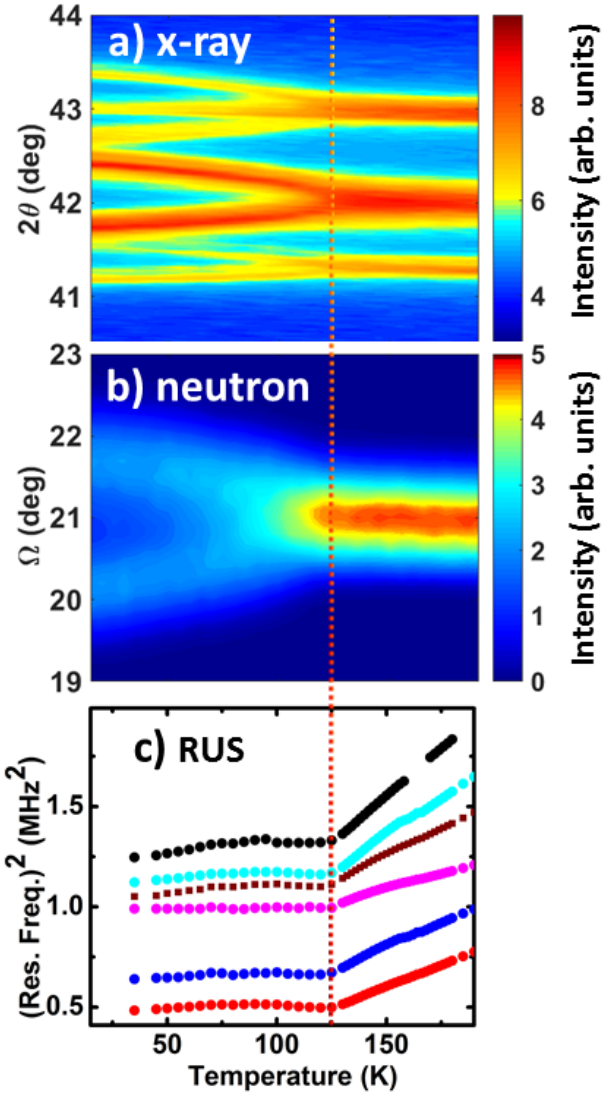



Figure 4.3: The structural transition of $CeCu_{5.95}Ag_{0.05}$ characterized using a) powder x-ray diffraction with wavelength, $\lambda \approx 1.54$ Å: The (122), (220) and (221) structural peaks in the orthorhombic phase split in the monoclinic phase as described in the text. Note that peaks indexed as (h 0 l) or (0 k l) in the orthorhombic phase are unaltered, aside from a change of indexing, by the monoclinic distortion. b) Single crystal neutron diffraction with $\lambda \approx 1.003$ Å: The structural peak (2 2 0) of orthorhombic phase splits into two structural peaks (2 0 2) and (– 2 0 2) of monoclinic phase at $T_S$. c) RUS: the square of the resonant frequencies change slope at $T_s$. A vertical line in the plot shows $T_s$. All measurements indicate that the structural phase transition takes place in $CeCu_{5.95}Ag_{0.05}$ at $T_S \approx 125(5)$ K.

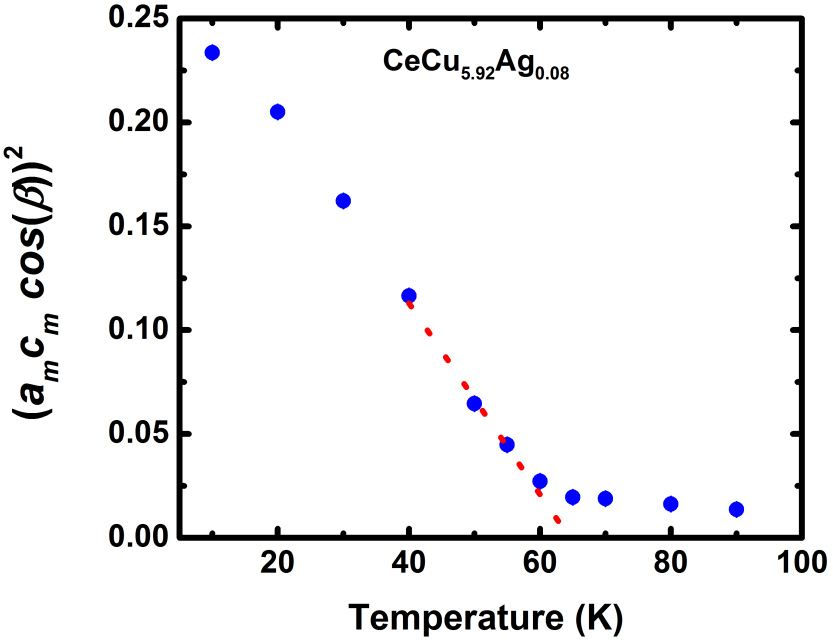



Figure 4.4: Monoclinic order parameter ($(a_m c_m \cos(\beta))^2$) of $CeCu_{5.92}Ag_{0.08}$ obtained from neutron diffraction measurements. An extrapolation of the order parameter gives $T_s$ = 62(3) K. A continuous change in the monoclinic order parameter is observed near $T_S$.

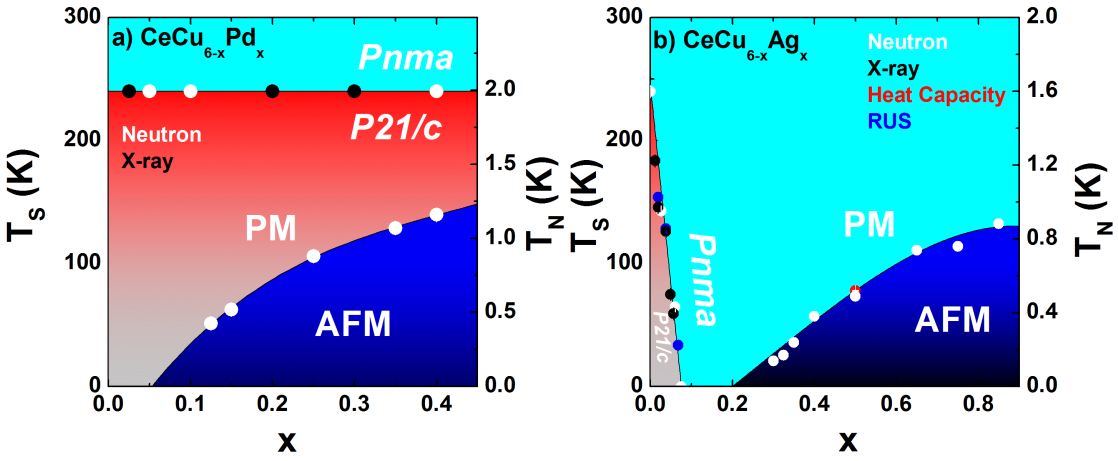



Figure 4.5: The phase diagrams of a) $CeCu_{6-x}Pd_x$ and b) $CeCu_{6-x}Ag_x$. The concentration for the occurrence of the magnetic QCP is taken to be the same as in [12, 13] and is $x_{QCP} \approx 0.2$ for $CeCu_{6-x}Ag_x$ and $x_{QCP} \approx 0.05$ for $CeCu_{6-x}Pd_x$. In $CeCu_{6-x}Ag_x$, the termination of the structural phase transition occurs at $x_S \approx 0.1$. No suppression of the structural phase transition was observed in $CeCu_{6-x}Pd_x$ for $x \leq 0.4$.

RUS measurements are one of the most sensitive ways of characterizing structural phase transitions. The resonances occur as the natural frequency of the sample, which is closely related to its elastic properties, matches the incident ultrasonic wave. At $T_s$, the change in the elastic properties of the sample indicates the occurrence of the structural phase transition. Here, the temperature dependence of the square of the resonant frequency is used to show the structural phase transition. As shown in Fig. 4.3(c), the square of the resonant frequency versus temperature has a constant slope above $T_s$. The slope of the curve changes continuously at $T_s$, and the shift in the resonances below $T_s$ are much weaker as compared to those at above $T_s$.

The work presented here indicates the structural phase transition from orthorhombic to monoclinic phase in $CeCu_6$ occurs at $T_s \approx 240$ K, which is somewhat larger compared to the previous studies[42, 43, 92]. The values of $T_s$ in $CeCu_{6-x}Ag_x$ drop linearly with Ag concentration until the structural phase transition disappears above the critical composition, $x_S \geq 0.1$(Fig. 4.5(b)). For $0.1 \leq x \leq 0.85$, no structural phase transition was observed above 4 K. The suppression of the structural phase transition due to doping is analogous to $CeCu_{6-x}Au_x$, where $T_s$ drops in similar fashion and the termination of the structural phase transition occurs at a similar Au-composition, $x_S \approx 0.14$[5, 7]. However, in $CeCu_{6-x}Pd_x$, no change in $T_s$ is observed with Pd-substitution within the range of our investigation, ($0 \leq x \leq 0.4$). The changes in the transition temperatures with doping in $CeCu_{6-x}Ag_x$ and $CeCu_{6-x}Pd_x$ are summarized in the phase diagrams presented in Fig. 4.5.

### 4.3.4 First Principles Calculations

To understand the structural phase transitions, my collaborators performed first principles calculations using the planewave code WIEN2K [102]. The generalized gradient approximation (GGA) of Perdew, Burke and Ernzerhof [103] was used, with sphere radii for the undoped compound of 2.21 Bohr for Cu and 2.50 for Ce. For the undoped compound, the lattice parameters and angles of the orthorhombic and

Table 4.3: The relative energies of several configurations for Ag and Pd doping.

| Configuration | Δ E (meV/u.c.) |
|---|---|
| Ag doping – orthorhombic | 0 |
| Ag doping – orthorhombic SP | -4 |
| Ag doping – monoclinic | +95 |
| Ag doping – monoclinic SP | +92 |
| Pd doping (Cu2) - orthorhombic | 0 |
| Pd doping (Cu2) - orthorhombic SP | +1 |
| Pd doping (Cu2)- monoclinic | +74 |
| Pd doping (Cu2) - monoclinic SP | + 73 |
| Pd doping (Cu1) - orthorhombic | 0 |
| Pd doping (Cu1) - monoclinic | + 82 |

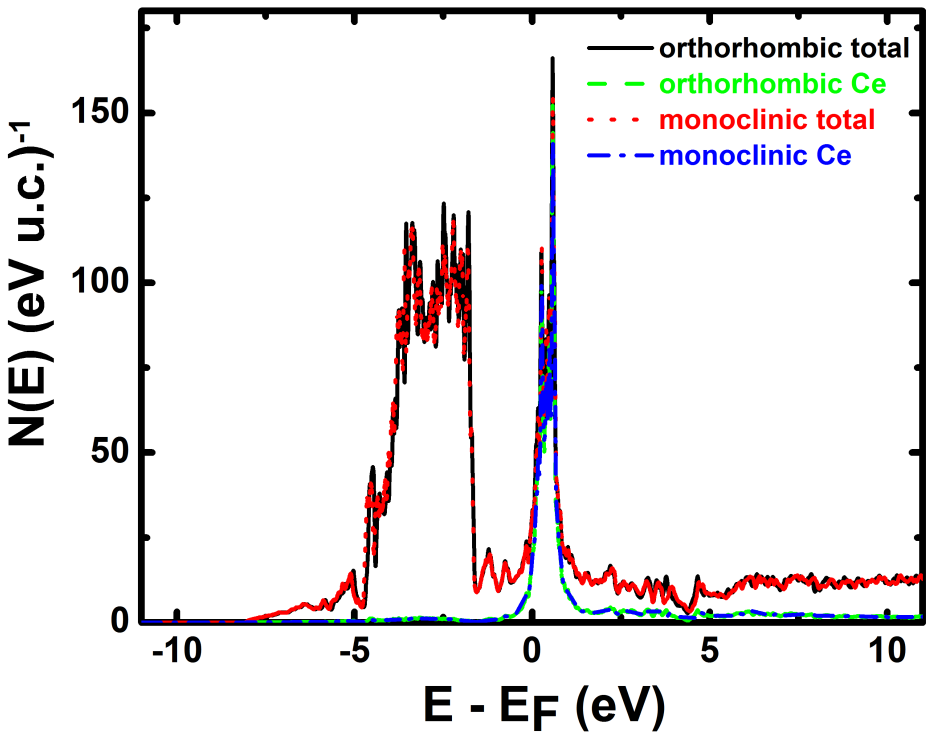



Figure 4.6: The calculated DOS of $CeCu_6$ in the orthorhombic and monoclinic structures.

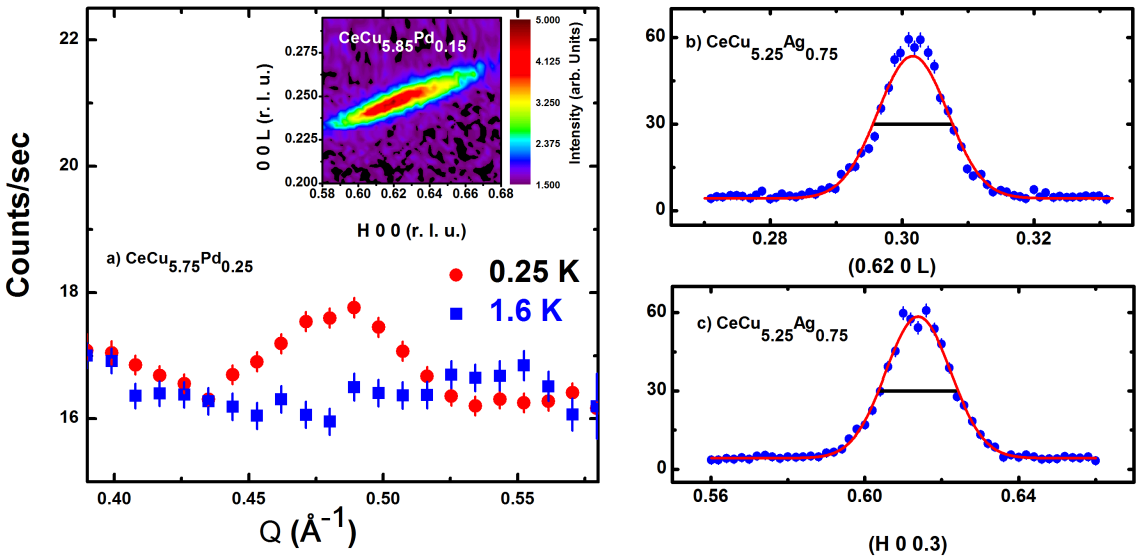



Figure 4.7: a) The magnetic reflection at Q = 0.480(3) from a polycrystalline sample with a composition of $CeCu_{5.75}Pd_{0.25}$. The inset shows the magnetic reflection from a a single crystal of $CeCu_{5.85}Pd_{0.15}$ near the wave vector $\mathbf{Q}$ = (0.6243(1) 0 0.2503(1)). b) and c) Single crystal diffraction measurement of the the (0.62 0 0.3) magnetic reflection of $CeCu_{5.25}Ag_{0.75}$ along (0.62 0 L) and (H 0 0.3) at 0.05 K. The red line is a Gaussian fit to the data constrained by the instrumental resolution. The horizontal black lines are the calculated instrumental resolution.

Table 4.4: Compositional dependence of the magnetic wave vector in $CeCu_{6-x}Ag_x$ and $CeCu_{6-x}Pd_x$.

| **$CeCu_{6-x}Ag_x$** | | |
|---|---|---|
| x | **Q** (h k l) [r.l.u.] | $\|Q\|$ ($Å^{-1}$) |
| 0.85 | — | 0.499(2) |
| 0.75 | (0.615(1) 0 0.302(1)) | 0.504(1) |
| 0.65 | — | 0.501(2) |
| 0.50 | (0.633(1) 0 0.296(1)) | 0.522(1) |
| 0.40 | (0.641(1) 0 0.301(1)) | 0.521(1) |
| 0.35 | (0.645(2) 0 0.300(1)) | 0.518(1) |
| 0.30 | (0.646(1) 0 0.297(1)) | 0.529(1) |
| **$CeCu_{6-x}Pd_x$** | | |
| x | **Q** (h k l) [r.l.u.] | $\|Q\|$ ($Å^{-1}$) |
| 0.40 | (0.577(1) 0 0.228(1)) | 0.469(1) |
| 0.40 | — | 0.449(3) |
| 0.35 | — | 0.466(6) |
| 0.25 | — | 0.480(4) |
| 0.15 | (0.624(1) 0 0.250(1)) | 0.509(1) |
| 0.125 | (0.624(1) 0 0.253(1) | 0.510(1) |

monoclinic phases reported by Asano *et al.* has been used[104], and relaxed the internal coordinates until forces were less than 2 mRyd/Bohr.

For the calculations of Ag and Pd doping, several assumptions were made. As detailed in Table 4.2, in the high temperature orthorhombic phase, for a doping level $x = 0.1$, the structures for $CeCu_{5.9}Ag_{0.1}$ and $CeCu_{5.9}Pd_{0.1}$ are very similar, differing in volume by less than 0.2%. Since even at this doping level the observed low-temperature structures are very different (orthorhombic for Ag doping, monoclinic for Pd doping), the effect of charge doping was isolated from the small structural differences by using the same lattice parameters and internal coordinates for Ag doping and Pd doping. In each case, one of the 24 Cu atoms in the unit cell was replaced by Cu or Pd. Since there is a substantial site preference for Ag doping in this case, the Cu2 site was used for the substitution. For Pd doping, two separate sets of calculations were done, with the Pd atom at the Cu1 and Cu2 sites.

For $CeCu_6$, the monoclinic structure has an energy 33 meV per unit cell lower than the orthorhombic structure, consistent with experimental observation. Despite this energy difference, the changes in electronic structure are scant. Figure 4.6 plots the calculated densities-of-states (DOS). In both cases, there is a DOS peak slightly above the Fermi level, attributable to the Ce states, along with a large contribution between 2 and 5 eV beneath $E_F$. The Fermi level DOS, at 31.53/eV - u.c. for the orthorhombic cell and 30.82/eV - u.c. for the monoclinic, changes by only 2%.

The relative energies of the doped compounds are presented in table 4.3. The non-spin polarized (NSP) orthorhombic state was chosen as the zero of energy. To make the spin-polarized (SP) calculations tractable, a ferromagnetic Ce configuration was used rather than the actual antiferromagnetism. The calculations correctly predict the suppression of the monoclinic state with Ag doping - the monoclinic state lies 95 meV higher in energy than the orthorhombic state, and including spin polarization does not appreciably change this result. The spin polarized (SP) orthorhombic state, with Ce moment 0.34 $\mu_B$, is the groundstate, 4 meV beneath the NSP orthorhombic state and well below both monoclinic states.

In contrast to the experiment, the calculations predict a suppression of the monoclinic state in $CeCu_{6-x}Pd_x$ system. For Pd doping on the Cu2 site this state is 74 meV above the orthorhombic state, and including spin polarization does not remedy this. A similar result is obtained for doping on the Cu1 site (spin polarization was not checked), with an 82 meV energy difference.

While the reason for this disagreement is not known, it likely arises from the heavy fermion state, which tends to confound mean-field based density functional theory (DFT). For example, for the base $CeCu_6$, our calculated T-linear specific heat coefficient $\gamma$ is 18.2 mJ/mol-$K^2$, much smaller than the observed value of between 840 and 1600 mJ/mol-$K^2$ [105]. However, since the calculations correctly predict the ground state of $CeCu_6$, and that for Ag doping, one still has hope for the ability of first principles calculations to describe this system.

One plausible way forward would be to explicitly include correlations through an LDA+U approach or an LDA+DMFT approach, as considered by Shim *et al* [106] for $CeIrIn_5$. Such approaches would likely tend to yield effective masses in better agreement with experiment, as well as more accurate related quantities such as the relative energies of the orthorhombic and monoclinic states. LDA+DMFT approaches have been applied, with a fair degree of success, to structural properties of Ce itself [107, 108, 109, 110] and it is anticipated that similar success can be achieved with LDA+DMFT in studying Ag and Pd doping of $CeCu_6$.

### 4.3.5 Magnetic Phase Transitions

Using the information obtained from the study of the polycrystalline samples together with the $CeCu_{6-x}Au_x$ literature, magnetic reflections in the (h 0 l) scattering plane were measured in $CeCu_{6-x}Ag_x$ and $CeCu_{6-x}Pd_x$ (for example see Fig. 4.7). For simplicity and ease of comparison with the work presented here on $CeCu_{6-x}Ag_x$ as well as the extensive work on $CeCu_{6-x}Au_x$, the small monoclinic distortion (less

than 2°) in $CeCu_{6-x}Pd_x$ is neglected and orthorhombic notation is used to discuss the magnetic properties.

The magnetic Bragg reflections occurs at the points in the reciprocal space that satisfies the condition $\mathbf{Q} = \boldsymbol{\tau} \pm \mathbf{k_i}$ (i = 1, 2), where $\boldsymbol{\tau}$ represents a nuclear reciprocal lattice vector and $\mathbf{k_i}$ are the incommensurate propagation vector, $\mathbf{k_1}$ = (0.62 0 0.3) , or the symmetry equivalent $\mathbf{k_2}$ = (0.62 0 −0.3). The magnetic propagation vector for $CeCu_{6-x}Ag_x$ is only weakly dependent on composition. The change in the magnitude of the propagation vector with doping appears to be more pronounced in $CeCu_{6-x}Pd_x$ as presented in Table 4.4.

The intensity of a structural or a magnetic peak collected with a triple-axis instrument is the convolution of the Bragg intensity with the instrumental resolution function. The software package ResLib[111] was utilized to estimate the instrumental resolution and thereby enable the extraction of resolution corrected intensities using the Cooper-Nathans approximation[112]. For $CeCu_{5.25}Ag_{0.75}$ the calculated instrumental resolution is indicated by the horizontal lines in Fig. 4.7(b) and 4.7(c). The instrumental resolution is not isotropic in the scattering plane and results in an elliptically shaped Bragg peak (e.g. inset of Fig. 4.7(a). The magnetic Bragg peaks observed for all compositions are found to be resolution limited, consistent with the presence of the long range magnetic order.

Table 4.5: Basis vectors from representational analysis of space group $Pnma$ with $\mathbf{k}$ = (0.62, 0, 0.3). The Ce-site is separated into four orbits given by 1: (0.2586, 0.25, 0.5636), 2: (0.2414, 0.75, 0.06360), 3: (0.7414, 0.75, 0.4364), 4: (0.7586, 0.25, 0.9364). The decomposition of the magnetic representation for each of the four orbits is $\Gamma_{Mag} = 1\Gamma_1^1 + 2\Gamma_2^1$. Symbols $m_{\parallel a}$ $m_{\parallel b}$ $m_{\parallel c}$ denote the projection of the magnetic moment along the $a$, $b$ and $c$-axis respectively.

| IR | BV | BV components | | | | | |
|---|---|---|---|---|---|---|---|
| | | $m_{\parallel a}$ | $m_{\parallel b}$ | $m_{\parallel c}$ | $im_{\parallel a}$ | $im_{\parallel b}$ | $im_{\parallel c}$ |
| $\Gamma_1$ | $\boldsymbol{\psi}_1$ | 0 | 1 | 0 | 0 | 0 | 0 |
| $\Gamma_2$ | $\boldsymbol{\psi}_2$ | 1 | 0 | 0 | 0 | 0 | 0 |
| | $\boldsymbol{\psi}_3$ | 0 | 0 | 1 | 0 | 0 | 0 |

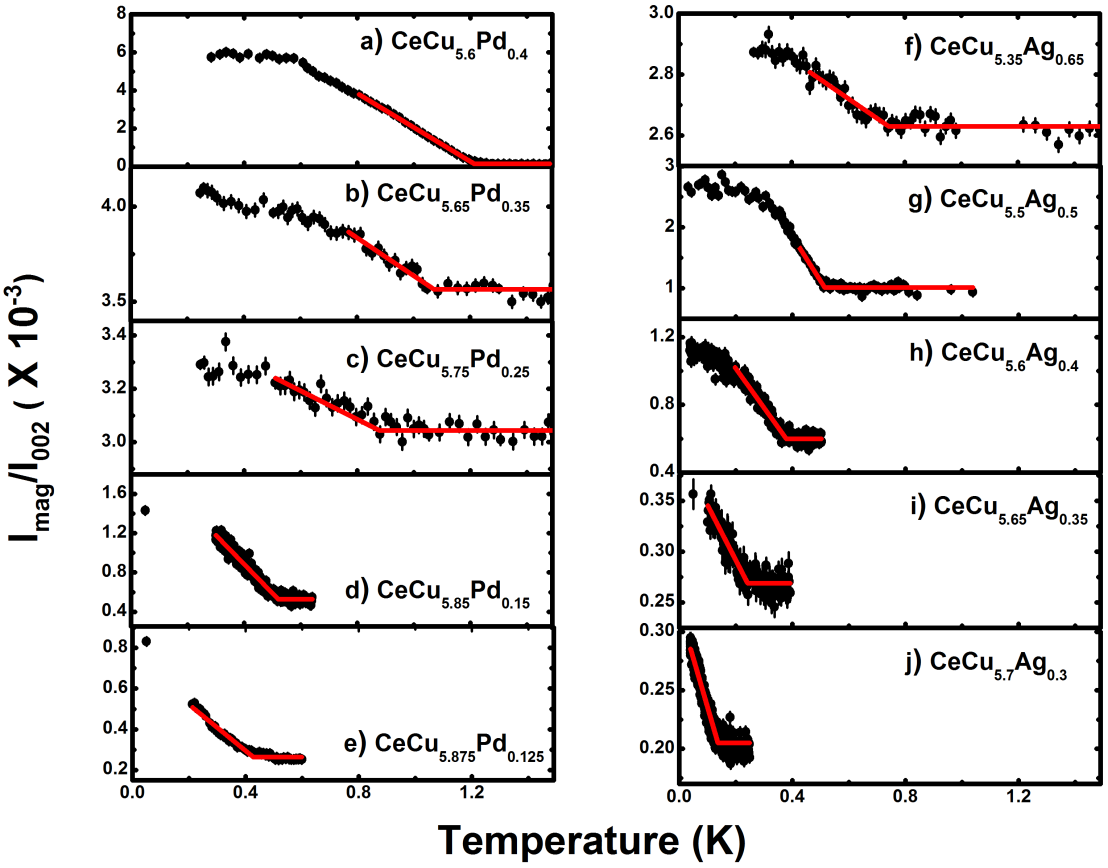



Figure 4.8: Temperature dependence of the intensity of the magnetic peak ((0.62 0 0.25) for $CeCu_{6-x}Pd_x$ and (0.64 0 0.3) for $CeCu_{6-x}Ag_x$) normalized to the structural (0 0 2) peak in (a-e) $CeCu_{6-x}Pd_x$ and (f-j) $CeCu_{6-x}Ag_x$. The red line is a fit to the the data with a power law equation of the form $y = y_0 + A(T - T_N)^{2\beta}$. $\beta$ was fixed to the mean field value of 0.5 and $T_N$ was allowed to vary in order to estimate the transition temperature. The estimated values of $T_N$ are a) 1.20(1) K, b) 1.07(2) K, c) 0.88(3) K, d) 0.52(1) K, e) 0.43(1) K, f) 0.74(2) K, g) 0.51(1) K, h) 0.38(1), i) 0.24(1) K, j), and 0.14(1) K.

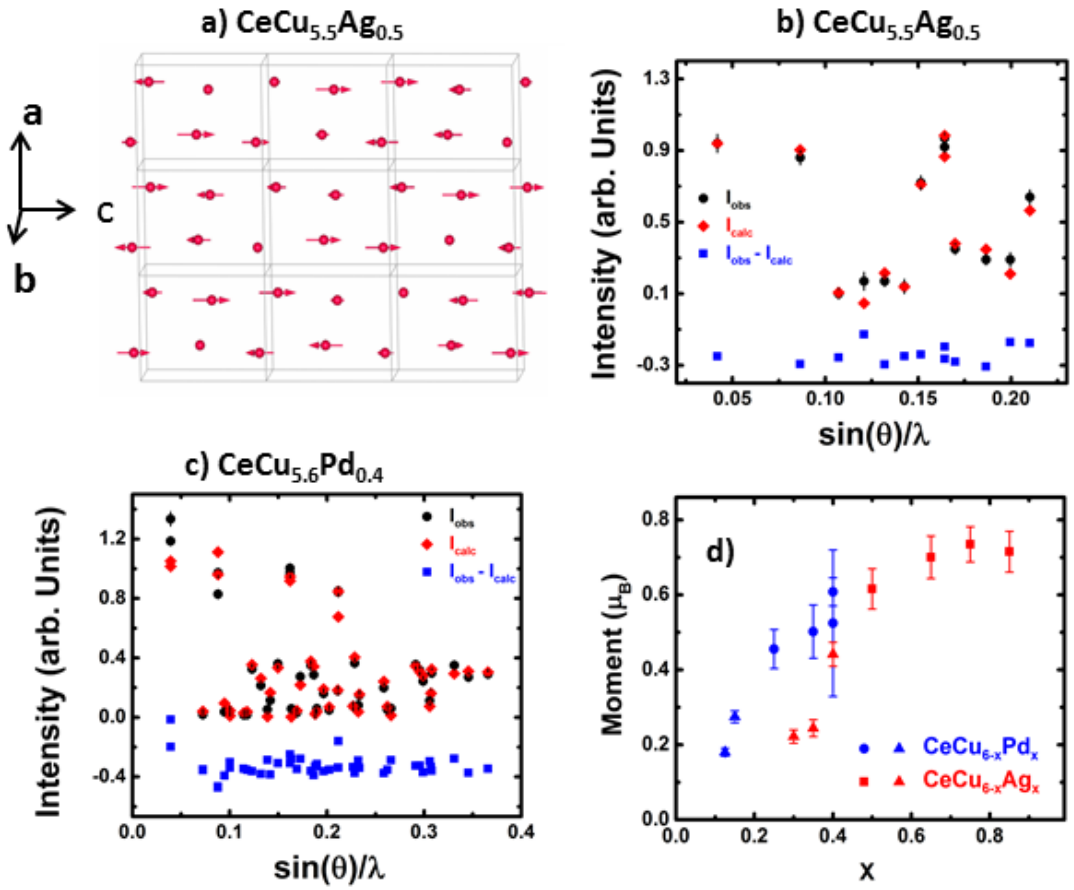



Figure 4.9: a) The magnetic structure of $CeCu_{5.5}Ag_{0.5}$. Each box represents a structural unit cell that contains four Ce-atoms as indicated by the red spheres. The length and direction of the arrows shows the magnitude and direction of the moment, respectively. All Ce-moments point along the $c$-axis of the orthorhombic unit cell. The amplitude of the moment is modulated along the wave vector (0.62 0 0.3). The observed and calculated intensities for the magnetic structure is displayed in b) and c) for $CeCu_{5.5}Ag_{0.5}$ and $CeCu_{5.6}Pd_{0.4}$ respectively. d) Compositional dependence of the ordered moments in $CeCu_{6-x}T_x$ ($T$ = Ag, Pd). The magnetic structure determined for $CeCu_{5.5}Ag_{0.5}$ and $CeCu_{5.6}Pd_{0.4}$, was assumed to be the same for the remaining members of each series. The QCP occurs at $x = 0.05$ for $CeCu_{6-x}Pd_x$ and $x = 0.2$, for $CeCu_{6-x}Ag_x$. A point shown as a triangle indicates a composition for which the magnetic moment was not completely saturated and thus the full moment value will be somewhat larger.

After the correction for instrumental resolution, magnetic peaks were normalized to the intensity of the nearby structural peak (0 0 2). The resulting order parameter data is used to characterize the magnetic phase transition. The Neel temperatures ($T_N$) are estimated by fitting the power law equation, $y = y_0 + A(T - T_N)^{2\beta}$. At temperatures close to $T_N$, some rounding of the order parameter is observed. The two most likely reasons for this are the presence of critical scattering or a small compositional variation leading to a distribution of $T_N$s. If the rounding is entirely attributed to compositional variation, this indicates a spread of $\Delta T_N \leq 20\%$, which, with reference to the phase diagram (Fig. 4.5), would imply a compositional variation of $\Delta x \leq 0.02$. On the other hand, a departure from the behavior of a QCP and the associated expectation of mean field behavior ($\beta = 0.5$) may be the result of the recovery of classical critical behavior and the presence of critical scattering at temperatures close to $T_N$. With the currently available data, these two possibilities could not be unambiguously distinguished. Therefore, the value of $\beta$ was restricted to the mean field value of 0.5. Mean field behavior has previously been observed near the QCP in other heavy fermion systems[52, 54, 59, 113]. This is likely due to the change in the effective dimension of the system as the quantum dynamics influences the static critical properties–one of the most prominent distinctions from a counterpart classical phase transition. The fits of the order parameter, for several compositions of $CeCu_{6-x}Ag_x$ and $CeCu_{6-x}Pd_x$, agree well with the mean-field approximation, as shown in figure 4.8.

To check the consistency with prior work utilizing magnetic susceptibility and heat capacity to determine $T_N$ [13, 14, 95], a heat capacity measurement was performed for $CeCu_{5.5}Ag_{0.5}$. This gives $T_N = 0.51(1)$, which is identical to the value extracted from fitting the order parameter ($T_N = 0.50(2)$) as well as previously published heat capacity measurements [14, 95]. For all other compositions, the estimated values of $T_N$ from the fit of the order parameter are in good agreement with the magnetic susceptibility and heat capacity measurements of previous

studies[13, 14, 95]. The estimated values of $T_N$ in $CeCu_{6-x}Ag_x$ and $CeCu_{6-x}Pd_x$ are incorporated in the phase diagrams presented in Fig. 4.5.

For the wave vector $\mathbf{k_1}$ = (0.62 0 0.3) and space group $Pnma$, representational analysis indicates the four equivalent Ce positions in the unit cell split into separate orbits as given by 1: (0.2586, 0.25, 0.5636), 2: (0.2414, 0.75, 0.06360), 3: (0.7414, 0.75, 0.4364), 4: (0.7586, 0.25, 0.9364). Two irreducible representations (IRs) are found for all four orbits with their basis vectors as listed in Table 4.5. To understand the magnetic structure in greater detail, the compositions $CeCu_{5.5}Ag_{0.5}$ ($T_N$ = 0.51(1) K) and $CeCu_{5.6}Pd_{0.4}$ ($T_N$ = 1.20(1) K) were taken. Following the representational analysis, the first IR, $\Gamma_1$, restricts the arrangement of Ce-moments to be parallel to the $b$-axis. Given that the propagation vector indicates a modulation in the $ac$-plane, only a transverse modulation of the magnetic moment is possible under this representation. Structures of this type can discarded as the observed intensities do not match with the calculated intensities. The second IR, $\Gamma_2$, restricts moments to the $ac$-plane but limits the possible magnetic structures to those with a modulation of the magnetic moment amplitude or a cycloidal modulation of the moment direction. However, the cycloidal model does not account well for the intensities of the observed magnetic reflections. The remaining possibility is a sinusoidal modulation of the moment amplitude in the crystallographic $ac$-plane. To simplify the problem, the directions of the Ce-moments were constrained to be same for all four Ce-orbits but the phases were allowed to vary. The best fit under this assumption was obtained when the moments point along the $c$-axis with a magnitude of 0.61(1) $\mu_B$. This yields the magnetic structure shown in the Figure 4.9(a), which is also consistent with the previous studies on $CeCu_{6-x}Au_x$ that report a similar structure based on neutron diffraction measurements[6, 9, 54, 57, 114]. The comparison between the observed and the calculated intensities is shown in the Figure 4.9(b).

In contrast to $CeCu_{5.5}Ag_{0.5}$, the low temperature crystal structure of $CeCu_{5.6}Pd_{0.4}$ is monoclinic with space group $P2_1/c$. The representational analysis of $CeCu_{5.6}Pd_{0.4}$ using the monoclinic space group along with the corresponding propagation vector

$\mathbf{Q}_{\mathbf{monoclinic}}$ = (0 0.23 0.58) indicates that each orbit constitutes a single representation with three real basis vectors along $a_m$, $b_m$ and $c_m$ axes of the monoclinic structure. The fit of the magnetic structure assuming a sinusoidal modulation of the moment indicates that the moments are pointed along the $b_m-$ axis of the monoclinic structure ($c-$axis of the orthorhombic structure*), identical to the magnetic structure of $CeCu_{5.5}Ag_{0.5}$ described above. The fit of the observed intensity is shown in the figure 4.9c.

The ordered moment obtained from a neutron diffraction measurement is proportional to the square root of the intensity of the magnetic Bragg peak, which is generally scaled to the nuclear reflections to provide an absolute value. Assuming that the magnetic structure doesn't vary with the doping composition, the moments of other compositions were determined from a comparison of the normalized magnetic intensity with respect to $CeCu_{5.5}Ag_{0.5}$ and $CeCu_{5.6}Pd_{0.4}$. For the compositions near the QCP, a full saturation of the ordered moments was not observed and the real value of the ordered moment is somewhat larger than the estimated values. The variation of the magnetic moment with Ag/Pd-composition is shown in the figure 4.9(c).

## 4.4 Discussion

It is interesting to view the results presented here on $CeCu_{6-x}Pd_x$ and $CeCu_{6-x}Ag_x$ in the context of the structural and magnetic properties of the intensively studied $CeCu_{6-x}Au_x$ system. INS measurements at the QCP of $CeCu_{6-x}Au_x$ show the presence of critical spin fluctuations peaked at $\mathbf{Q}$ = (0.8 0 0), but present in an extended region of the Brillouin zone in the shape of a butterfly[9, 24]. Interestingly, the points at the wings of the butterfly correspond to the magnetic ordering wave vectors observed for different Au-compositions of $CeCu_{6-x}Au_x$ in the magnetically

*Note that the structural parameters undergo a cyclic change at the orthorhombic-monoclinic phase transition

ordered regime[52, 53, 54, 55, 56]. Among all the compositions of $CeCu_{6-x}Au_x$ that are reported, the composition $x$ = 0.2, studied by neutron diffraction closest to the QCP, is the only one which exhibits short ranged magnetic ordering near the wave vector $\mathbf{Q}$ = (0.8 0 0) in addition to a long range magnetic ordering that occurs at $\mathbf{Q}$ = (0.625 0 0.275)[6, 8, 52, 57]. With a slight increase in Au-composition, for $x$ = 0.3, the short range order disappears and only the long range magnetic ordering is observed at the wave vector $\mathbf{Q}$ = (0.64 0 0.275)[6, 8, 52]. Upon further alloying with Au, at $x$ = 0.5, the magnetic wave vector exhibits a crossover to $\mathbf{Q}$ = (0.59 0 0), which stays roughly the same for higher Au-composition [6, 8, 52, 58]. However, in $CeCu_{6-x}Ag_x$ and $CeCu_{6-x}Pd_x$, our studies find no evidence for short range magnetic order near $\mathbf{Q}$ = (0.8 0 0). Furthermore, in $CeCu_{6-x}Ag_x$, the magnetic propagation vector is essentially unchanged for the range of the compositions investigated here suggesting there is no crossover to a propagation vector near $\mathbf{Q}$ = (0.59 0 0) at large $x$.

The possibility that the structural degrees of freedom could give rise to a quantum multicritical point in $CeCu_{6-x}Au_x$[5] is interesting and worthy of further consideration. In the related system, $CeCu_{6-x}Ag_x$, the magnetic QCP occurs in the orthorhombic phase, and is well-separated from the termination of the structural phase transition. In $CeCu_{6-x}Pd_x$, the magnetic QCP occurs in monoclinic phase, and no structural critical point is observed for $x \leq 0.4$. Despite the distinct behavior of the structural properties of these systems, the magnetic behavior of all three systems is in many ways similar. In particular, the magnetic structures of all these systems are identical to each other: The Ce-moments point along the $c-$axis of the orthorhombic unit cell and are modulated with an incommensurate wave-vector. The heat capacity in all three systems appears to exhibit a similar logarithmic divergence at low temperatures [13, 14, 115], indicating the thermal average of the underlining critical fluctuations is independent of the structural properties. These observations suggest that the magnetic QCP is independent of the structural phase transition.

The orthorhombic-monoclinic structural phase transition in $CeCu_6$ is second order in nature[93]. There is no evidence either in the temperature dependence of the monoclinic order parameter $(a_m c_m \cos\beta)^2$ or in the square of the resonance frequencies determined from the RUS measurements that the transition becomes first order with doping (See Fig. 4.3(c) and 4.4). Thus there appears to be the possibility that a complete suppression of the orthorhombic-monoclinic transition results in a SQCP. The notion of the SQCP is still emerging and has attracted recent attention. For example, the $(Sr,Ca)_3Ir_4Sn_{13}$ series appears to exhibit a SQCP[116, 117]. Since any SQCP in $CeCu_{6-x}Au_x$ or $CeCu_{6-x}Ag_x$ would be complicated by the presence of a magnetic QCP, investigating other $CeCu_6$-derived systems or their non-magnetic analogs, such as $LaCu_{6-x}Au_x$ appear ideal systems in which to further probe the concept of a SQCP. Further study to investigate the possibility of SQCP in $LaCu_{6-x}Au_x$ is presented in chapter 5.

## 4.5 Conclusions

In conclusion, a comprehensive study of the structural and the magnetic properties of $CeCu_{6-x}Ag_x$ and $CeCu_{6-x}Pd_x$ is reported. Long range incommensurate magnetic ordering evolves with doping in both systems. The magnetic structure is composed of a sinusoidal modulation of the Ce-moments which are aligned along the $c$-axis of the orthorhombic ($Pnma$) unit cell. The long range magnetic structure as well as the size of the ordered moments determined in $CeCu_{6-x}Ag_x$ and $CeCu_{6-x}Pd_x$ are similar to the well known heavy fermion system $CeCu_{6-x}Au_x$. Yet, these systems exhibit several unique structural and magnetic properties. The magnetic QCP in $CeCu_{6-x}Ag_x$ occurs in the orthorhombic phase and is well separated from the termination of the structural phase transition. No substantial change in the magnetic wave vector is observed with Ag-composition in $CeCu_{6-x}Ag_x$. In $CeCu_{6-x}Pd_x$, the magnetic QCP occurs well within the monoclinic phase. Further

investigations of $CeCu_{6-x}Ag_x$ and $CeCu_{6-x}Pd_x$ are essential to understand the nature of QCP in these systems.

# Chapter 5

# Elastic QCP in $LaCu_{6-x}Au_x$

A similar version of this chapter is published as, "Candidate Elastic Quantum Critical Point in $LaCu_{6-x}Au_x$", L. Poudel, A. F. May, M. R. Koehler, M. A. McGuire, S. Mukhopadhyay, S. Calder, R. E. Baumbach, R. Mukherjee, D. Sapkota, C. de la Cruz, D. J. Singh, D. Mandrus, and A. D. Christianson, Phys. Rev. Lett. **117**, 235701(2016) (Reference [118])

In this chapter, the structural properties of $LaCu_{6-x}Au_x$ are presented. Neutron diffraction, x-ray diffraction, and heat capacity measurements were performed to study the evolution of structural properties with Au-composition. The continuous orthorhombic-monoclinic structural phase transition in $LaCu_6$ is suppressed linearly with Au substitution. A complete suppression of the structural phase transition occurs at the critical composition, $x_c$ = 0.3. Heat capacity measurements at low temperatures indicate residual structural instability at $x_c$. The instability is ferroelastic in nature, with density functional theory (DFT) calculations showing negligible coupling to electronic states near the Fermi level. The data and calculations presented here are consistent with the zero temperature termination of a continuous structural phase transition suggesting that the $LaCu_{6-x}Au_x$ series hosts an elastic quantum critical point.

## 5.1 Introduction

Quantum fluctuations in the vicinity of a QCP generate a seemingly inexhaustible supply of new phases of matter[1, 28, 29, 105, 119, 120, 121, 122, 123]. Although of great interest, the competing phases typically found near a QCP obscure the fundamental critical behavior and consequently a general understanding of such phase transitions has remained elusive and no concept as powerful as the universality of classical continuous phase transitions has emerged. Hence, new examples of QCPs are highly prized as a means of probing the general organizing principles of QCPs. Thus it is rather surprising, given the immense body of work devoted to the study of structural phase transitions, that little attention has been given to the concept of a SQCP. The bulk of previous work on QCPs involving structural degrees of freedom has been focused on an incipient ferroelectric state[124, 125, 126, 127, 128, 129, 130]. For example, the quantum zero point motion in $SrTiO_3$ acts to prevent the complete softening of the relevant optic phonon mode resulting in a quantum paraelectric on the verge of ferroelectricity[131, 132].

Recently, interest in SQCPs has risen. For instance, $ScF_3$ has been discussed as an example of an SQCP in an ionic insulator[133]. On the other hand, in metallic systems, there have been several studies of a family of Rameika phase stannides where a structural phase transition with concomitant changes in the Fermi surface can be tuned to an SQCP[116, 117, 134, 135, 136, 137, 138]. Here, the problem of an SQCP is approached from the perspective of a structural phase transition where elastic instabilities are primarily responsible for the lowering of symmetry and electronic degrees of freedom are unimportant. This type of transition is similar to the nematic transition as found in the Fe-based superconductors[139, 140, 141] where the point group symmetry is lowered without a change in translational symmetry. The two cases are nevertheless distinct, as the nematic transition in Fe-based superconductors is strongly coupled to electronic degrees of freedom, whereas the elastic transition studied here is in the opposite decoupled limit.

Elastic QCPs, where the quantum zero point motion of the atoms destroys an elastically ordered state, have been the subject of recent theoretical study[142]. However, examples where electronic degrees of freedom are uninvolved have eluded study thus far. To remedy this, we have identified the $LaCu_{6-x}Au_x$ series as a promising candidate to host an elastic QCP. $LaCu_6$ exhibits a continuous phase transition from an orthorhombic ($Pnma$) to a monoclinic ($P2_1/c$) crystal structure at 460 K[43]. A phase transition of this type is a common feature of the $RCu_6$ ($R$ = La, Ce, Pr, Nd, Sm) family including the $CeCu_{6-x}Au_x$ series which hosts one of the most studied antiferromagnetic QCPs[1, 7, 24, 25, 42, 43, 61, 62, 63]. The continuous nature of the orthorhombic-monoclinic phase transition is evidenced by: a smooth evolution of the monoclinic distortion[61, 62]; a gradual softening of the $C_{66}$ elastic constant[42]; a progressive softening of a transverse acoustic phonon mode[43]; and a continuous change in the linear thermal expansion coefficient[7]. Furthermore, no signature of the structural phase transition is visible in resistivity measurements[143], suggesting that the electronic degrees of freedom are of little consequence. Finally, the absence of $f-$electrons in $LaCu_6$ eliminates complications due to a magnetic ground state.

In this chapter, a detailed study of the structural properties of the $LaCu_{6-x}Au_x$ series as a function of Au-composition will be presented. The structural transition temperature ($T_S$) in $LaCu_{6-x}Au_x$ decreases linearly with Au-doping, and extrapolation of $T_S$ indicates complete suppression of the transition at the critical composition $x_c$ = 0.3. The low temperature heat capacity is maximum at $x_c$ as is typical for a QCP. DFT calculations show that the Fermi surface is essentially unchanged at $T_S$ and that the structural transition occurs as the result of a zone center elastic instability. The measurements taken together with the calculations point towards an elastic QCP in the $LaCu_{6-x}Au_x$ series.

## 5.2 Experimental Details

Polycrystalline samples of $LaCu_{6-x}Au_x$ were prepared by arc melting stoichiometric compositions of La (purity ≥ 99.998%, Ames laboratory), Cu (purity 99.9999%, Alpha Aesar) and Au (purity 99.9999 %, Alpha Aesar) as described in the section 3.1.1. Specific heat measurements were performed on selected compositions. Structural properties for each composition were obtained from Rietveld analysis of neutron and/or x-ray diffraction patterns. The phase purity of polycrystalline $LaCu_{6-x}Au_x$ samples was checked by laboratory x-ray diffraction measurements at room temperature. The diffraction patterns in $LaCu_{6-x}Au_x$ corresponded to either the orthorhombic ($Pnma$) or the monoclinic ($P2_1/c$) phase depending on composition. For $x$ = 0.15, 0.2, 0.25, additional x-ray diffraction measurements were performed on a PANalytical X'Pert Pro MPD powder x-ray diffractometer using Cu$K_{\alpha,1}$ radiation ($\lambda$ = 1.5406 Å). Full diffraction patterns were collected at room temperature and 20 K, followed by scans around few selected Bragg peaks in 10 K steps to determine the structural transition temperature, $T_S$.

Neutron diffraction measurements were carried out on polycrystalline samples ($LaCu_{6-x}Au_x$, $x$ = 0.125, 0.265, 0.275, 0.3) with the HB-2A powder diffractometer at the HFIR of ORNL. Neutrons of wavelength 1.54 Å were used with collimations of $12' - 21' - 6'$ before the monochromator, sample and detector, respectively. Samples of mass ≈ 5 g were finely powdered inside a glove box and held in a vanadium can with helium exchange gas to facilitate thermal conduction. The can was loaded in a closed cycle refrigerator system. Diffraction measurements were carried out at different temperatures near and below $T_S$. To examine the impact of Au-doping in greater detail, high resolution synchrotron x-ray measurements were performed on two compositions: $LaCu_6$ (monoclinic) and $LaCu_{5.7}Au_{0.3}$ (orthorhombic). The measurements were carried out at beamline 11-BM of the APS at ANL using synchrotron x-rays of wavelength $\lambda$ = 0.413 Å. The samples were mixed with $SiO_2$

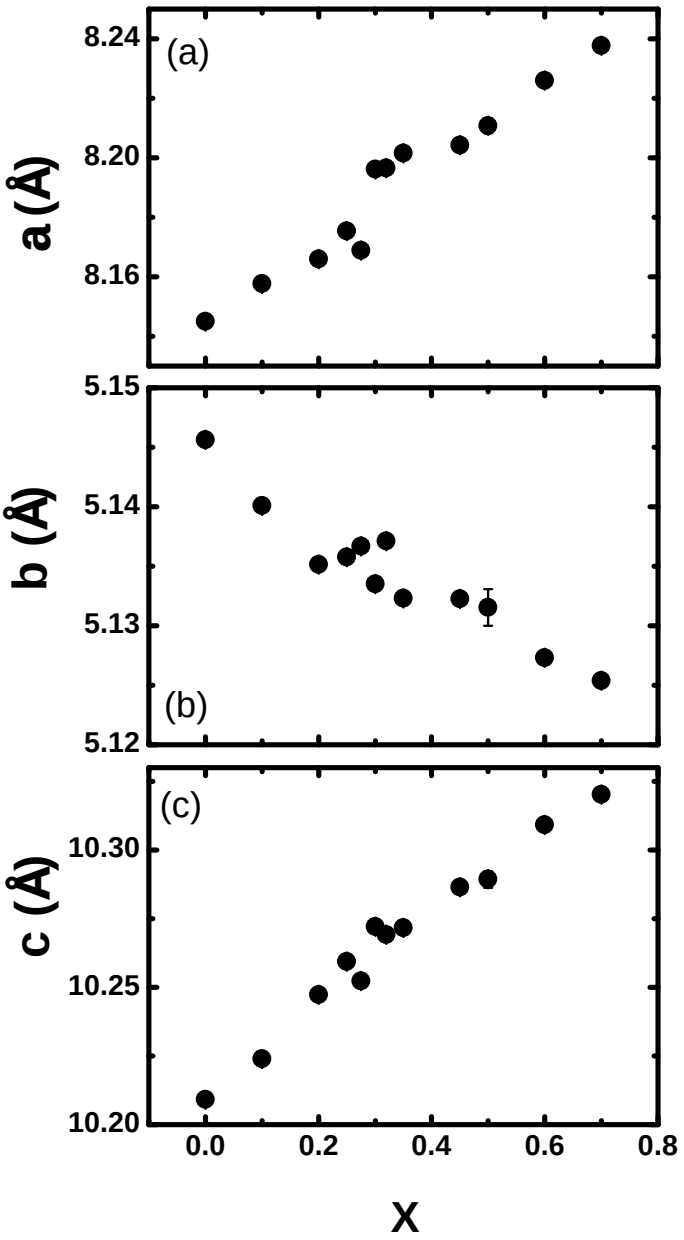



Figure 5.1: Orthorhombic lattice parameters (a) $a$, (b) $b$, (c) $c$ in $LaCu_{6-x}Au_x$ at room temperature. The lattice parameters were obtained from the Rietveld refinements of laboratory x-ray diffraction measurements. The compositions $x = 0$ and 0.1 were refined in monoclinic structure (space group: $P2_1/c$). All other compositions ($x \geq 0.2$) were refined to the orthorhombic phase (space group: $Pnma$).

powder in a molar ratio of 1:2 (for $LaCu_6$) and 1:3 (for $LaCu_{5.7}Au_{0.3}$) to minimize x-ray absorption. The finely ground mixtures were held in kapton tubes of diameter 0.8 mm for the measurements. The structural parameters were extracted from Rietveld analyses of the diffraction patterns using the FullProf software suite[99].

My collaborators performed DFT calculations using the Perdew, Burke and Enzerhof (PBE) generalized gradient approximation[103] for $LaCu_6$ with experimental structures. Phonon calculations were performed with the Phonopy code[144] based on underlying DFT calculations by the VASP code[145, 146]. Electronic structure calculations were performed with the general potential LAPW method[146] as implemented in WIEN2k[102, 147]. The calculations were done using well converged basis sets. LAPW plus local orbital basis sets were used with LAPW sphere radii of 2.3 $bohr$ for La and 2.25 $bohr$ for Cu. The electronic structure calculations were performed using experimental lattice parameters for the orthorhombic and monoclinic cells with fully relaxed internal atomic coordinates.

My collaborators performed heat capacity measurements of $LaCu_{6-x}Au_x$($x$= 0, 0.1, 0.2, 0.25, 0.27, 0.3, 0.32, 0.35, 0.4, 0.5, 0.6, 0.7) above 2 K in a Quantum Design PPMS system.

## 5.3 Results

### 5.3.1 Neutron/x-ray diffraction

Figure 5.1 displays the compositional variation of the orthorhombic lattice parameters in $LaCu_{6-x}Au_x$ at room temperature. The substitution results in an overall expansion of the unit cell due to the larger atomic radius of Au (covalent radius = 144 fm) compared to Cu (covalent radius = 128 fm), which is typical for the $RCu_6$ family[7]. With an increase in Au-composition for ($x \leq 0.7$), the $b$-parameter decreases while $a$ and $c$-parameter show a linear increase with $x$. The temperature dependence of the lattice parameters in $LaCu_{6-x}Au_x$ (for $x$ = 0, 0.125, 0.265, 0.275)

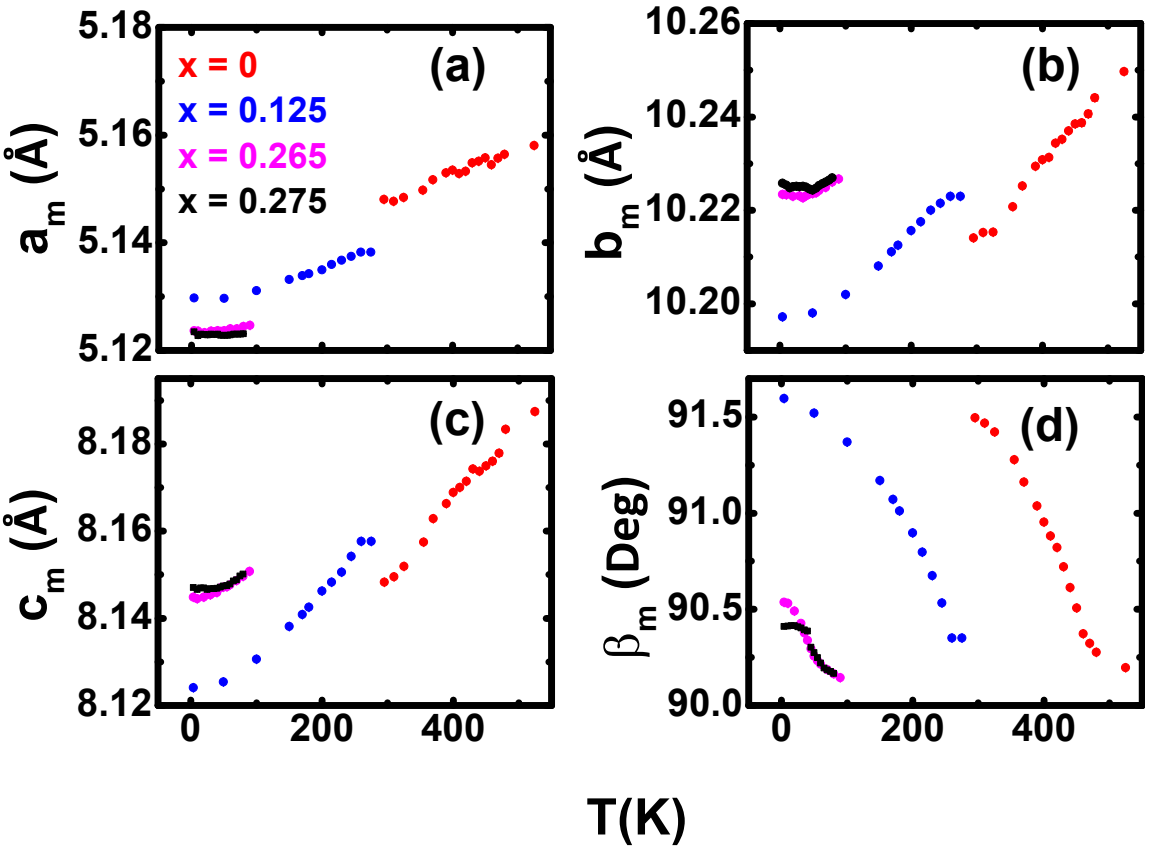



Figure 5.2: Temperature dependence of the monoclinic lattice parameters (a) $a_m$, (b) $b_m$, (c) $c_m$, and (d) $\beta_m$ in $LaCu_{6-x}Au_x$.

is shown in Fig. 5.2. For each composition studied, the lattice parameters increase smoothly with temperature and no discontinuities were observed at $T_S$, which is consistent with the continuous nature of the phase transition.

The structural phase transition in $LaCu_6$ was tuned by substituting Cu by isoelectronic Au. At the structure transition, the lattice parameters transform from orthorhombic to monoclinic symmetry as follows: $a \rightarrow c_m$, $b \rightarrow a_m$, $c \rightarrow b_m$, and $\beta_m$ denotes the monoclinic angle. In a diffraction measurement, the structural phase transition is manifested by the splitting of some of the Bragg peaks[*]. The temperature at which the peaks begin to separate is characterized as the transition temperature ($T_S$), as illustrated in Fig. 5.3(a). The shear strain acts as an order parameter for the phase transition. Using the geometry of the Fig. 5.4, the shear component of strain tensor can be written as[148],

$$e^m_{13} = e^m_{31} = \frac{1}{2} e^m_s = \frac{1}{2}\frac{\Delta a}{c_0} \tag{5.3}$$

or equivalently,

$$e^m_{13} = \frac{1}{2}\frac{c_m}{c_0}\cos(\beta_m) \tag{5.4}$$

where, $c_0$ is the extrapolation of lattice parameter from the orthorhombic phase into the monoclinic phase. Above $T_S$, the shear strain is zero[†]. Hence, to determine

[*]The $d-$spacing corresponding to a reflection in orthorhombic and monoclinic geometry is defined as,

$$\frac{1}{d^2_{orthorhombic}} = \left(\frac{h^2}{a^2} + \frac{k^2}{b^2} + \frac{l^2}{c^2}\right) \tag{5.1}$$

$$\frac{1}{d^2_{monoclinic}} = \frac{1}{\sin^2\beta_m}\left(\frac{h^2}{a^2_m} + \frac{k^2}{b^2_m} + \frac{l^2}{c^2_m} - \frac{2hl\cos\beta_m}{a_m c_m}\right) \tag{5.2}$$

In the orthorhombic structure, the $d-$spacing of each member of a Bijvoet pairs is equal. However, in the monoclinic structure, for $h \neq 0$ and $l \neq 0$, the $d-$spacing for two Bijvoet pairs can be different. Consequently, in a powder diffraction measurement, a structural Bragg peak that can be indexed by $(hkl)$ in the orthorhombic system separates into a pair of peaks which correspond to $(kl\text{-}h)$ and $(\text{-}klh)$ in the monoclinic phase.

[†]In the orthorhombic notation, $e^m_{13}$ translates into $e_{21}$. Also, the component of stress tensor $\sigma_{21}$ is related to $e_{21}$ by,

$$\sigma_{21} = c_{2121} e_{21} \tag{5.5}$$

where, $c_{2121}$ is the elastic shear modulus, which is usually written in a contracted notation $c_{66}$.

$T_S$ for each composition, the values of $\cos^2\beta_m$ extracted from the analysis of the diffraction data were extrapolated as a function of temperature (Fig. 5.3(b)). The resulting transition temperatures in $LaCu_{6-x}Au_x$ are summarized in the phase diagram shown in Fig. 5.5. A linear decrease in $T_S$ with Au-composition is observed. Extrapolation of $T_S$ as a function of Au-composition shows that the phase transition disappears at $x_c = 0.30(3)$ [‡]. Further support for this value of $x_c$ and the presence of a QCP is provided by the extrapolation of $\cos^2\beta_m$ at 20 K for each composition, which yields $x_c = 0.28$(Fig. 5.6) close to the value $x_c = 0.3$ determined from directly extrapolating $T_S$.

Figure 5.7 displays room temperature synchrotron x-ray diffraction patterns with the fits obtained from Rietveld refinements. In agreement with the compositional dependence displayed in the phase diagram (Figs. 5.5 and 5.6), high resolution synchrotron diffraction measurements at room temperature confirm that the crystal structures of $LaCu_6$ and $LaCu_{5.7}Au_{0.3}$ are monoclinic ($P2_1/c$) and orthorhombic ($Pnma$), respectively. No impurity peaks were observed in synchrotron x-ray diffraction measurements, consistent with phase pure samples. The structural and goodness of fit parameters determined from the Rietveld analysis are presented in Table 5.1.

The orthorhombic crystal structure of $LaCu_6$ is similar to the structure of $CeCu_6$ shown in the Fig. 2.3. In the orthorhombic ($Pnma$) structure, the La occupies a $4c$ site, whereas the Cu atoms are distributed among one $8d$ and four $4c$ sites. The Au atoms in $LaCu_{5.7}Au_{0.3}$ occupy only a particular $4c$ site: Cu2 (0.146, 0.25, 0.139). The same site preference was also observed in the related materials $CeCu_{6-x}Au_x$[60] and $CeCu_{6-x}Ag_x$[86] and is attributed to the large volume of the Cu2 site[7]. At the structural transition, the symmetry of all $4c$ sites remains unchanged, whereas the orthorhombic $8d$ site separates into two monoclinic $4c$ sites due to the loss of the mirror symmetry along the (100) plane.

[‡]Note that the statistical error bar on this extrapolation is very small, *i.e.*, 0.004. A more realistic upper bound for the error on $x_c$ is given by the interval between the final two compositions which is 0.025.

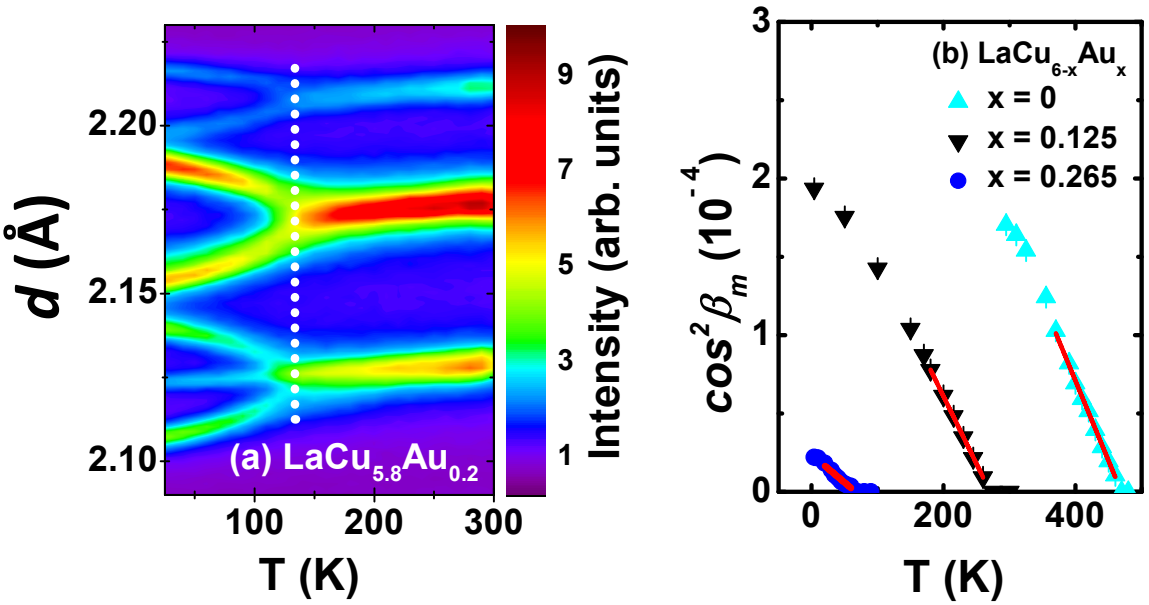



Figure 5.3: (a) X-ray diffraction data showing the splitting of selected Bragg peaks at the structural transition in $LaCu_{5.8}Au_{0.2}$. The following indexing scheme describes the splitting of the peaks: (122)→(22±1), (220)→(20±2), (221)→(21±2). The peak between (21±2) at low temperature is the orthorhombic (303) reflection, which becomes the monoclinic (033) reflection (no splitting). The vertical dotted line indicates the temperature where the peaks begin to separate. Note: Each pixel represents a triangulation-based linear interpolation of the measurement performed with 10 K steps in temperature. (b) The temperature dependence of $\cos^2\beta_m$ in $LaCu_{6-x}Au_x$ determined from neutron diffraction data. $\cos^2\beta_m$ varies smoothly with temperature near $T_S$. For each composition, $T_S$ was estimated from a linear extrapolation (red line) of $\cos^2\beta_m$.

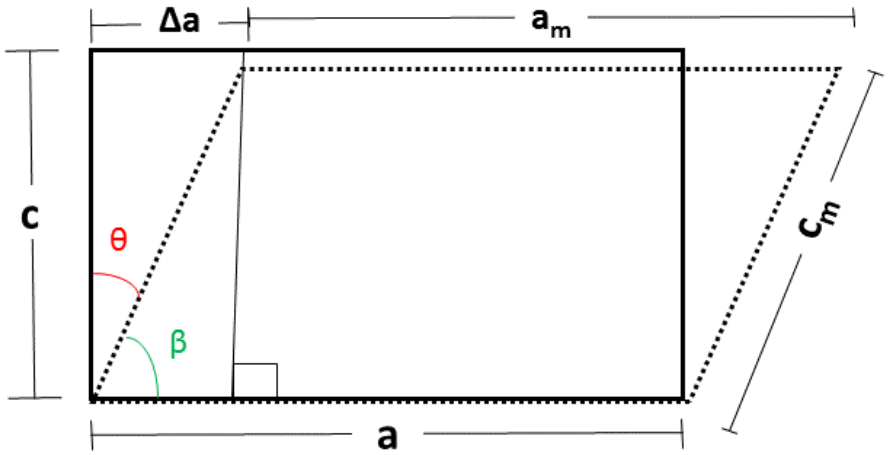



Figure 5.4: The monoclinic $ac$ plane (dotted parallelogram) showing the geometry of a shear. The solid rectangle is the extrapolation of monoclinic $ac$ plane when $\theta = 0$ (no shear).

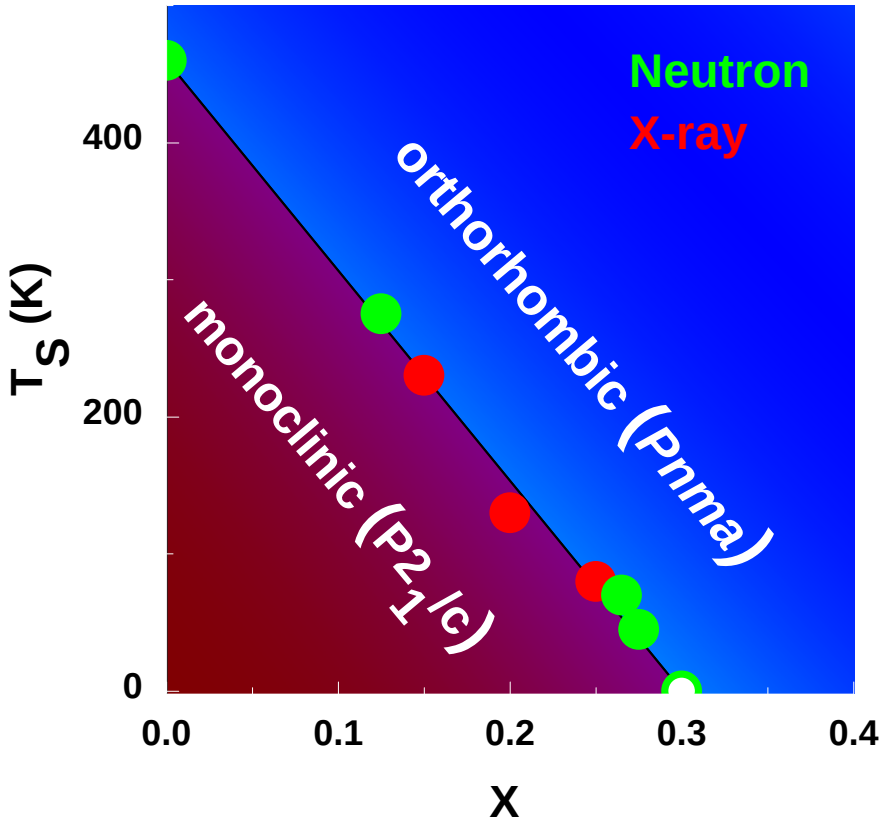



Figure 5.5: Structural phase diagram of $LaCu_{6-x}Au_x$. The open circle represents the point where no structural phase transition is observed above 2 K. The statistical error bars for $T_S$ are smaller than the symbol size. Linear extrapolation of $T_S$ with temperature indicates $x_c = 0.3$.

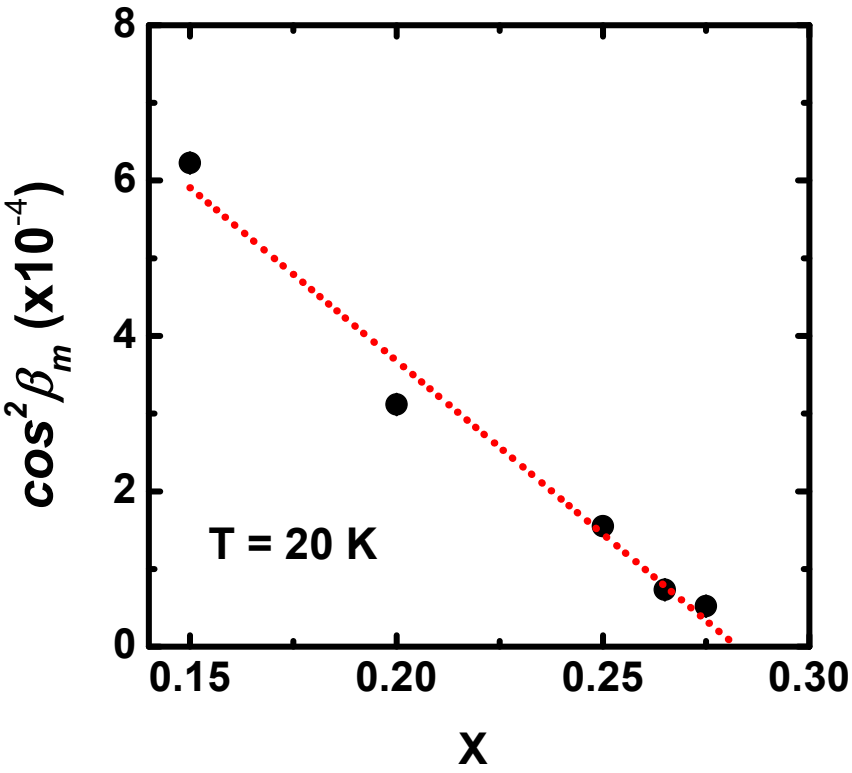



Figure 5.6: The variation of $\cos^2\beta_m$ in $LaCu_{6-x}Au_x$ with Au-composition at 20 K. An extrapolation (dotted red line) of $\cos^2\beta_m$ with Au-composition indicates that the suppression of the monoclinic ground state occurs at $x = 0.28$.

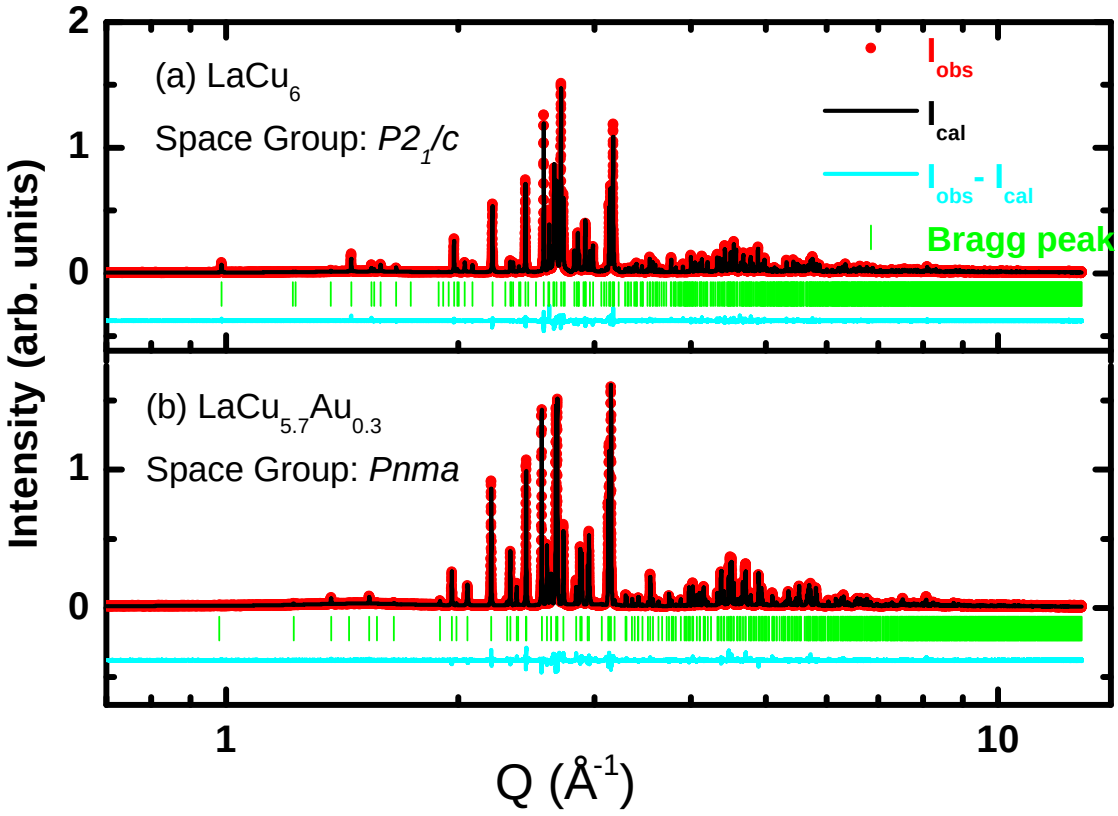



Figure 5.7: Synchrotron x-ray diffraction pattern of (a) $LaCu_6$, (b) $LaCu_{5.7}Au_{0.3}$ at 300 K. The fit (black) to the diffraction pattern (red) is obtained with the Rietveld analysis. The vertical green bars represent structural Bragg peaks. $I_{calc} - I_{obs}$ is offset for clarity. Note: x-axis is in logarithmic scale.

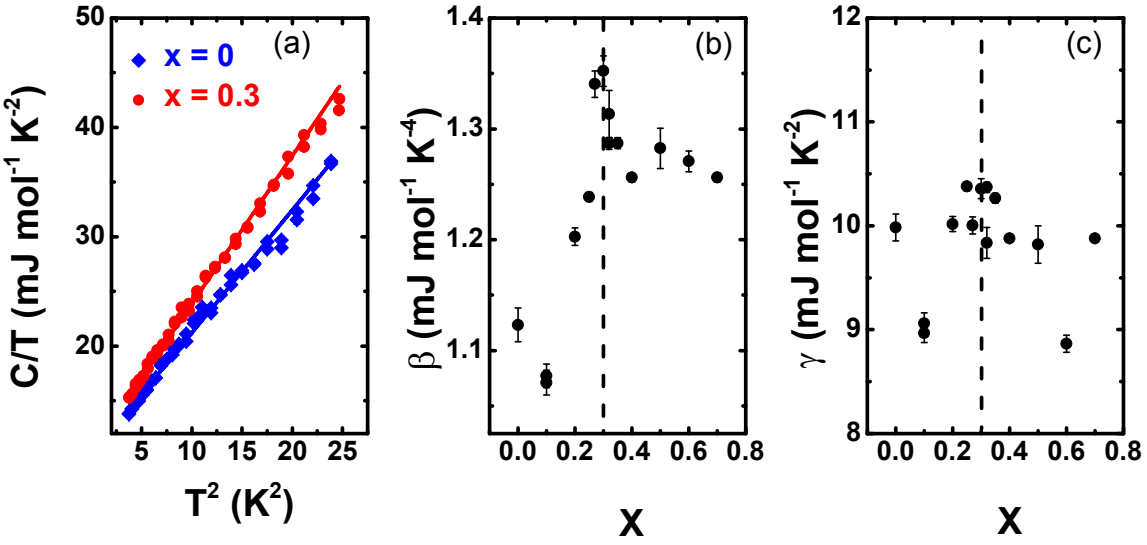



Figure 5.8: (a) Heat capacity data showing $T^3$ behavior at low temperature for $LaCu_6$ ($x = 0$) and $LaCu_{5.7}Au_{0.3}$ ($x_c$=0.3). The solid lines are a fit to the data of the form $C = \gamma T + \beta T^3$. (b,c) The variation of (b) $\beta$ and (c) $\gamma$ obtained from the fits to the heat capacity measurements as a function of Au-composition. The vertical dotted lines indicate the critical composition ($x_c$ = 0.3). In all panels, the values are reported per formula unit.

The Rietveld refinement of $LaCu_{5.7}Au_{0.3}$ was carried out in various steps. In each stage, Au atoms were either placed in one of the five different Cu sites or equally distributed among them. A comparison between calculated and observed intensities at different stages of the refinements indicates that the Au atoms in $LaCu_{5.7}Au_{0.3}$ exclusively occupy the Cu2 site located at ($x/a = 0.146$, $y/b = 0.25$, $z/c = 0.139$). As presented in the Table 5.2, the best set of goodness of fit parameters, $R_p$, $R_{wp}$ and $\chi^2$, are obtained when the Au atoms are constrained to Cu2 site. Furthermore, the refined occupancy of Au on Cu2 site is 0.31(1), which coincides well with the expected value 0.3 (Table 5.1(b)).

### 5.3.2 Heat capacity

For all compositions studied, the low temperature heat capacity can be modelled by the relation, $C = \gamma T + \beta T^3$[149], where $\gamma$ and $\beta$ capture the electronic and phonon contributions to the heat capacity, respectively (Fig. 5.8(a). The phonon heat capacity reaches a maximum value at $x_c$ as shown the Fig. 5.8(b). The electronic heat capacity remains essentially independent of Au-composition (Fig.5.8(c)). The measurement displays no signature of the structural phase transition as shown in the Fig. 5.9.

To check for an enhanced superconducting transition temperature at the critical concentration over the 0.16 K $T_c$ in $LaCu_6$[150], an additional heat capacity measurement of $LaCu_{5.7}Au_{0.3}$ was performed down to lower temperatures using a PPMS with $^3$He insert. No superconducting transition was observed above 0.7 K. The heat capacity data are consistent with the Debye model, as shown in Fig. 5.10.

### 5.3.3 Density Functional Theory Calculations

The phonon dispersions for orthorhombic structure (Fig. 5.11) show a clear instability of ferroelastic character whereas phonon calculations for the monoclinic phase (Fig. 5.12) find only stable modes consistent with the fact that this is the ground state structure. Figure 5.11 shows the unstable transverse acoustic branch

Table 5.1: Room temperature structural parameters of a) $LaCu_6$ and b) $LaCu_{5.7}Au_{0.3}$. The parameters are obtained from the fits to the diffraction patterns shown in Fig. 5.7.

a) **$LaCu_6$**, space group = $P2_1/c$

$a_m$ = 5.145643(2) Å, $b_m$ = 10.20915(4) Å, $c_m$ = 8.14498(3) Å, $\beta_m$ = 91.485(1)

$R_P$ = 13.4, $R_{wp}$ = 15.3, $\chi^2$ = 2.9

| Element | Wyck. | $x/a$ | $y/b$ | $z/c$ | B | Occ. |
|---|---|---|---|---|---|---|
| La1 | 4$c$ | 0.2589(8) | 0.4356(3) | 0.2612(4) | 0.69(4) | 1 |
| Cu1 | 4$c$ | 0.0082(12) | 0.1884(6) | 0.4377(7) | 0.61(12) | 1 |
| Cu2 | 4$c$ | 0.2419(13) | 0.1411(6) | 0.1474(8) | 0.82(12) | 1 |
| Cu3 | 4$c$ | 0.2467(13) | 0.7544(6) | 0.8170(8) | 0.83(12) | 1 |
| Cu4 | 4$c$ | 0.2271(12) | 0.6013(6) | 0.5616(8) | 0.82(12) | 1 |
| Cu5 | 4$c$ | 0.2514(13) | 0.5148(6) | 0.8995(7) | 0.49(11) | 1 |
| Cu6 | 4$c$ | 0.4968(12) | 0.1926(6) | 0.4330(7) | 0.62(11) | 1 |

b) **$LaCu_{5.7}Au_{0.3}$**, space group = $Pnma$

$a$ = 8.19617(6) Å, $b$ = 5.13350(4) Å, $c$ = 10.27211(2) Å

$R_P$ = 13.1, $R_{wp}$ = 14.7, $\chi^2$ = 2.46

| Element | Wyck. | $x/a$ | $y/b$ | $z/c$ | B | Occ. |
|---|---|---|---|---|---|---|
| La1 | 4$c$ | 0.2611(4) | 0.2500 | 0.4360(3) | 1.05(4) | 1 |
| Cu1 | 8$d$ | 0.4361(5) | 0.0029(10) | 0.1897(5) | 1.11(7) | 1 |
| Cu2 | 4$c$ | 0.1462(4) | 0.2500 | 0.1391(3) | 0.87(8) | 0.68(1) |
| Au2 | 4$c$ | 0.1462(4) | 0.2500 | 0.1391(3) | 0.87(8) | 0.32(1) |
| Cu3 | 4$c$ | 0.8180(8) | 0.2500 | 0.7526(5) | 1.04(11) | 1 |
| Cu4 | 4$c$ | 0.5614(9) | 0.2500 | 0.6011(6) | 1.18(11) | 1 |
| Cu5 | 4$c$ | 0.9040(7) | 0.2500 | 0.5162(6) | 1.09(12) | 1 |

Table 5.2: The goodness of fit parameters at different stages of Rietveld refinement of $LaCu_{5.7}Au_{0.3}$. The best set of parameters (shown in bold) was obtained when the Au atoms were constrained to the Cu2 site.

| Au distributed in | $R_p$ | $R_{wp}$ | $\chi^2$ |
|---|---|---|---|
| Cu1-site | 32.7% | 39.6% | 17.95 |
| **Cu2-site** | **13.4%** | **15.3%** | **2.9** |
| Cu3-site | 28.6% | 37.5% | 16.06 |
| Cu4-site | 26.9% | 68.5% | 53.71 |
| Cu5-site | 28.3% | 34.5% | 13.61 |
| Equally distributed | 22.7% | 25.7% | 7.54 |

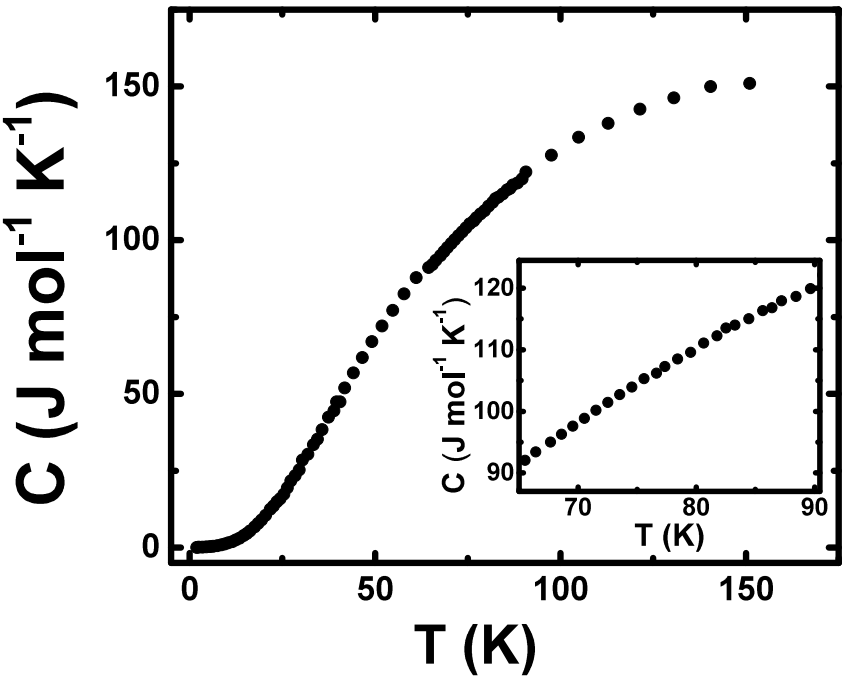



Figure 5.9: Heat capacity measurement of $LaCu_{5.75}Au_{0.25}$. No anomaly is observed near the structural phase transition ($T_S$ = 80(5) K). Inset is a zoom near $T_S$ .

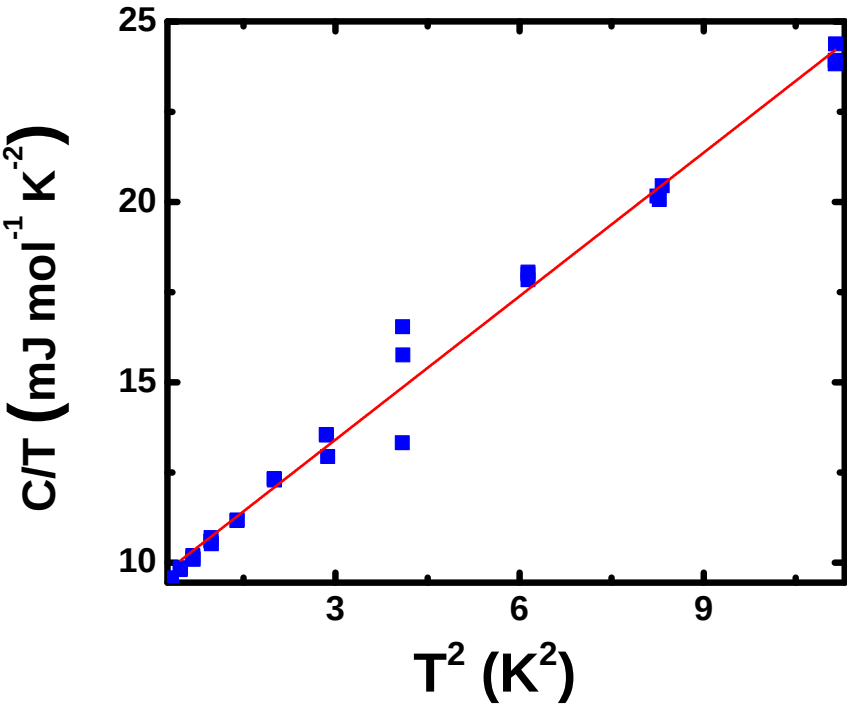



Figure 5.10: Heat capacity measurement of $LaCu_{5.7}Au_{0.3}$ showing Debye-$T^3$ behavior at low temperatures (0.7 K ≥ T ≥ 3.5 K). The straight line (red) is the fit of the equation $C/T = \gamma + \beta T^2$ to the data.

is found along $\Gamma - X$. This branch has an upward curvature, meaning that the instability is a zone center elastic instability. There are no soft optic phonons. The phonon softening calculated by DFT is in line with the softening of the transverse acoustic mode observed in $CeCu_6$ and $LaCu_6$[43]. The transition is continuous and originates from a zone center elastic instability, and may thus be termed ferroelastic, although the switching in the low-T phase has not been observed and therefore formally it is coelastic[151]. Further investigations to confirm ferroelasticity in $LaCu_{6-x}Au_x$ are essential.

The electronic densities of states are very similar for the monoclinic and orthorhombic phases, as shown in Fig. 5.13. In particular there is no significant change around the Fermi level, $E_F$. Also, similar to prior calculations[152], the Cu $d$ bands are occupied and are located from approximately $-5$ eV to $-1.7$ eV with respect to $E_F$. The Cu bands therefore do no play a role in the low energy physics, which instead depends on an electronic structure derived mainly from Cu and La $s$ states. The Fermi surface is derived from five bands that cross $E_F$. As shown in Fig. 5.14, the Fermi surfaces are similar between the two phases. The calculated plasma frequencies for the orthorhombic phase are $\Omega_p$ 3.00 eV, 3.03 eV and 3.61 eV along $a$, $b$ and $c$-axes, respectively. The conductivity anisotropy, assuming isotropic scattering rates, i.e. $\sigma \approx \Omega_p^2$ is predicted to be isotropic in the $a-b$ plane and 45% higher along $c$. These values are similar for the monoclinic phase, i.e. a root mean square average of 3.20 eV with a predicted conductivity having an isotropic plane and a conductivity 40% higher perpendicular to it. The Fermi level DOS is very similar between the two phases: N($E_F$)=3.52 $eV^{-1}$ and 3.37 $eV^{-1}$ per formula unit for the orthorhombic and monoclinic phases, respectively.

Figure 5.13 shows the electronic DOS for orthorhombic and monoclinic phases of $LaCu_6$. The Fermi surfaces of $LaCu_{6-x}Au_x$ are shown in Fig. 5.14. The electronic densities of states are very similar for the monoclinic and orthorhombic phases. In particular, there is no significant change around the Fermi level, $E_F$ . Similar to the prior calculations[152], the Cu $d$-bands are occupied and are located from

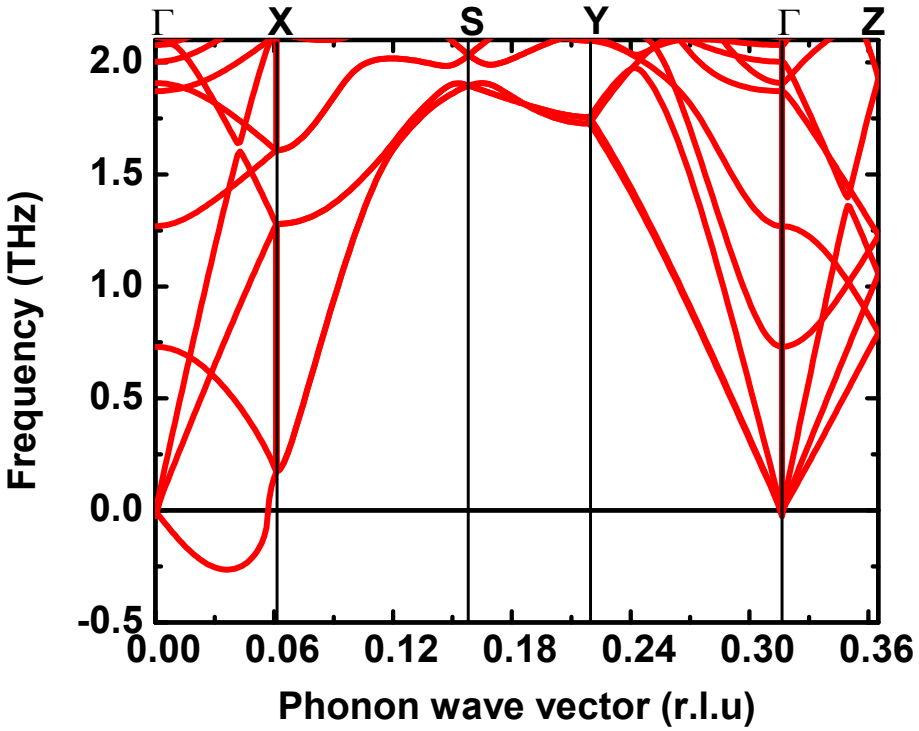



Figure 5.11: Calculated phonon dispersions of $LaCu_6$ with the $Pnma$ crystal structure. The imaginary phonon mode frequency from Γ to $X$ indicates the instability of the orthorhombic structure.

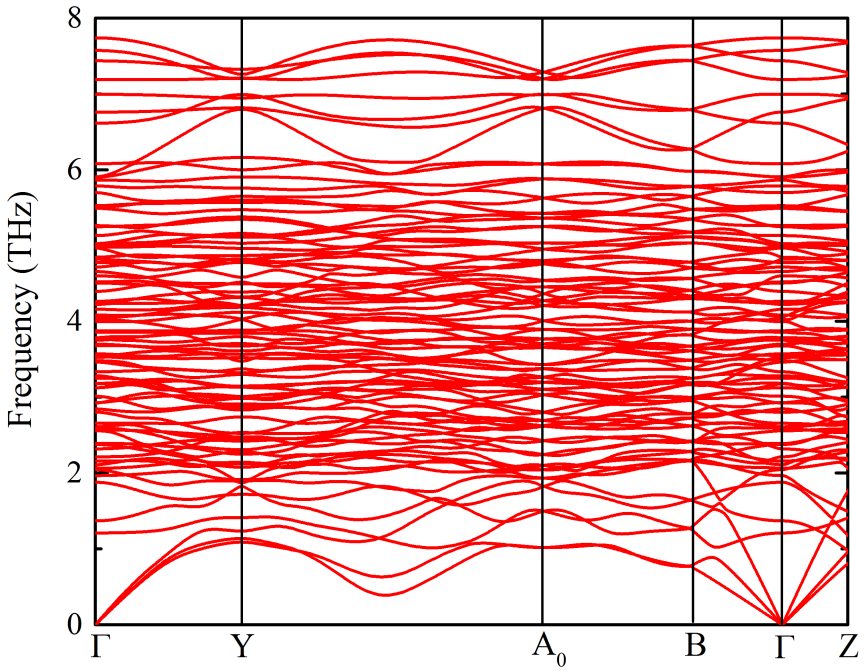



Figure 5.12: Calculated phonon dispersion of $LaCu_6$ with monoclinic (space group: $P2_1/c$) crystal structure. All the phonon modes are stable with monoclinic structure.

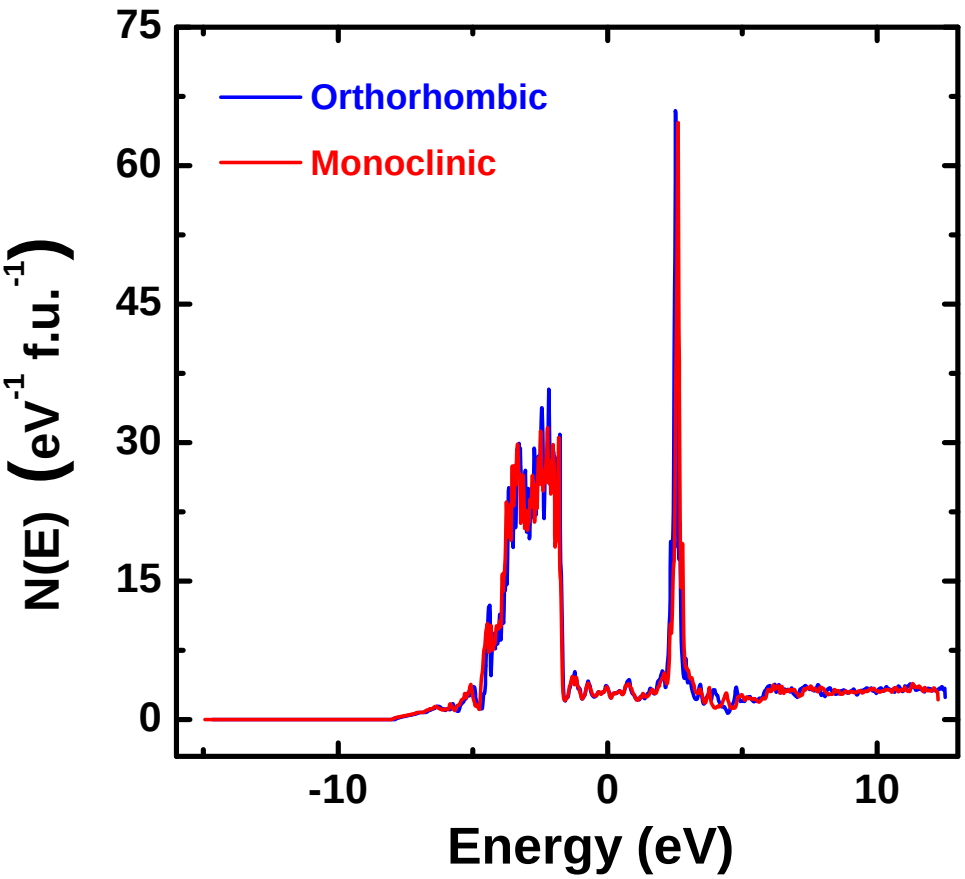



Figure 5.13: Electronic DOS of $LaCu_6$ in orthorhombic and monoclinic phases.

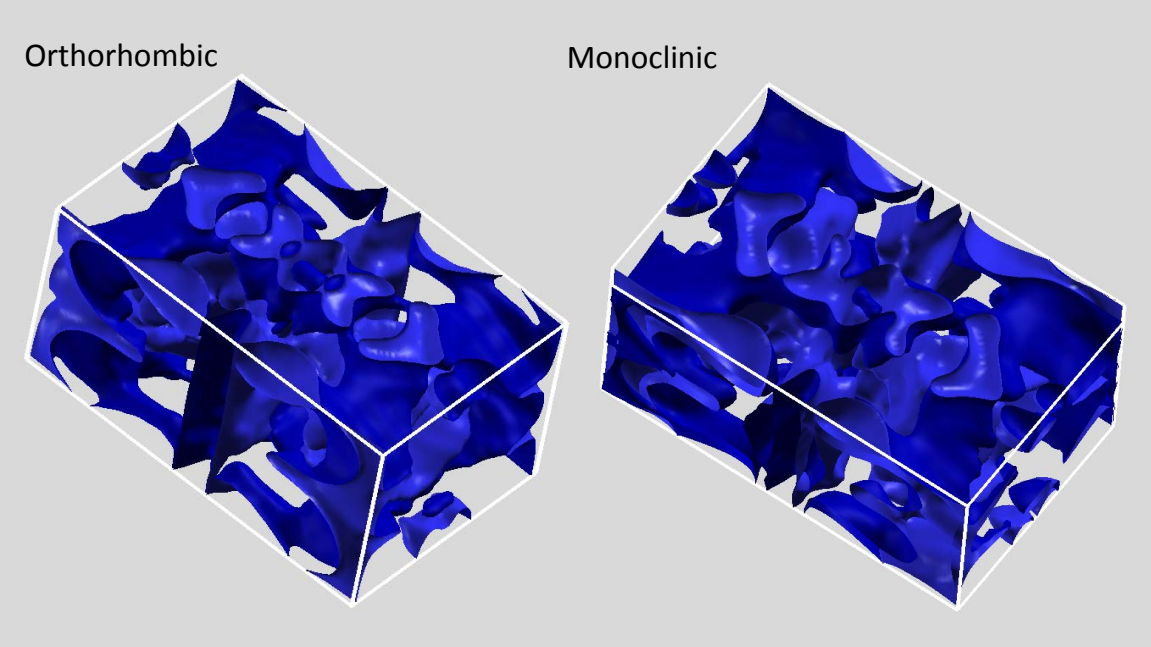



Figure 5.14: Fermi surfaces of $LaCu_6$ in orthorhombic and monoclinic phases.

approximately -5 $eV$ to -1.7 $eV$ with respect to $E_F$ and therefore do not play a role in the low energy physics, which instead depends on an electronic structure derived mainly from Cu and La $s-$states. The Fermi surface is derived from five bands that cross $E_F$ and is similar in both two phases . The calculated plasma frequencies($\Omega_p$) for the orthorhombic phase are 3.00 $eV$, 3.03 $eV$ and 3.61 $eV$ along $a$, $b$ and $c$, respectively. The Fermi level DOS is very similar between the two phases: $N(E_F)$ = 3.52 $eV^{-1}$ and 3.37 $eV^{-1}$ per formula unit for the orthorhombic and monoclinic phases, respectively.

## 5.4 Discussion

Calculated phonon dispersions which show a zone center elastic instability provide additional insights into the nature of the structural phase transition in $LaCu_{6-x}Au_x$. Such zone center symmetry lowering without other apparent long range orders can reflect nematicity, associated with orbital or magnetic degrees of freedom as has been suggested in the Fe-based superconductors, for example[139, 140, 141], Pomeranchuk instabilities of the Fermi surface[153], or lattice instability due to steric effects, i.e. under-bonding or poor matches between ion sizes and the lattice structure. The electronic structure calculations presented here indicate that the latter is the case in $LaCu_6$.The electronic structure of orthorhombic and monoclinic $LaCu_6$ are very similar to each other in all respects, including the electronic structure near $E_F$. This implies that the phase transition is not driven electronically, $e.g.$ by an instability of the Fermi surface such as a density wave, as there is no substantial reconstruction of the electronic structure associated with the transition.

As noted in the section 5.3.3, the electronic structure of orthorhombic and monoclinic $LaCu_6$ are very similar to each other in all respects including the electronic structure near $E_F$. This implies that the phase transition is not driven electronically, e.g. by an instability of the Fermi surface such as a density wave, as

there is no substantial reconstruction of the electronic structure associated with the transition.

As noted above, another possible driver for a symmetry lowering is a Pomeranchuk instability of the Fermi surface[153]. Such a scenario would involve a strong reconstruction of the Fermi surface, as in the Fe-based superconductors at the nematic transition[154]. Transport coefficients were calculated using the BoltzTraP code[155] and find very weak monoclinicity of these in the low temperature phase. In particular the off-diagonal monoclinic component of the conductivity tensor with constant scattering time is 4.8% of the average diagonal component, while the DOS is hardly changed, and experimental evidence does not suggest sizable Fermi surface reconstruction.

These results imply that the phase transition is not driven electronically, *e.g.* by an instability of the Fermi surface such as a density wave, as there is no substantial reconstruction of the electronic structure associated with the transition. A further implication is that the structural transition does not couple strongly to electrons at the Fermi energy, meaning that only weak effects in transport and other electronic properties may be expected. Together the unstable transverse acoustic branch along $\Gamma - X$ and the decoupled electronic degrees of freedom are consistent with a ferroelastic ground state in $LaCu_6$. The variations of the transition temperature upon substitution on the La and Cu site are consistent with the characterization of the transition as a ferroelastic transition driven by size effects, specifically, substitution of a larger atom on the Cu site behaves similar to the substitution of a smaller atom on the La site[7], making a connection between the instability and size mismatch, as opposed to chemical pressure, band-width, *etc*.

Having determined that the structural transition is elastic in origin and that the electronic degrees of freedom are unimportant, thermodynamics properties with heat capacity measurements were performed to understand the critical dynamics near the QCP. Typically at a QCP, the energy scale associated with the critical fluctuations vanishes resulting in an enhanced heat capacity as the QCP is approached–the

softening of the transverse acoustic mode discussed above plays this role here. As anticipated, a larger heat capacity is observed at the putative QCP in $LaCu_{6-x}Au_x$ (Fig. 5.8(a)). The modest increase in the phonon heat capacity at $x_c$ is in line with the softening of the acoustic mode along $\Gamma - X$. The softening of a single acoustic mode is a small contribution to $\beta$ which contains contributions from all thermally accessible phonon modes. Interestingly, $\beta$ is elevated for compositions larger than $x_c$, that is the orthorhombic region of the phase diagram directly adjacent to the QCP. Measurements which directly probe the unstable acoustic mode would be particularly useful to further illuminate this issue.

Recently, the $(Ca_xSr_{1-x})_3Rh_4Sn_{13}$[116, 134] and the $(Ca_xSr_{1-x})_3Ir_4Sn_{13}$[117] series have been identified as systems that can be tuned to a displacive SQCP by application of physical or chemical pressure. In an intriguing analogy with many unconventional superconductors, the phase diagrams of these systems comprise a dome of superconductivity peaked near an SQCP[134, 135, 156]. Furthermore, the structural phase transition in these systems occurs with an abrupt change in the Fermi surface associated with a charge density wave[117, 135, 136, 137, 138]. Hence, there is a clear distinction with the QCP in $LaCu_{6-x}Au_x$ where there is no expectation (or evidence) that electronic degrees of freedom play an important role or are affected in a significant way. Also, an elastic QCP is associated with an instability of a acoustic mode rather than an optic mode as in the case of displacive SQCP. Nevertheless, there are some similarities, for example, the phonon specific heat is enhanced near the SQCP in $LaCu_{6-x}Au_x$ and somewhat more dramatically in the stannides mentioned above[116, 117]. These observations indicate that the elastic QCP studied here is fundamentally different from the displacive SQCP and the $LaCu_{6-x}Au_x$ series appears to be an ideal candidate system to further probe an elastic QCP without the complications of competing electronic phases.

## 5.5 Conclusions

In conclusion, a continuous structural phase transition in $LaCu_{6-x}Au_x$ system was suppressed via Au substitution. A phase diagram showing that the complete suppression of the structural phase transition occurs for $x_c$ = 0.3 was constructed from the results of x-ray and neutron diffraction measurements. The low-temperature phonon contribution to the heat capacity rises at the critical composition, indicating residual instability of the orthorhombic structure at low temperature. These observations indicate that the suppression of the monoclinic phase with Au-substitution in $LaCu_{6-x}Au_x$ likely results in a QCP. DFT calculations support the idea that the QCP in $LaCu_{6-x}Au_x$ arises from an elastic instability with no significant involvement of electronic degrees of freedom. Further investigation of $LaCu_{6-x}Au_x$ should prove invaluable in the elucidation of the fundamental properties of an elastic QCP.

# Chapter 6

# Quantum criticality of $CeCu_{6-x}Ag_x$

Some of the text and figures of this chapter are about to be submitted for publication in a professional journal.

In this chapter, inelastic neutron scattering (INS) measurements of the critical composition of $CeCu_{5.8}Ag_{0.2}$ are presented. A diffuse pattern of dynamic magnetic scattering in $CeCu_{5.8}Ag_{0.2}$ is observed in the (h 0 l) scattering plane. The dynamic susceptibility over a large region of momentum transfers is fit by a single phenomenological equation that yields $E/T$ scaling with a fractional exponent of 0.72(1). The fit of the phenomenological equation provides a superior description of the data compared with available theoretical models. Additional analysis of the INS measurements reveals at least two magnetic fluctuations occurring at an incommensurate and a commensurate wave-vectors, both of which are correlated in three dimensions. The incommensurate component of the magnetic fluctuations can be scaled as expected for the three dimensional HMM model.

## 6.1 Introduction

A QCP is on the verge of two distinct states of matter at zero temperature. Due to the quantum nature of fluctuations coupled with the electronic degrees of freedom, the fate of the system is determined by competition among different tendencies

that are present at the QCP[121]. Hence, measurements that shed light on the intricacy of the different tendencies in the system aids in understanding the QCPs. In this context, the heavy fermion system $CeCu_{6-x}Ag_x$ is selected for a systematic experimental investigation using INS measurements. This work demonstrates that the observed spin dynamics reflect competing magnetic fluctuations, which results in unconventional $E/T$ scaling behavior.

The quantum critical behavior in the heavy fermion series $CeCu_{6-x}Au_x$ serves as a prototype for metallic quantum criticality. However, several unique characteristics remain unexplained. Of particular interest is understanding the origin of the fractional exponent in the $E/T$ scaling. As described in section 2.7, a debate regarding the correct understanding of this experimental observation has risen, and several theoretical proposals have been made[69, 75, 76, 78, 134]. With currently available data, it is impossible to determine whether one of these proposals provides a superior description or if an entirely different theory is required. Here, the problem of $CeCu_{6-x}Au_x$ is approached in the study of a magnetically related series $CeCu_{6-x}Ag_x$.

In $CeCu_{6-x}Ag_x$, the magnetic QCP occurs at $x = 0.2$ (Fig. 4.5). In contrast with the $CeCu_{6-x}Au_x$ and $CeCu_{6-x}Pd_x$ systems, the magnetic QCP in $CeCu_{6-x}Ag_x$ occurs in the orthorhombic ($Pnma$) phase and no structural phase transition is observed at the critical composition. The long range magnetic ordering takes place at the wave-vector $\mathbf{Q}$ = (0.62 0 0.3), which is similar to that observed in $CeCu_{6-x}Pd_x$ and $CeCu_{6-x}Au_x$. Thus, the $CeCu_{6-x}Ag_x$ series presents an opportunity to study the QCP similar to $CeCu_{6-x}Pd_x$ and $CeCu_{6-x}Au_x$ without the complications of a structural phase transition. If the unconventional nature of QCP in $CeCu_{6-x}Au_x$ is the consequence of the strains or disorder in the lattice due to the presence of nearby structural phase transition, a detailed understanding of the $CeCu_{6-x}Ag_x$ system at the QCP would provide additional insight for such study.

In this chapter, a detailed investigation of the critical behavior of $CeCu_{5.8}Ag_{0.2}$ using state of art INS spectroscopy (INS) is presented. The dynamic susceptibility was measured as a function of temperature and energy transfers over a large area

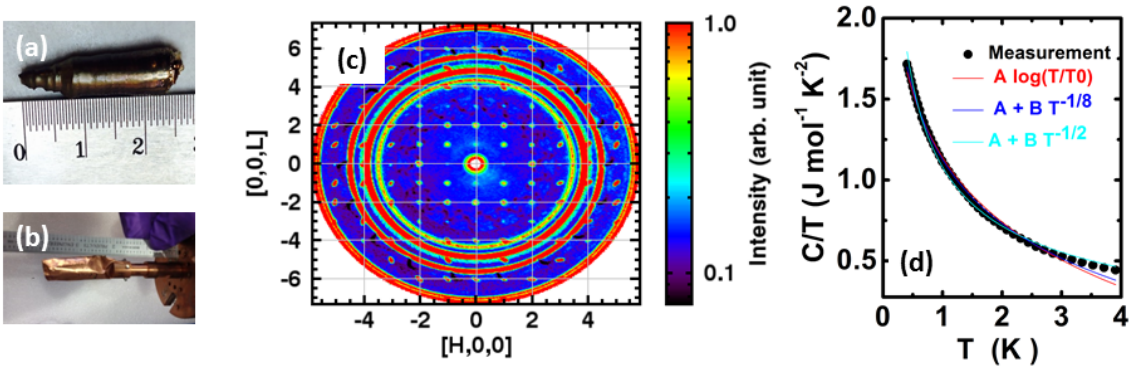



Figure 6.1: (a) A Single crystal of $CeCu_{5.8}Ag_{0.2}$ synthesized by the Czochralski process. (b) Single crystal mounted in a copper sample holder prior to the INS measurement. The sample is protected by an extra cover of copper foil which acts as a heat shield to ensure the temperature of the sample is uniform. (c) Elastic neutron scattering measurement showing structural Bragg peaks in (h 0 l) scattering plane. All major Bragg peaks are visible and can be indexed. (d) Heat capacity at zero magnetic field displaying a divergence of C/T at lower temperatures. The measurement closely agrees with previous studies[14]. Solid lines are the fit of functions shown in the Legend to the data.

of reciprocal space, and a scaling analysis was performed on several theoretical models. The dynamic susceptibility at various **Q**s are described by a single phenomenological equation which quantitatively provides a superior description of the measurements as compared to the equations derived on the basis of different theoretical approximations. The measurements also reveal the presence of multiple low energy fluctuations near the QCP, indicating that competing interactions play a central role in the quantum critical behavior. When the fluctuation spectrum is separated into two contributions, the fluctuations associated with the wave vector of the magnetically ordered region of the phase diagram exhibit a scaling commonly associated with the HMM theory. Ultimately, the competition between nearby interactions in reciprocal space drives an exotic nature of the QCP which is beyond the paradigm of the existing theoretical models.

## 6.2 Experimental Details

A single crystal of $CeCu_{5.8}Ag_{0.2}$ was grown using the Czochralski technique as described in section 3.1.2. Figure 6.1(a) shows the single crystal synthesized by the Czochralski process. The top and bottom part of the large single crystal was cut for the EDS measurements, which confirm that both ends of the single crystals are homogeneous and no compositional variation was observed. The crystal was aligned in the (H 0 L) scattering plane using the alignment station (CG-1b) at the HFIR of ORNL. The sample was mounted in a copper holder and was covered by a thin foil of copper to minimize the loss of heat due to radiation (Fig. 6.1(b)). The elastic slice of the neutron scattering measurements confirmed well-indexed nuclear Bragg peaks, verifying the single crystallinity of the sample (Fig. 6.1(c)). A heat capacity measurement was performed on the crystal in a Quantum Design PPMS with a $^3He$ option. Heat capacity at zero field shows a strong divergence of $C/T$ with temperature indicating that the sample is close to a QCP. The measurement is consistent with the literature[14].

INS measurements of $CeCu_{5.8}Ag_{0.2}$ were carried out on the CNCS of the SNS at ORNL[11]. An incident energy of 2.5 meV was used, which provides elastic energy resolution (FWHM) of 0.07 meV. The measurement was carried out at eight different temperatures (0.25 K, 0.325 K, 0.5 K, 1 K, 2 K, 4 K, 25 K, 50 K). For each temperature, the sample was rotated 110 degrees about the vertical direction in one degree steps.

The data acquisition system at CNCS records the time of flight of each neutron. The data in each detector pixel was converted into a four dimensional data set containing the dynamical correlation function $S(\mathbf{Q},\omega)$, three components of momentum transfer, and energy transfer using the computer program Mantid[157]. This reduction process considers detector tube efficiency, normalizes the data to total proton charge, and subtracts a time independent background. This reduction was performed for each position of sample rotation angle. The set of $S(\mathbf{Q},\omega)$ for all sample rotations was combined into a single dataset using the Horace suite software [158]. Some preliminary analysis was also performed using the computer program DAVE [159]. Using the combination of Matlab and Horace software, the data were sliced into a two-dimensional color picture (for example, Fig. 6.2(a) ), or cut as a one-dimensional plot along a selected energy or a momentum transfer axis.

## 6.3 Results

Before background correction, the constant energy slices within the energy interval [0.2, 0.4] are shown in Figs. 6.2(a,b,c). Plots are shown in Figs. 6.2(d), 6.2(e) and 6.2(f), which represent cuts along H, L, and energy axis, respectively. The comparison of the slices and cuts shows that the intensity near $\mathbf{Q}$ = (1 0 0) decreases with an increase in temperature, consistent with the assumed magnetic nature of scattering. The magnetic scattering disappears or becomes significantly weaker at 50 K. For all temperatures, a ring like structure is observed at low-Q regions due to the low angle background of the instrument. The scattering along [0 0 L]

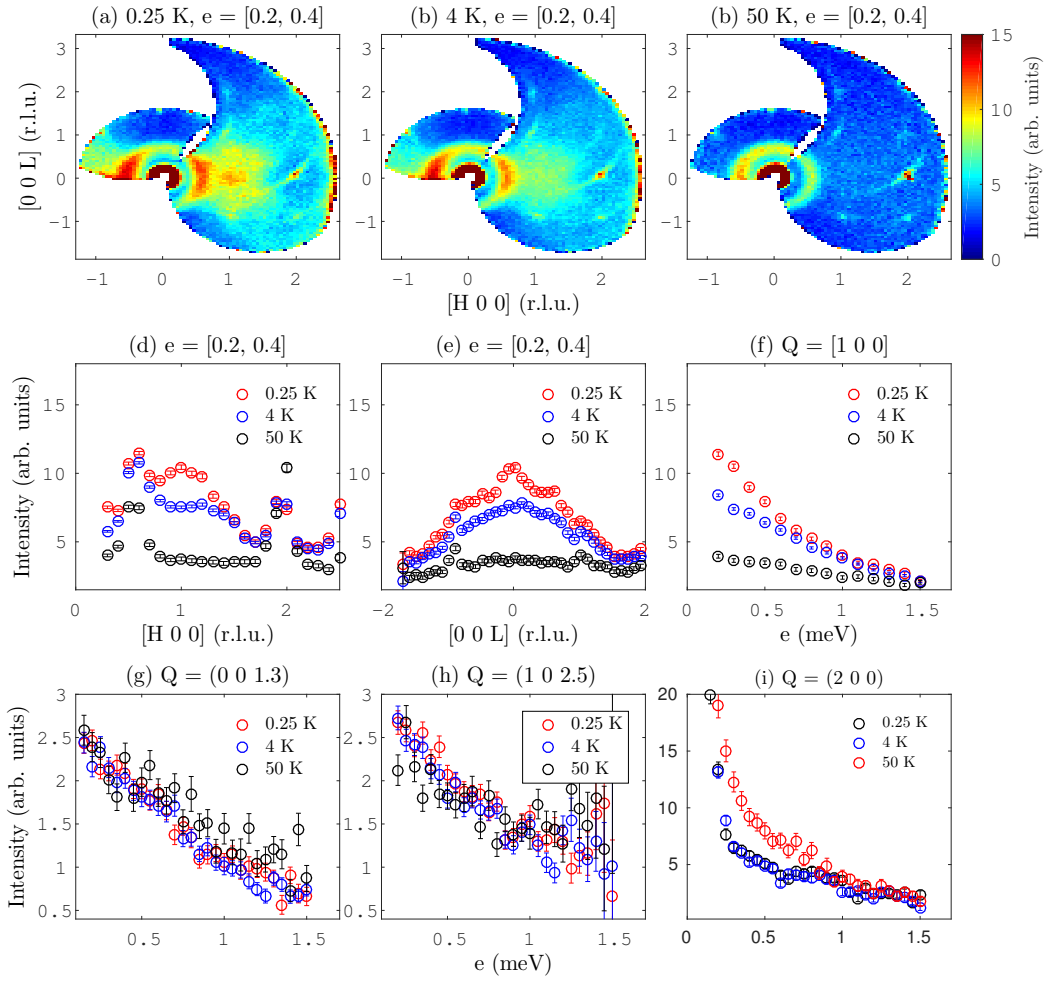



Figure 6.2: (a) Constant energy slice at 50 K averaged over the energy range e =[0.2,0.4] and $k$ =[-0.2,0.2]. The scattering is mostly attributed to the background from different sources in addition to weak magnetic scattering. The scattering at **Q** = (1 0 ± 1), **Q** = (1 0 2), **Q** = (2 0 ±1) and **Q** =(0 0 2) is due to the low frequency tail of the structural Bragg peaks. (b) The temperature dependence of cuts along the energy axis at the wave-vector **Q** = (0 0 1.2). The intensity of the scattering is independent of temperature. The **Q** independent background is taken from this wave-vector. (c) Cuts along the energy axis at the wave-vectors **Q** = (1 0 1.2) and (1 0 2.5) at 50 K. The cuts at two wave-vectors are similar. (d) The cuts along energy axis near the structural Brag peak **Q** = (2 0 0). The intensity of the scattering increases at higher temperature due the thermal population of phonons.

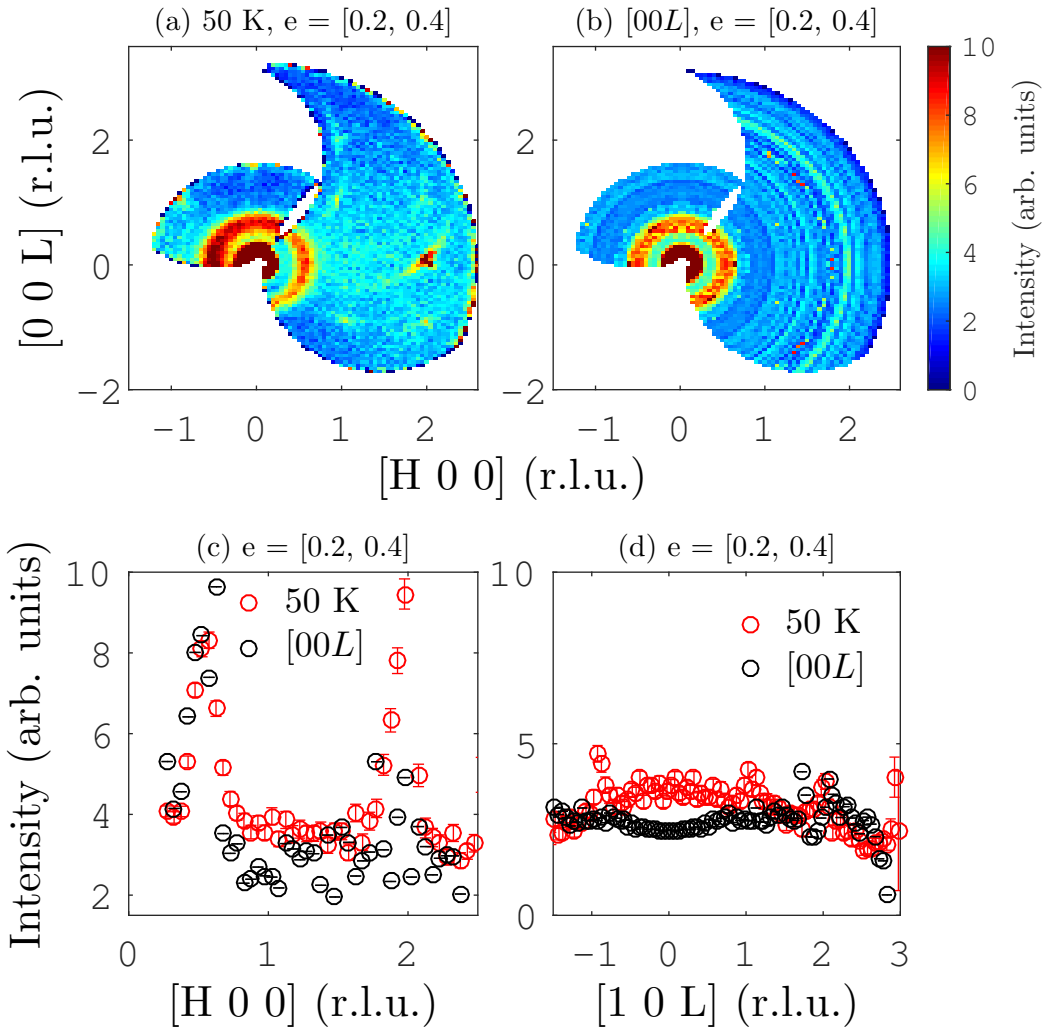



Figure 6.3: (a) Constant energy slice at 50 K. Note: this plot is a copy of Fig. 6.2(c). (b) A constant energy slice obtained by replicating the cuts along L-axis. (c) Cuts of constant energy slices(a,b) along the H-axis near (1 0 0). (d) Cuts of the constant energy slices (a,b) along the L-axis near (1 0 0).

is independent of temperature and energy transfers as shown in Fig. 6.2(g). The scattering near $\mathbf{Q}$ = (0 0 1.3) is taken to be the non-magnetic background. As a check of consistency, the intensities of the scattering at $\mathbf{Q} = (0,0,1.3)$ and $\mathbf{Q} = (1,0,2.5)$ are compared. The intensities of the scattering being similar at two different regions of the butterfly having different scattering angles provides greater confidence in the choice of background. The background near the structural Bragg peak is affected by phonons. As shown in Fig. 6.2(i), the intensity increases at higher temperature near the structural peak (2 0 0), which is attributed to the thermal population of low energy phonons. For the scaling analysis, the regions heavily affected by the phonons or the low-Q background are discarded.

The non-magnetic background is taken from the scattering along the L-axis and subtracted from the measurement. The energy dependence of the background is determined from the cuts along the energy axis at the wave-vector $\mathbf{Q}_{BG}$ = (0 0 1.3). For the scaling analysis, a non-magnetic background shown in Fig. 6.2(g) has been subtracted. The $\mathbf{Q}$-dependence of the background can be obtained from the measurement at 50 K. As shown in Fig. 6.3(a), the intensity near (1 0 0) is similar to the intensity of scattering near $\mathbf{Q}_{BG}$ = (0 0 1.3), showing that the magnetic scattering is almost completely suppressed at 50 K. The Q-dependence of the background can also be replicated from the cut along the L-axis as shown in Fig. 6.3(b), and it compares well with the 50 K measurement shown in 6.3(a). A clearer comparison is presented in Figs. 6.3(c) and 6.3(d). This comparison reinforces the legitimacy of the choice to use 50 K as the background. Furthermore, the 50 K measurements were performed with the same experimental configurations (*e.g*, sample rotation angle, cryostat, and sample orientation) and account for the non-magnetic background created by the rotation of sample as well as unknown sources.

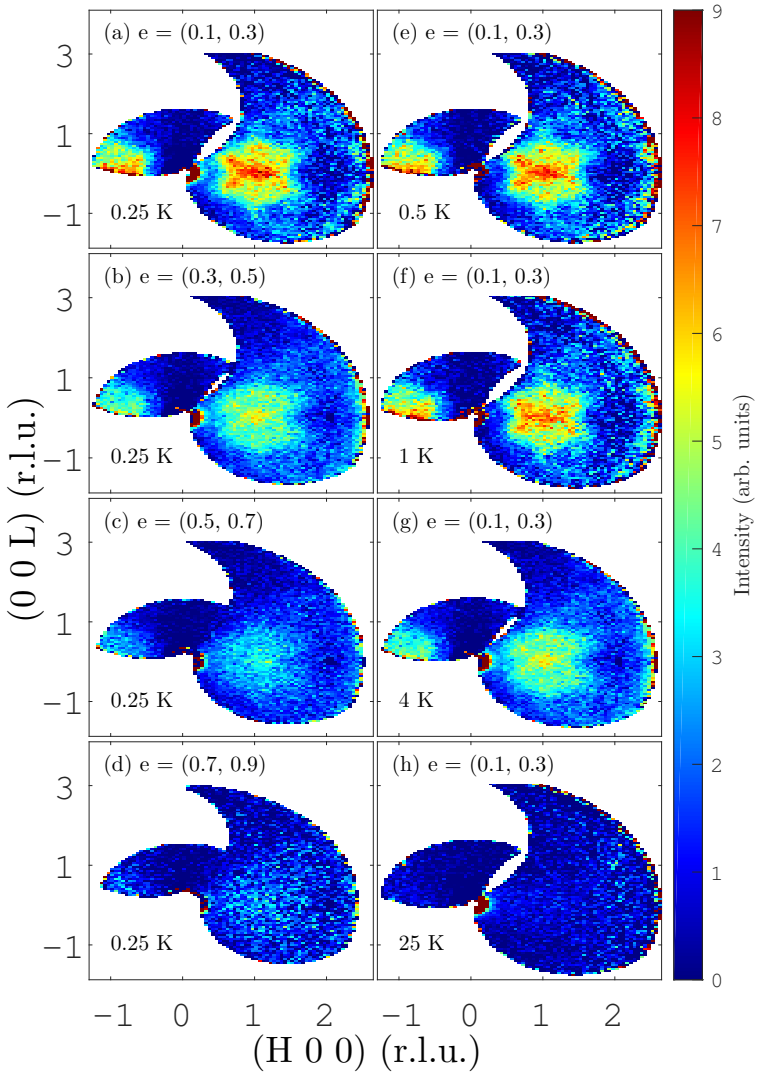



Figure 6.4: Constant energy slices of the neutron scattering data for $CeCu_{5.8}Ag_{0.2}$ in (h 0 l) scattering plane. (a-d) displays the energy dependence of the scattering at 0.25 K, and (e-h) displays the temperature dependence at 0.1 meV. In all panels, the data collected at 50 K is used as the background and is subtracted from the data. Each pixel in the plot represents the integrated intensity in the area of dimension $(0.05)^2$ r.l.u.$^2$.

### 6.3.1 Dynamic Critical Scattering of $CeCu_{5.8}Ag_{0.2}$

Figure 6.4 shows the evolution of the magnetic scattering with energy and temperature. Magnetic scattering is observed in the form of a diffuse pattern centered at **Q**=(100). The resolution of the measurement at the elastic line is 0.07 meV. The intensity of the scattering is maximum at the center. With an increase in energy, the intensity of scattering decreases and scattering becomes more diffuse as shown in Figs. 6.4(a-d). A qualitatively similar situation arises when temperature, instead of energy transfer, is increased. As shown in Figs. 6.4(e-h), the pattern of scattering remains essentially unchanged until 1 K but becomes more diffuse at higher temperatures.

### 6.3.2 $E/T$-scaling

For a more quantitative analysis of the magnetic scattering, the INS measurement was compared with the scaling equations derived from different models described in the section 2.7. In this section, the scaling analysis with reference to the different models is presented.

The imaginary part of dynamic susceptibility was extracted from INS measurement using equation 3.19. A global fit of the scaling equations was performed to the imaginary part of dynamic susceptibility taken from various $\mathbf{Q}, T, E$. For the ease of comparison, the scaling analysis for the different models were performed within the same range of $Q$, $E$, $T$. The **Q**-dependent function is considered a fitting parameter for each model. The data are plotted as the dimensional ratio $E/T$ in the x-axis and the quantity $\chi'' T^{\alpha}$ in the vertical axis.

#### Phenomenological $E/T$

For a paramagnetic system, the Curie-Weiss law can be written in the form, [24].

$$\chi(\mathbf{Q}, E, T) = \frac{C}{\theta(\mathbf{Q} - \mathbf{Q}_0) + (T - iE)^{\alpha}} \tag{6.1}$$

where $\theta(\mathbf{Q}-\mathbf{Q}_0)$ is a Curie-Weiss temperature that represents the wave-vector dependence of the magnetic fluctuations. In mean-field theory, $\alpha = 1$.

This equation yields $E/T$-scaling when the Weiss temperature $\theta(\mathbf{Q}-\mathbf{Q}_0)$ is zero. This result is only possible when $\mathbf{Q} = \mathbf{Q}_0$ (i.e., at the critical wave-vector). Under that condition, equation 6.1 can be written as,

$$\chi(\mathbf{Q},E,T) = T^{-\alpha}\frac{C}{(1-iE/T)^{\alpha}} = T^{-\alpha}g(E/T) \tag{6.2}$$

where the scaling function $g(E/T)$ depends only on the dimensionless ratio $E/T$. The value of equation (6.2) is that the quantity $\chi\ T^{-\alpha}$ depends only on the dimensionless ratio $E/T$ despite the microscopic details of the system, and is thus termed $E/T$ scaling.

At $T = 0$, equation 6.1 reduces to another scaling equation.

$$\chi(\mathbf{Q},E) = [\theta(q)]^{-\alpha}\frac{C}{(1-iE/\theta(q))^{\alpha}} = [\theta(q)]^{-\alpha}g(\theta(q)/T) \tag{6.3}$$

The fit of equation 6.1 yields $\alpha = 0.72(1)$. The measurement and fit for different regions of the (h 0 l) scattering plane is presented in Fig. 6.5(a-c). Consistent with equation 6.2, the susceptibility at different temperatures collapses onto a single curve displaying an $E/T$ scaling at the center of the diffuse scattering pattern, $\mathbf{Q}_0$ = (1 0 0) (Fig. 6.5(a)). The overlap becomes less pronounced as the magnitude of $\mathbf{q} = (\mathbf{Q}-\mathbf{Q}_0)$ increases. The deviation from the $E/T$-scaling at higher $\mathbf{q}$ is captured by $\theta(\mathbf{q})$ of equation 6.1. The values of $\theta(\mathbf{q})$ as a function of $q = |\mathbf{Q}\text{-}\mathbf{Q}_0|$ are presented in Figure 6.5(d), which shows that $\theta(\mathbf{q})$ varies quadratically near the center of the pattern (q = 0). As an alternative test of the phenomenology, an $E/\theta(q)$ scaling analysis was also performed at the base temperature of 0.25 K. The dynamic susceptibility at the base temperature fits well with the equation 6.3 and the quantity $\chi''(\theta(q))^{-\alpha}$ at different $\mathbf{q}$s overlap into a single curve displaying an $E/\theta(\mathbf{Q})$ scaling. This observation verifies that the measurement fits well with the phenomenological

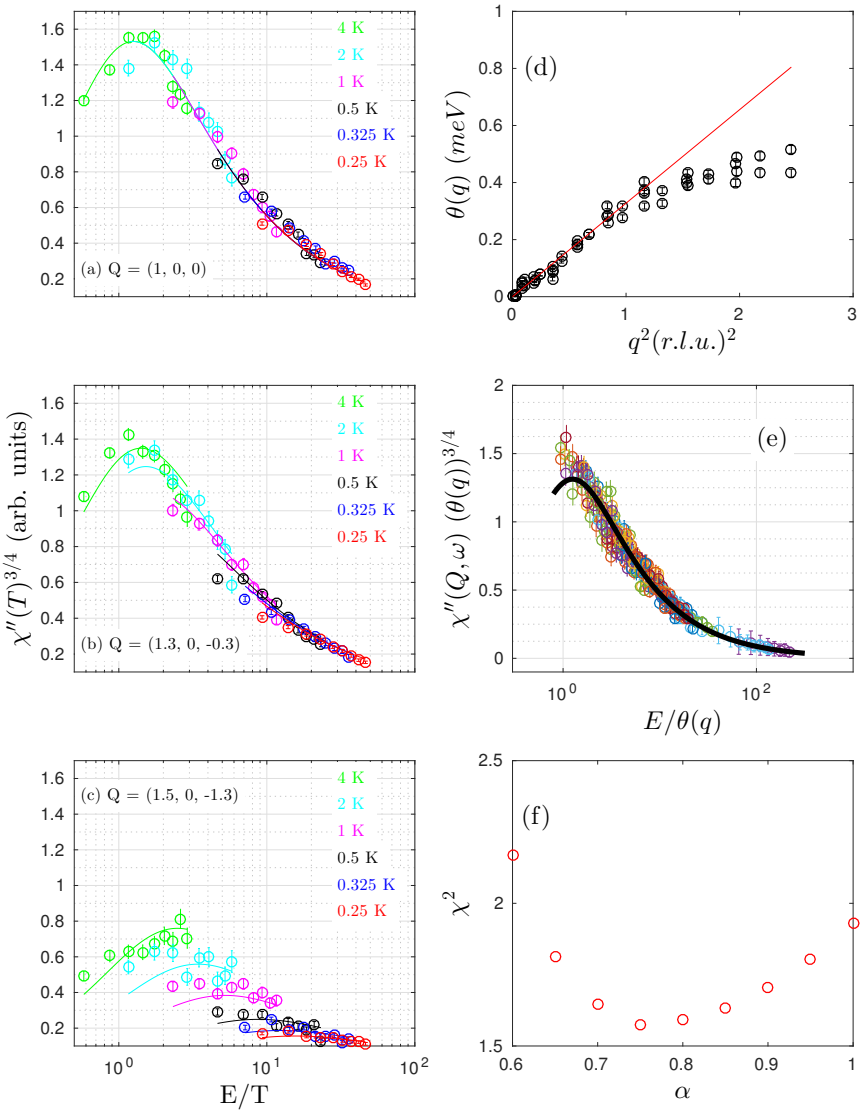



Figure 6.5: (a-c) Scaling analysis of the imaginary part of dynamic susceptibility in different regions of reciprocal space. The solid lines are the fit of the phenomenological equations 6.1 to the data. (d) The fit yields the **q**-dependent term $\theta(q)$. Near **q** = 0, $\theta(q) \approx \mathbf{q}^2$ (red line). (e) Dynamic susceptibility at 0.25 K scaled as a function of $E/\theta(q)$. As anticipated from equation 6.3, the susceptibility at different **Q**s collapse onto a single curve showing $E/\theta(q)$-scaling. The solid line is the fit of equation 6.3 to the data. (f) The variation in the goodness of fit parameter $\chi^2$ with the scaling exponent $\alpha$. The best fit is obtained near $\alpha$=0.72.

equation 6.1. The goodness of fit parameter is shown in Fig. 6.5(g), attesting that the scaling exponent $\alpha$ = 0.72(1).

### "local QCP" model

Fig. 6.6 displays the best fit of equation 2.15 to the data. As shown in Figure 6.6(a), the fitted lines at different temperatures converge into a single curve displaying an $E/T$ scaling at the center of diffuse scattering. For all other $\mathbf{Q}$s, the fitted lines at different temperatures deviate from each other, and the deviation becomes more robust as $\mathbf{Q}-\mathbf{Q}_0$ increases (Fig. 6.6(a-f)). The deviation from $E/T$-scaling is captured by the $Q$-dependent function $f(\mathbf{Q}-\mathbf{Q}_0)$ in equation 2.17, which appears to be a quadratic function of $(\mathbf{Q}-\mathbf{Q}_0)$ near the center of the diffuse pattern(Fig. 6.6(a-f). The fit also yields the exponent $\alpha$ = 0.73(1), which is close to the expected value[71, 72, 73].

While the fit of the scaling equation is close to the data at different temperatures, and the $Q$ dependence of the function $f(Q)$ agrees with the "local" QCP model, the scaling equation overpredicts the susceptibility as $E \approx T$ as compared to the phenomenological equations.

### Strong-coupling

The fits of equation 2.24 in different regions of the scattering plane are displayed in Figure 6.7. Although the fits look very close to the data, the momentum dependent variable $S(\mathbf{Q}-\mathbf{Q}_0)$ appears to be linearly dependent on $\mathbf{Q}-\mathbf{Q}_0$, showing that the scaling equation 2.24 does not describe the measurements (Fig. 6.8). The scaling equation, however, fits well at the center of butterfly $\mathbf{Q}=\mathbf{Q}_0$ = [100].

### XY-dissipation

The $\mathbf{Q}$-dependence of $\chi''(\mathbf{Q})$ near $\mathbf{Q}$= (1 0 0) is shown in Figure 6.9(a). The plot shows that the width changes with energy transfer, which is consistent with the observation

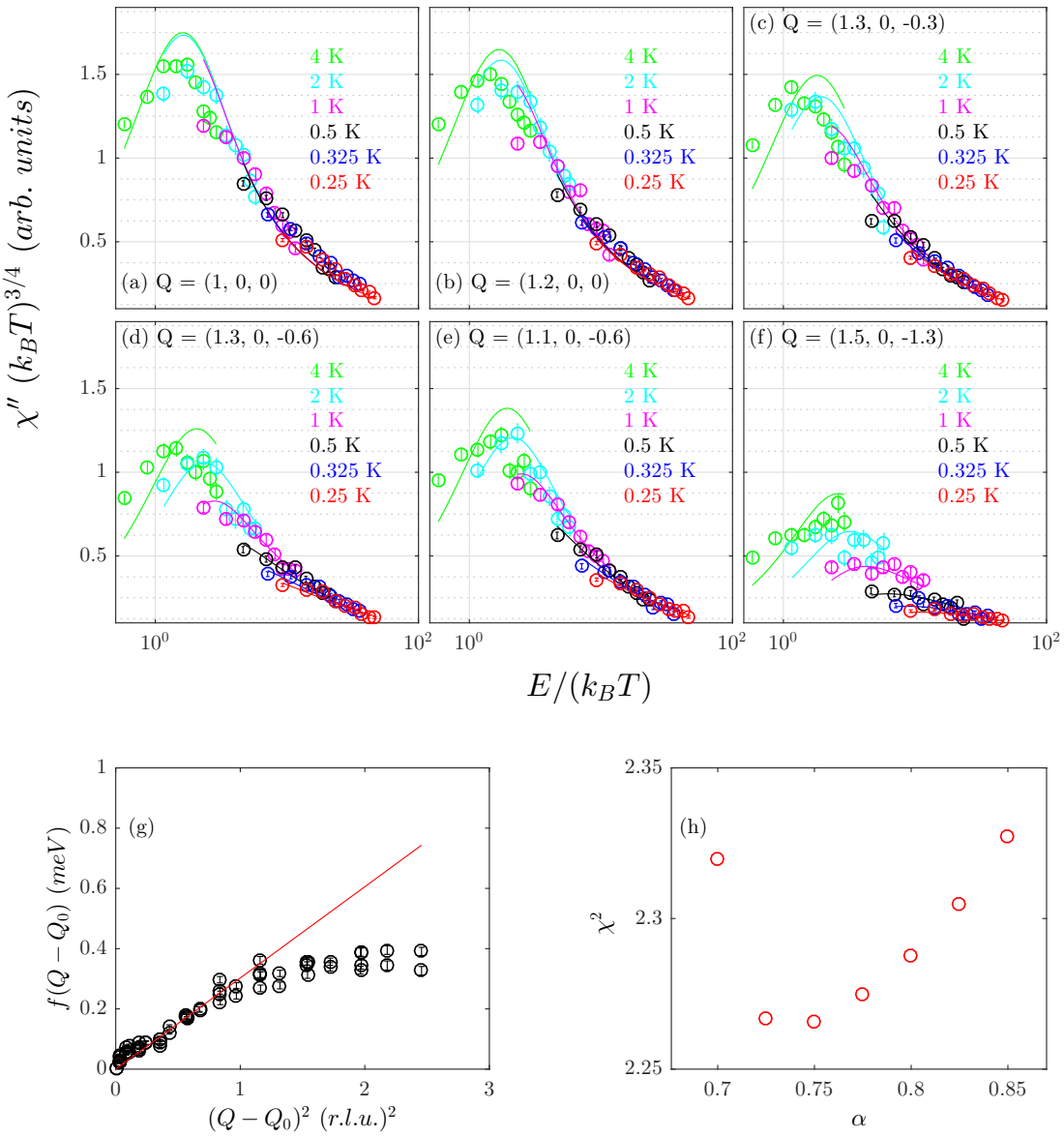



Figure 6.6: Scaling analysis of equation 2.15 to the data. (a-f) Measurement at different temperatures scaled as a function of $E/T$. The solid lines are the fit of equation 2.15 to the data. The fitted lines at different temperatures converge only at the center of the scattering, $\mathbf{Q}$ = (1 0 0) and deviate away from the center. The $\mathbf{Q}$-dependent function in equation 2.15 is considered as a fitting parameter. (g) The variation of $f(\mathbf{Q}-\mathbf{Q}_0)$ as a function of $\mathbf{Q}-\mathbf{Q}_0$. Near $Q_0$, the function is quadratic in $\mathbf{Q}-\mathbf{Q}_0$. (h) The goodness of fit parameter ($\chi^2$) as a function of scaling exponent, $\alpha$. The best goodness of fit parameter is obtained when $\alpha$ = 0.73(1).

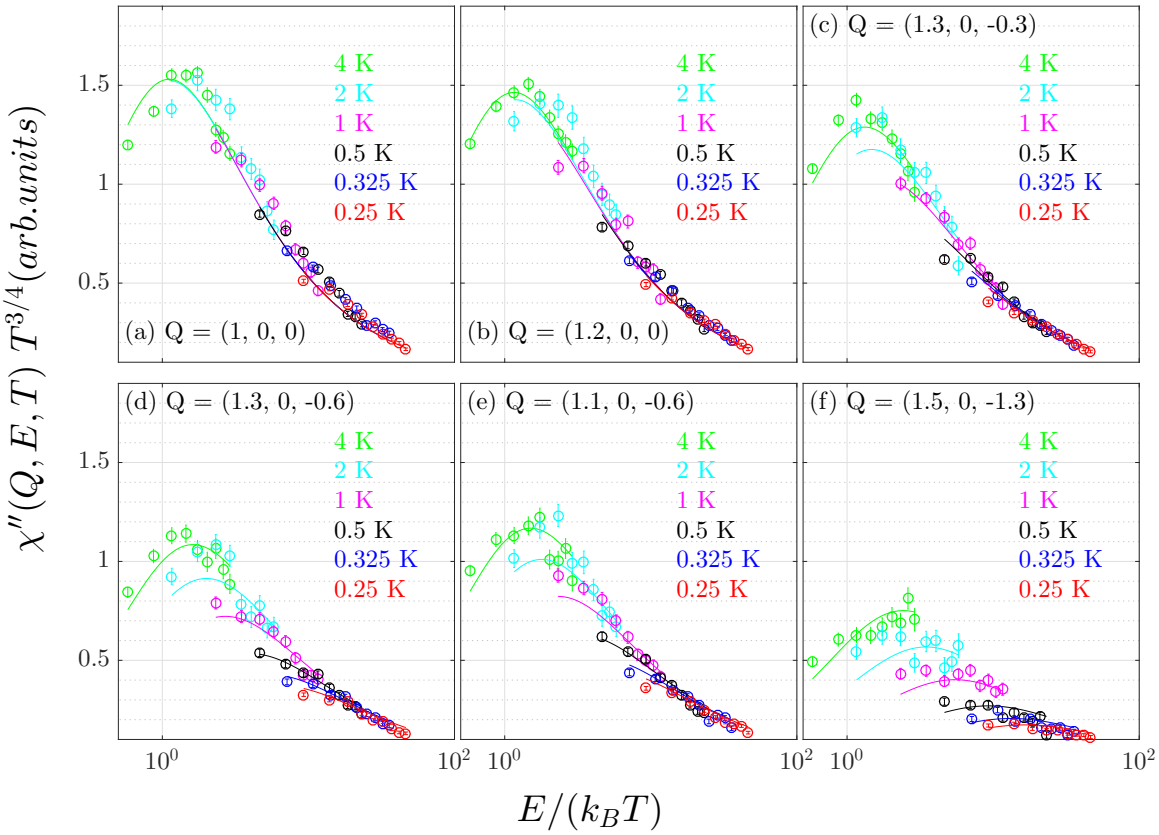



Figure 6.7: Scaling analysis with reference to the strong-coupling model. Solid lines represent a fit of equation 2.24 to the data. The **Q**-dependent function S($\mathbf{Q}-\mathbf{Q}_0$) is taken as a fitting parameter. Panels(a-f) represent different regions of the magnetic scattering.

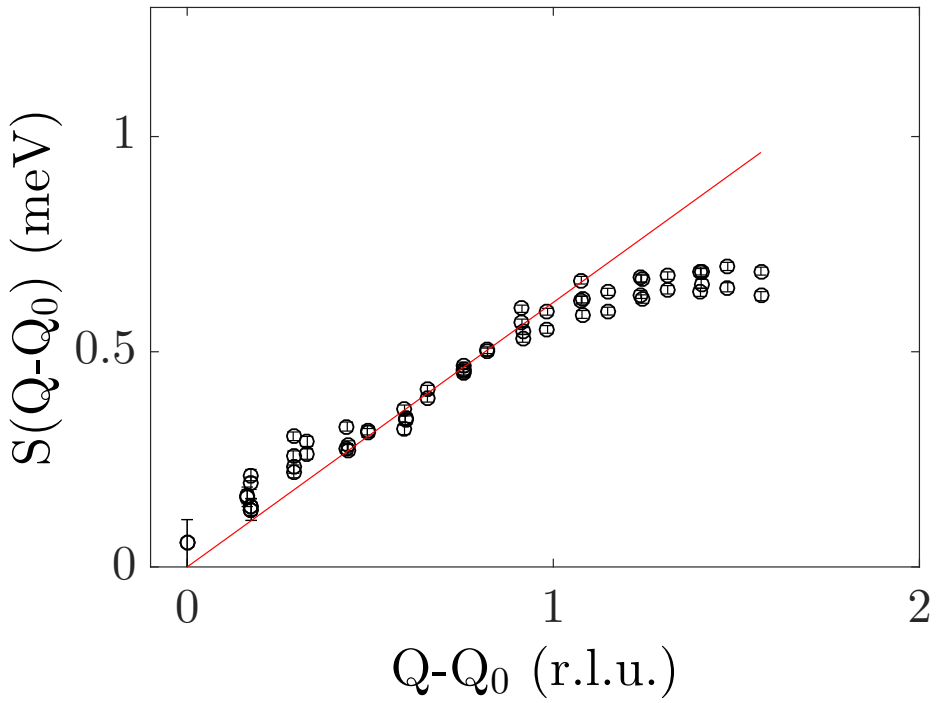



Figure 6.8: Dependence of $S(\mathbf{Q}-\mathbf{Q}_0)$ on $(\mathbf{Q}-\mathbf{Q}_0)$. The values of $S(\mathbf{Q}-\mathbf{Q}_0)$ were obtained from a global fit of equation 2.20 to the data as presented in FIg. 6.7.

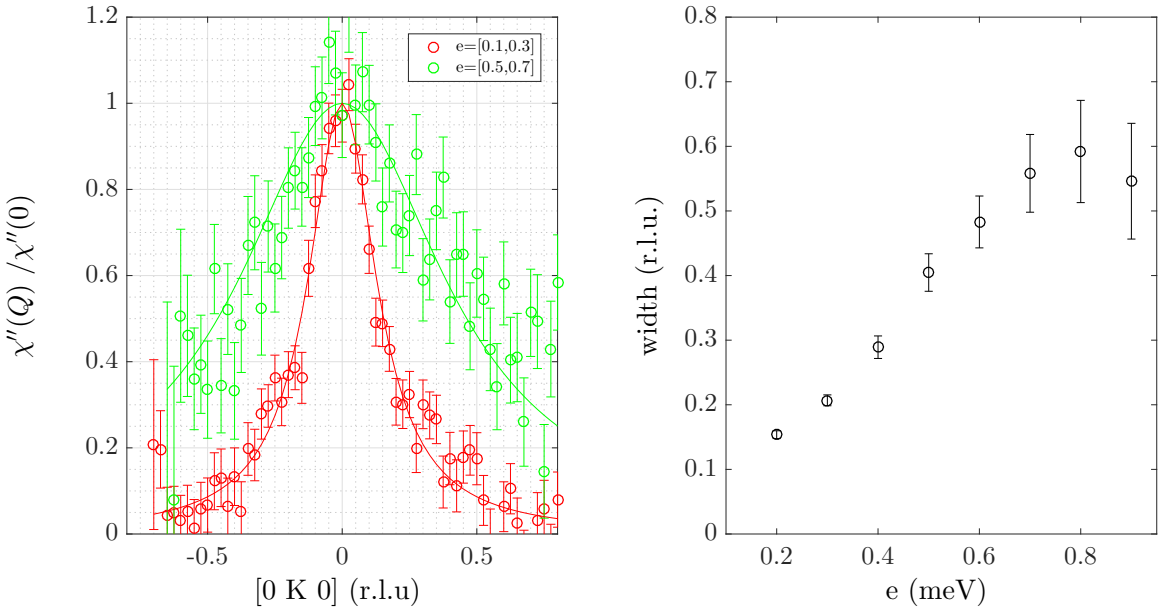



Figure 6.9: (a) Cuts along (0 1 0) axis at $\mathbf{Q}$ = (1 0 0) at two energy transfers normalized to the peak value. A fit of simple Lorentzian function was performed to estimate the widths of the peaks. The change in the widths of the cuts is not expected from the XY-dissipation model. (b) The variation of widths of the cuts with energy transfers. The widths increase with energy.

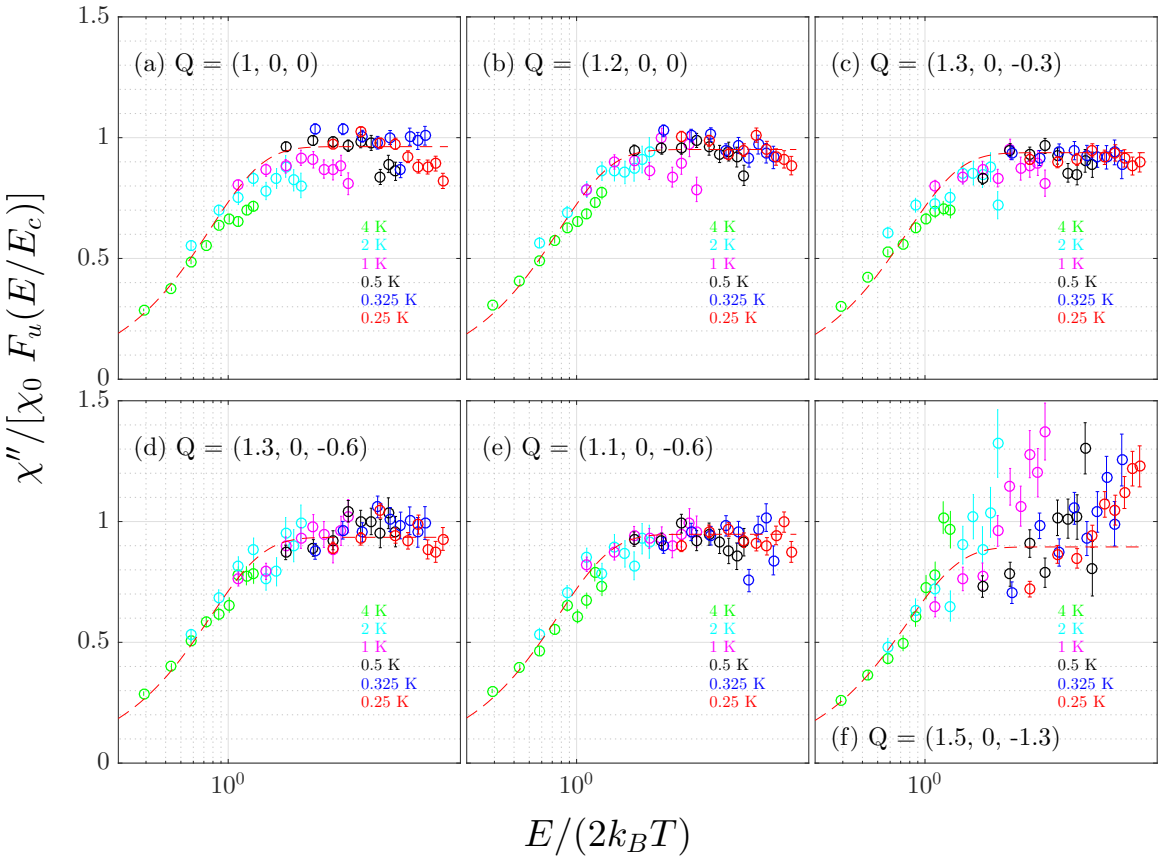



Figure 6.10: Scaling analysis of Ag with reference to the XY-dissipation model. Each panel corresponds to the wave-vectors in different regions of the scattering. The y-axis is the dynamic susceptibility scaled by $F_u(E/E_c) \propto \frac{1}{\sqrt{1+(E/E_c)^2}}$. The $\mathbf{Q}$ -dependent function, $F(\mathbf{Q}-\mathbf{Q}_0)$, is fitted as a parameter. The dotted line represents hyperbolic tangent of $E/2T$.

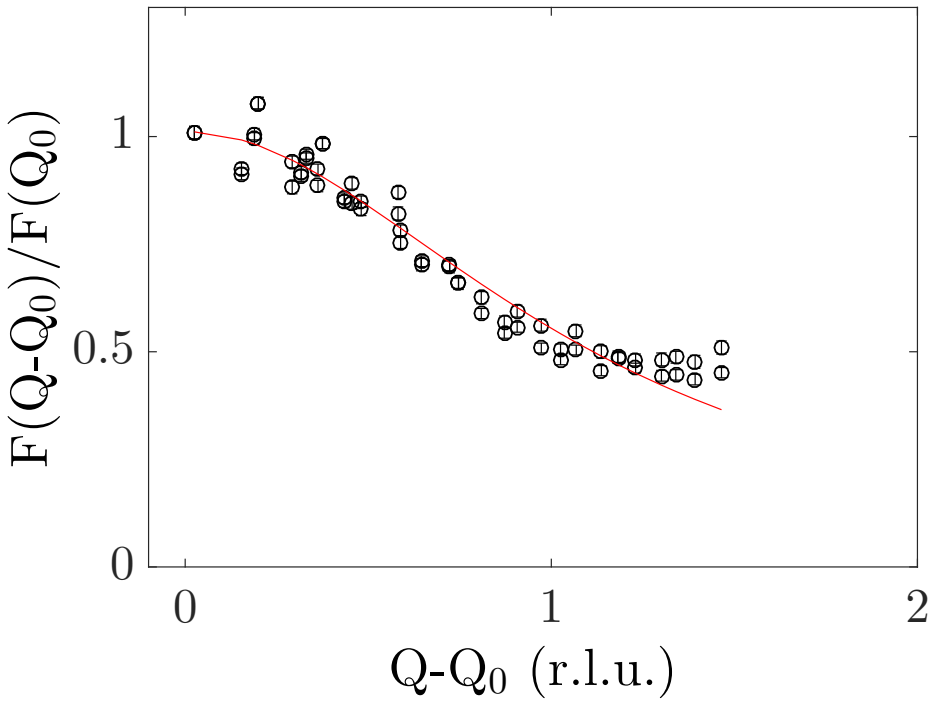



Figure 6.11: Variation of $F(\mathbf{Q}-\mathbf{Q}_0)$ obtained from the fit of the equation 2.29. The fits are as presented in Fig. 6.10. The solid red line is fit of the Lorentzian function.

that the scattering becomes more diffuse at higher energy and temperatures. The Lorentzian widths of the cuts increase at higher energy transfers as shown in Figure 6.9 (b). The change in correlation length with energy transfer is not consistent with the fundamental assumption of the XY-dissipation model, which states that the fluctuations are separable in $\mathbf{Q}$ and $E, T$.

The fit of the scaling equation 2.29 is presented in Figure 6.11. Here, the cutoff energy $E_c$ and the $\mathbf{Q}$-dependent function F($\mathbf{Q} - \mathbf{Q}_0$) are taken as a fitting parameter. The fit of equation 2.29 to the data yields the $E_c$ = 0.35(1) meV, which is close to the cuttoff energy estimated for the related system $CeCu_{6-x}Au_x$[160].

**Summary of Comparison to Existing Theory**

The observed $E/T$ scaling with the exponent 0.72(1) implies a spectacular deviation from the conventional HMM approach. Similar behavior is reported in the related system $CeCu_{6-x}Au_x$, and it has been portrayed as a poster child of these three QCP models. As demonstrated earlier, the scaling equations derived from these models were extensively tested with the measurement. While many aspects of these models are tantalizingly close to the measurement, none of these models fits better than the phenomenological $E/T$ scaling. The superiority of the phenomenological equation as compared to that of the theoretical models indicates that the existing theoretical framework does not provide an adequate description of the critical behavior of $CeCu_{5.8}Ag_{0.2}$.

### 6.3.3 Unveiling Competing Fluctuations

A central question concerning the nature of the quantum critical behavior in $CeCu_{6-x}Ag_x$ is what type of spin-spin correlation(s) in real space gives rise to a butterfly shaped pattern in the (h 0 l) scattering plane. The magnetic order in $CeCu_{6-x}Ag_x$ propagates with the incommensurate wave-vectors $\mathbf{Q}_1$ = (0.65 0 ±0.3) and is independent of Ag composition[86]. Hence, the critical scattering is generically

expected at the wave-vector (0.65 0 ±0.3) and equivalent regions of higher Brillouin zones (1.35 0 ±0.3). However, the correlations centered at these four spots neither result in a butterfly shaped pattern nor justify the maximum intensity at the center $\mathbf{Q}_2$ = (1 0 0). For a more quantitative understanding of these fluctuations, a sum of two two-dimensional Lorentzian functions in the following form was used.

$$y = \frac{A}{1 + (\xi_{\parallel}\cos(\theta)(Q_h - Q_{h0}))^2 + (\xi_{\perp}\sin(\theta)(Q_l - Q_{l0}))^2} \tag{6.4}$$

Here, $\xi_{\parallel}$ and $\xi_{\perp}$ are the components of the real space correlation lengths along an arbitrary axis and perpendicular to the axis. $\theta_0$ is the angle between the arbitrary axis and [H 0 0] in the reciprocal space. The fluctuation is centered at the wave vector $\mathbf{Q}$ = $(Q_{H0}, 0, Q_{L0})$. $\theta$ measures the angle between the wave-vector $\mathbf{q}$= ($Q_H - Q_{H0}$, 0, $Q_L - Q_{L0}$) and the arbitrary axis. A sketch indicating the relative orientation of the parallel and perpendicular components of the correlation length in reciprocal space geometry is shown in Fig. 6.12.

The fit of equation 6.4 provides a good description of the data at all temperatures and energy transfers. An example of the fit is shown in Fig. 6.13(b), which consists of two two dimensional Lorentzians shown in Fig. 6.13(c) and Fig. 6.13(d). One dimensional cuts are also shown in Fig. 6.13(e,f) for clarity. The quality of the fits implies that another competing fluctuation is centered at the wave-vector $\mathbf{Q}_2$ = (1 0 0) and that the overlap of these two fluctuations renders a butterfly shaped pattern. In real space, this observation refers to the presence of two similar tendencies by which the system can achieve a magnetically ordered ground state. There is a natural relationship between these two types of fluctuations, the fluctuation at (100) reflecting the tendency for commensurate rather than incommensurate order. The fit provides a good description of the data at all temperatures and energy transfers.

The measurement was also compared with equation 6.4 under different assumptions (Fig. 6.14). First, as is suggested in the literature[63], an assumption was made that the fluctuations are two-dimensional in real space, i.e., the correlation

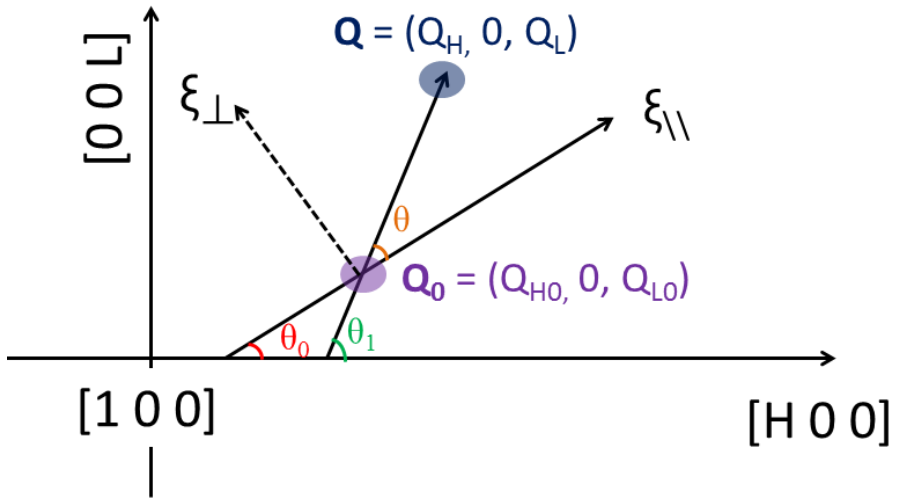



Figure 6.12: Reciprocal space geometry showing the relative orientation of correlation length vector $\xi$ with the $\mathbf{Q}$. $\xi_{\parallel}$ and $\xi_{\perp}$ are the parallel and perpendicular components of correlation length vector. The parallel axis is at an angle $\theta_0$ from reciprocal [H 0 0] axis (crystallographic $a$ axis in real space). The fit of constant energy slice yields $\theta_0 = 71°$. The magnetic correlation is centered at $\mathbf{Q}_0 = (Q_{h0}, 0, Q_{l0}$. Wave-vector $\mathbf{Q} = (Q_h, 0, Q_l)$ is a variable in the scattering pane.

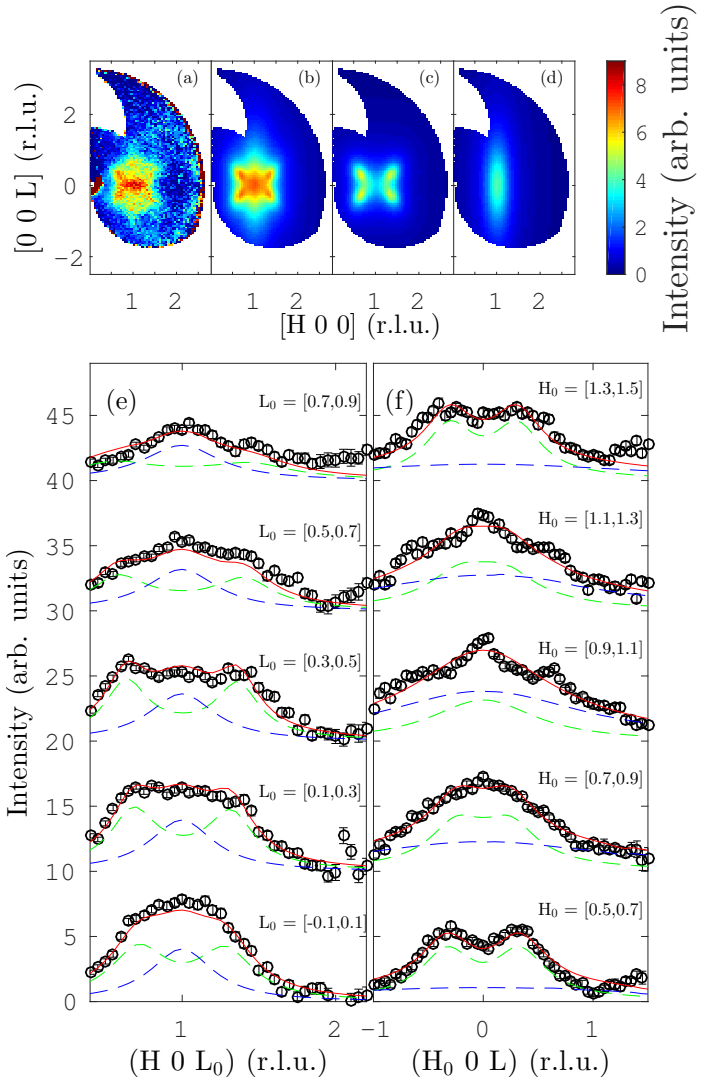



Figure 6.13: (a) Constant energy slice at 0.25 K averaged over an energy range e =[0.15,0.25] after a 50 K background subtraction. (b) The parametrization of slice as a superposition of two independent magnetic fluctuations shown in (c) and (d). (c) Magnetic fluctuation centered at the **Q** =[0.65 0 0.3] and symmetry related regions. Panel (d) The magnetic fluctuation centered at **Q** = (1 0 0). (e,f) Cuts along (e) (H 0 0) and (f) (0 0 L) axis each integrated within E = [0.15,0.25] meV. The red line is the fit of two Lorentzian functions described in the text. The blue and green dotted lines represent the contribution from the magnetic fluctuations centered at commensurate and incommensurate wave-vectors, respectively.

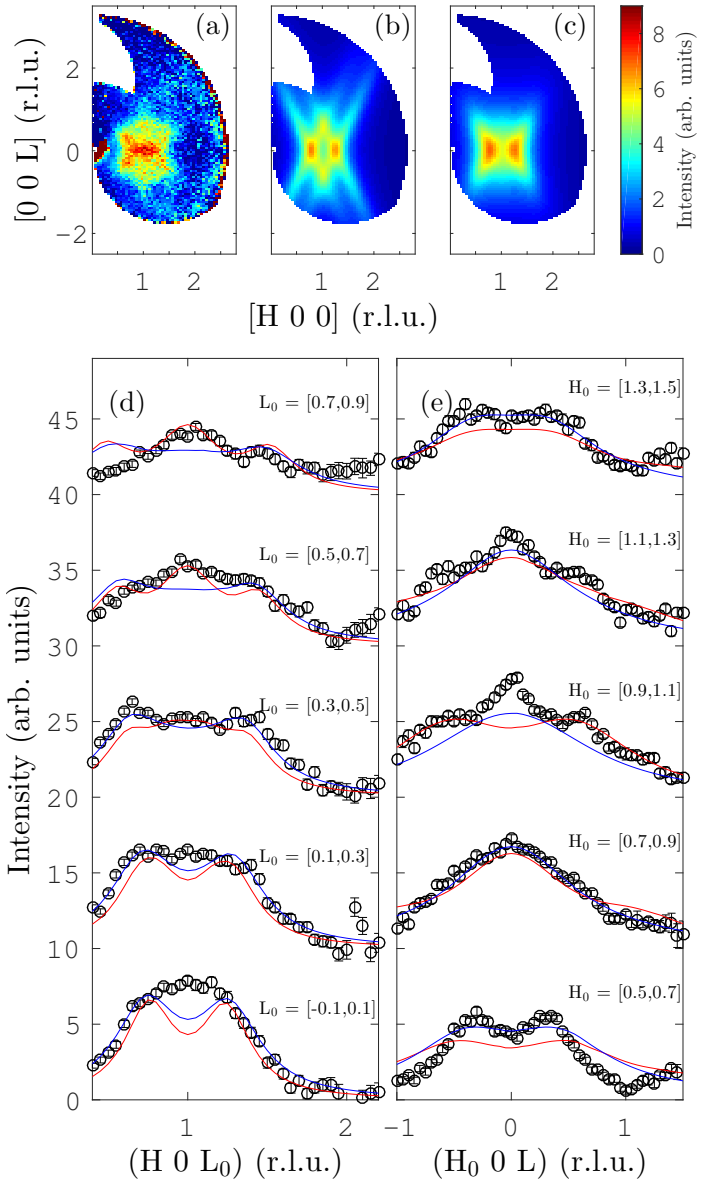



Figure 6.14: (a) Constant energy slice at 0.25 K cut within the energy interval of e = [0.075,0.275]. A background collected at 50 K is subtracted from the data. (b,c) The best fit of equation 6.4 to the **Q** slice obtained by (b) constraining the correlation lengths to differ by an order of magnitude (c) without any constrains in the correlation lengths. (d,e) Plots showing one dimensional cuts of slice (a,b,c). The black circles represent slice shown in (a). The red and blue lines represent the cuts of the pattern shown in (b) and (c), respectively.

lengths along an arbitrary axis differ by an order of magnitude perpendicular to the axis. And since the critical wave-vector in $CeCu_{6-x}Ag_x$ is $\mathbf{Q}_1$ = (0.65 0 ±0.3), the intensity of critical scattering is expected to be maximum at (0.65 0 ±0.3) and (1.35 0 ±0.3). A fit of four two dimensional Lorentzians each centered at these four spots of the (h 0 l) scattering plane was performed to the constant energy slice. To verify the assumption that the fluctuations are two-dimensional, the correlation lengths along the parallel and perpendicular axis are constrained to differ at least by an order of magnitude. The best fit obtained under that assumption is shown in Fig. 6.14(b), which is clearly different from the measured slice shown in Fig. 6.14(a). When the constraints on the correlation lengths are released, a slightly better fit is obtained (Fig. 6.14(c)); however, the correlation lengths obtained from the fit are in the same order of magnitude, ruling out the possibility that the fluctuations are two dimensional in real space. For a clearer comparison between the fits and the measurement, cuts along [H 0 0] and [0 0 L] are shown in Fig. 6.14(d) and Fig. 6.14(e).

This analysis clearly demonstrates that the picture of two dimensional fluctuation is not sufficient to describe the measurement and, more importantly, that the magnetic scattering in $CeCu_{5.8}Ag_{0.2}$ can not be described as a result of a single fluctuation. Therefore, the approach presented in Fig. 6.13, which considers an additional non-critical magnetic fluctuation, is the simplest model describing the measurement. The scattering therefore can be parametrized as an overlap of two fluctuations near a critical wave-vector $\mathbf{Q}_1$ = (0.65 0 ±0.3) and a non-critical term $\mathbf{Q}_2$ = (1 0 0). Under this assumption, the correlation lengths and the spectral weight of each fluctuation are estimated from a fit of equation 6.4 to the constant energy slices cut at different temperatures and energy transfers. The correlation lengths along the parallel and perpendicular axis are in the same order over the entire spectrum (Figs. 6.15(b,c)). However, the fluctuations near $\mathbf{Q}_2$ is gapped with an energy transfer of 0.3 meV (Fig. 6.15(d)). The correlation lengths of $\mathbf{Q}_2$ along $a$ and $c$-axis are in the same order, meaning that the magnetic fluctuations are three dimensional.

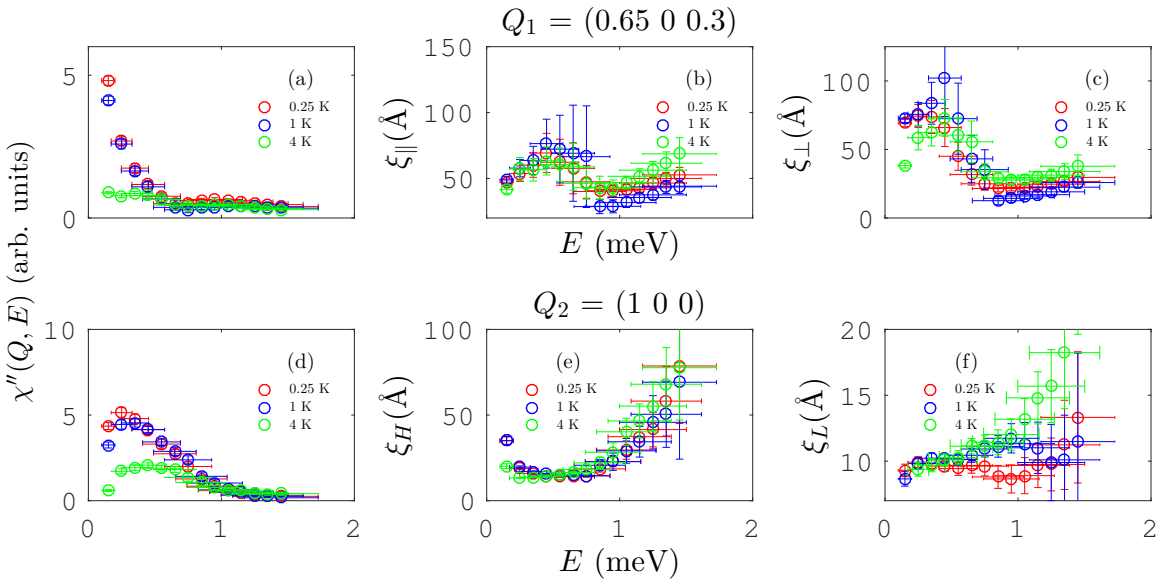



Figure 6.15: Spectral weights and the real space correlation lengths extracted from the fit of a two dimensional Lorentzian function. (a) The spectral weight of the fluctuations centered at an incommensurate wave-vector $\mathbf{Q}_1$ = (0.65 0 ±0.3) (b,c) Real space correlation lengths along (b) parallel and (c) perpendicular to the axis. (d) Spectral weight of the non-critical fluctuations centered at $\mathbf{Q}_2$ = (1 0 0). Subplot (e) and (f) are the real space correlation lengths along the $a$ and $c$-axis of crystal structure.

As shown in Fig. 6.15 fluctuations at $\mathbf{Q}_1$ are quasielastic, whereas $\mathbf{Q}_2$ appears to be inelastic with a small energy gap, suggesting that $\mathbf{Q}_1$ is the only mode that goes critical at the QCP. The critical component is expected to be at the incommensurate wave-vector $\mathbf{Q}_1$ based on the previous neutron diffraction measurement that shows $CeCu_{6-x}Ag_x$ orders only at the wave-vector close to $\mathbf{Q}_1$[86]. The non-critical fluctuation $\mathbf{Q}_2$ may be a vestige of the parent compound $CeCu_6$ in which strong magnetic fluctuations are observed near $\mathbf{Q}_2$ with a similar energy scale as determined from the analysis of the QCP composition[47, 48]. Thus, it is not entirely unexpected that dynamic magnetic scattering occurs near both wave-vectors $\mathbf{Q}_1$ and $\mathbf{Q}_2$ as the QCP is situated at the borderline of two different phases at zero temperature.

Since the magnetic scattering in $CeCu_{5.8}Ag_{0.2}$ comprises the critical fluctuations at $\mathbf{Q}_2$ in addition to a non-critical mode $\mathbf{Q}_1$, an interesting question is how the critical part of dynamic susceptibility scales as a function of energy and temperature. Since the critical part of the fluctuations is three dimensional, conventional SDW theory predicts that the critical dynamic susceptibility can be scaled as a function of $E/T^{3/2}$. Indeed, an $E/T^{3/2}$-scaling is observed in the critical part of the dynamic susceptibility. As shown in Fig. 6.16(a), the quantity $\chi'' T^{3/2}$ at different temperatures collapses into a single curve. The critical part of the spectrum fits well with the equation $\chi'' = T^{-3/2} f(E/T^{3/2})$, which illustrates that certain aspects of the critical behavior of $CeCu_{6-x}Ag_x$ is consistent with the HMM model.

Competing magnetic fluctuations appear to be a common feature among Ce-based QCPs. $CeCu_{6-x}Ag_x$, nonetheless, clearly differs from the remaining Ce-based QCPs that the competition is between nearby fluctuations in the reciprocal space. A remarkably similar situation is also reported in the heavy fermion system $YbRh_2Si_2$, in which ferromagnetic fluctuations appear to compete with slightly incommensurate antiferromagnetic fluctuations and anomalous behavior such as logarithmic divergence of $C/T$ as well as $E/T$ scaling of total dynamic susceptibility observed near the QCP[161, 162] –similar to $CeCu_{6-x}Ag_x$ and $CeCu_{6-x}Au_x$. While it is not clear why the two fluctuations result in an $E/T$ scaling, it can be

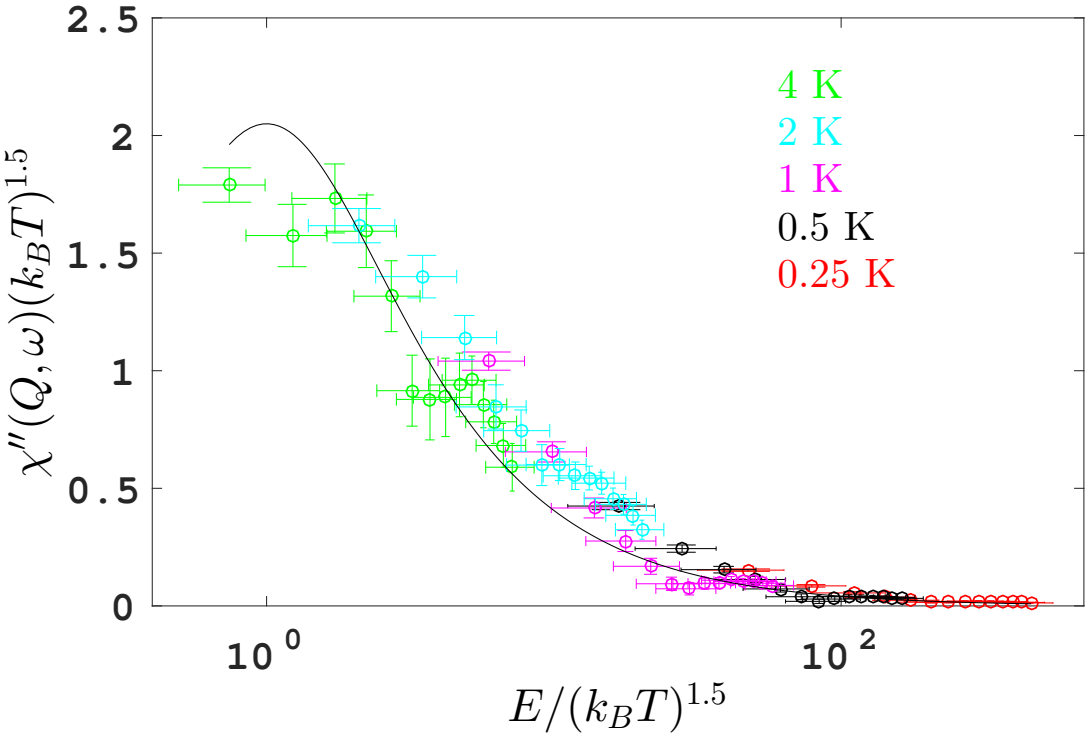



Figure 6.16: Scaling analysis of the critical dynamic susceptibility with reference to the conventional approach provided by HMM. The critical part of the dynamic susceptibility is extracted from the fit of a sum of two overlapping Lorentzians as shown in Fig. 6.13.

speculated that the frustration due to strongly competing ground states results in an unconventional scaling behavior. As is shown in Fig. 6.13, the spectral weights of the competing fluctuations in $CeCu_{5.8}Ag_{0.2}$ are roughly equal, showing that the ground states are nearly degenerate. Such degeneracy indicates a strong competition between two similar magnetic ground states; hence, the frustration resulting from the strong competition gives rise to an exotic nature of the QCP. This situation is somewhat similar to the geometrically frustrated systems in which the magnetic frustration gives rise to an $E/T$ scaling and a fractional exponent[163]. However, other possibilities can not be ruled out from the analysis; for instance, a quantum Lifshitz point arising from a large number of degenerate ground states (instead of two) can possibly lead to the unconventional behavior in $CeCu_{5.9}Au_{0.1}$.

## 6.4 Conclusions

In conclusion, an extensive series of INS measurements of $CeCu_{6-x}Ag_x$ at the critical composition was performed as a function of temperature, energy and momentum transfers. The dynamic susceptibility near the QCP displays $E/T$ scaling with an anomalous exponent of 0.72(1). The observed $E/T$ scaling is tantalizingly close to a number of different theoretical frameworks, although a simple phenomenological equation provides the best description, suggesting that the existing theoretical approaches are not sufficient to describe the quantum critical phenomenon. The analysis over a large area of the reciprocal space shows that the spectrum comprises of two competing magnetic fluctuations with similar spectral weights. The critical part of the fluctuations display $E/T^{3/2}$ scaling, demonstrating that some aspects of the critical behavior in $CeCu_{5.8}Ag_{0.2}$ is consistent with the conventional three dimensional antiferromagnetic QCP.

# Chapter 7

# Conclusions and Overview

This dissertation presents a thorough investigation of the structural and magnetic properties of $Ce\mathrm{Cu}_{6-x}T_x$ ($T$ = Ag, Pd) and $\mathrm{LaCu}_{6-x}\mathrm{Au}_x$. These series are closely related to the well-known heavy fermion series $\mathrm{CeCu}_{6-x}\mathrm{Au}_x$. Literature suggests that both $\mathrm{CeCu}_{6-x}\mathrm{Ag}_x$ and $\mathrm{CeCu}_{6-x}\mathrm{Pd}_x$ host a magnetic QCP and display similiar thermodynamic properties.

Using neutron and x-ray diffraction measurements, I have shown that there is a clear distinction in the doping dependence of the structural phase transition in $\mathrm{CeCu}_{6-x}\mathrm{Ag}_x$ and $\mathrm{CeCu}_{6-x}\mathrm{Pd}_x$ series. In $\mathrm{CeCu}_{6-x}\mathrm{Ag}_x$, the structural phase transition can be suppressed with Ag-composition, whereas in $\mathrm{CeCu}_{6-x}\mathrm{Pd}_x$, the structural phase transition remains unperturbed by Pd-substitution. Despite this distinction in the structural properties, the magnetic properties in these series are very similar. This suggests that the role of structural degrees of freedom is minimal in the evolution of long range magnetic order in these series.

The non-magnetic analogue $\mathrm{LaCu}_{6-x}\mathrm{Au}_x$ has shown the promise of hosting an elastic QCP – a fundamentally new type of quantum critical phenomena that has been theoretically predicted but never been experimentally realized. The elastic QCP paves a way to a new avenue of investigations into the expanded realm of QCPs that goes much beyond the scope of magnetic QCPs. Furthermore, DFT

calculations for $LaCu_6$ suggest that the role of electronic charge is minimal and is decoupled from the elastic properties. Hence, the $LaCu_{6-x}Au_x$ series appears to be particularly attractive for further investigations of purely elastic QCP. While the notion of the elastic QCP is still emerging, some of the topical questions that remain open are: How does the characteristics of an elastic QCP differ from the magnetic counterparts? Is there a room in Landau-Ginzburg-Wilson framework to describe the elastic QCPs? The answer of these questions will advance the understanding of the quantum critical phenomena.

INS measurements of the critical composition $CeCu_{5.8}Ag_{0.2}$ have provided novel insights into the $E/T$ scaling and the unconventional QCP. One interesting aspect of this investigation is that a simple phenomenological model describes the data in a superior way than the equations derived within the framework of available theoretical models. The superiority of the phenomenological equation suggests that an alternative to existing theoretical models is needed. Hence, a more rigorous approach in understanding the $E/T$ scaling is essential.

Our investigation offers additional insights into the longstanding puzzles in $CeCu_{6-x}Au_x$. An important result of this study is to unveil the presence of a commensurate magnetic fluctuation in addition to an incommensurate fluctuation. The overlap of these fluctuations give rise to a strange pattern of magnetic scattering, commonly referred as a "butterfly" in earlier studies. The fluctuations are three dimensional. A careful analysis of these fluctuations shows that only the incommensurate fluctuations appear to be critical at the QCP and are germane to the scaling analysis. When the critical part of the fluctuation is scaled, the dynamic susceptibility conforms to the predictions of a three dimensional SDW QCP. These observations demonstrate that the unconventional behavior is driven by competing fluctuations.

This analysis however leaves an interesting theoretical question as to why the $E/T$ scaling works well as it does. Probably, the easiest interpretation of this observation is that a fortuitous overlap of two competing fluctuations results in an

$E/T$ scaling. However, there are other possibilities that can not be ruled out from this analysis. For example, there can be a continuous change in the critical wave-vectors that give rise to a quantum Lifshitz point. The next prominent possibility is that the $E/T$ arises from a strong competition of nearly degenerate fluctuations or the inherent disorder in the system. Further studies to illuminate the role of additional magnetic fluctuations in the exotic character of $CeCu_{6-x}Au_x$ and $CeCu_{6-x}Ag_x$ would be beneficial in the overall understanding of quantum critical phenomena.

# Bibliography

[1] H. v. Löhneysen, A. Rosch, M. Vojta, and P. Wölfle, "Fermi-liquid instabilities at magnetic quantum phase transitions," *Rev. Mod. Phys.*, vol. 79, pp. 1015–1075, Aug 2007. xii, 2, 11, 12, 82, 83

[2] M. Klanjšek, "Viewpoint: A critical test of quantum criticality," *Physics*, vol. 7, p. 74, 2014. xiv, 6

[3] S. M. X. L. H. Y. Ye Chen, Zongfa Weng, "High-pressure studies on heavy fermion systems," *Chinese Physics B*, vol. 25, no. 7, p. 77401, 2016. xiv, 12

[4] A. C. Larson and D. T. Cromer, "The crystal structure of $CeCu_6$," *Acta Crystallogr.*, vol. 14, pp. 545–546, May 1961. xiv, 14, 15, 60

[5] R. Robinson, D. Goossens, M. Torikachvili, K. Kakurai, and H. Okumura, "A quantum multi-critical point in $CeCu_{6-x}Au_x$," *Physica B: Condensed Matter*, vol. 385-386, Part 1, pp. 38 – 40, 2006. xv, 18, 19, 53, 56, 66, 78

[6] H. Okumura, K. Kakurai, Y. Yoshida, Y. Ōnuki, and Y. Endoh, "Magnetic structure of $CeCu_{6-x}Au_x$," *J. Magn. Magn. Mater.*, vol. 177–181, Part 1, no. 0, pp. 405 – 406, 1998. xv, 17, 19, 76, 78

[7] K. Grube, W. H. Fietz, U. Tutsch, O. Stockert, and H. v. Löhneysen, "Suppression of the structural phase transition in $CeCu_6$ by pressure and Au doping," *Phys. Rev. B*, vol. 60, pp. 11947–11953, Nov 1999. xv, 18, 19, 53, 66, 83, 86, 89, 106

[8] O. Stockert, A. Schröder, H. Löhneysen, N. Pyka, E. Garcia-Matres, R. Kamp, S. Welzel, and M. Loewenhaupt, "Evolution of the magnetic order in $CeCu_{6-x}Au_x$," *Physica B: Condensed Matter*, vol. 259–261, no. 0, pp. 383 – 384, 1999. xv, 17, 19, 78

[9] H. Löhneysen, H. Bartolf, S. Drotziger, C. Pfleiderer, O. Stockert, D. Souptel, W. Löser, and G. Behr, "Rare-earth intermetallic compounds at a magnetic

instability," *Journal of Alloys and Compounds*, vol. 408-412, pp. 9 – 15, 2006. xv, 16, 18, 21, 22, 53, 76, 77

[10] E.-W. Scheidt, D. Maurer, A. Weber, T. Gotzfried, K. Heuser, S. Kehrein, and R. Tidecks, "Quantum phase transitions: experimental facts — a challenge for theory," *Physica B: Condensed Matter*, vol. 321, no. 1–4, pp. 133 – 137, 2002. Proceedings of the Second Regional Conference on Magnetic and Superconducting Materials. xv, 3, 23, 24, 25

[11] G. Ehlers, A. A. Podlesnyak, J. L. Niedziela, E. B. Iverson, and P. E. Sokol, "The new cold neutron chopper spectrometer at the spallation neutron source: Design and performance," *Review of Scientific Instruments*, vol. 82, no. 8, 2011. xvi, 50, 113

[12] E.-W. Scheidt, T. Schreiner, K. Heuser, and G. Stewart, "Quantum critical behavior of magnetic field-dependent resistivity of $CeCu_{6-x}Ag_x$," *Physica B: Condensed Matter*, vol. 259, pp. 388–389, 1999. xvii, 25, 56, 65

[13] M. Sieck, C. Speck, M. Waffenschmidt, S. Mock, and H. Löhneysen, "Magnetization and specific heat of $CeCu_{6-x}M_x$, $(M = Ni, Pd, Pt)$," *Physica B: Condensed Matter*, vol. 223–224, no. 0, pp. 325 – 328, 1996. xvii, 3, 23, 56, 65, 75, 76, 78

[14] R. Küchler, P. Gegenwart, K. Heuser, E.-W. Scheidt, G. R. Stewart, and F. Steglich, "Grüneisen ratio divergence at the quantum critical point in $CeCu_{6-x}Ag_x$," *Phys. Rev. Lett.*, vol. 93, p. 096402, Aug 2004. xxii, 25, 56, 75, 76, 78, 111, 112

[15] L. D. Landau, "On the theory of phase transitions," *Zh. Eksp. Teor. Fiz.*, vol. 11, p. 19, 1937. 1

[16] K. G. Wilson, "The renormalization group and critical phenomena," *Rev. Mod. Phys.*, vol. 55, pp. 583–600, Jul 1983. 2

[17] J. A. Hertz, "Quantum critical phenomena," *Phys. Rev. B*, vol. 14, pp. 1165–1184, Aug 1976. 2, 11

[18] A. J. Millis, "Effect of a nonzero temperature on quantum critical points in itinerant fermion systems," *Phys. Rev. B*, vol. 48, pp. 7183–7196, Sep 1993. 2, 11

[19] L. B. Ioffe and A. J. Millis, "Critical behavior of the uniform susceptibility of a fermi liquid near an antiferromagnetic transition with dynamic exponent z=2," *Phys. Rev. B*, vol. 51, pp. 16151–16158, Jun 1995. 2, 11

[20] A. J. Millis, D. K. Morr, and J. Schmalian, "Local defect in metallic quantum critical systems," *Phys. Rev. Lett.*, vol. 87, p. 167202, Oct 2001. 2

[21] T. Moriya, *Spin fluctuations in itinerant electron magnetism*, vol. 56. Springer-Verlag Berlin, 1985. 2, 11

[22] T. Moriya and T. Takimoto, "Anomalous properties around magnetic instability in heavy electron systems," *Journal of the Physical Society of Japan*, vol. 64, no. 3, pp. 960–969, 1995. 2, 11

[23] P. Gegenwart, Q. Si, and F. Steglich, "Quantum criticality in heavy-fermion metals," *Nat Phys*, vol. 4, pp. 186–197, Mar 2008. 2, 14, 53

[24] A. Schröder, G. Aeppli, R. Coldea, M. Adams, O. Stockert, H. Löhneysen, E. Bucher, R. Ramazashvili, and P. Coleman, "Onset of antiferromagnetism in heavy-fermion metals," *Nature*, vol. 407, no. 6802, pp. 351–355, 2000. 2, 14, 20, 53, 77, 83, 118

[25] A. Schröder, G. Aeppli, E. Bucher, R. Ramazashvili, and P. Coleman, "Scaling of magnetic fluctuations near a quantum phase transition," *Phys. Rev. Lett.*, vol. 80, pp. 5623–5626, Jun 1998. 2, 14, 20, 53, 83

[26] T. Senthil, A. Vishwanath, L. Balents, S. Sachdev, and M. P. Fisher, "Deconfined quantum critical points," *Science*, vol. 303, no. 5663, pp. 1490–1494, 2004. 5

[27] S. Sebastian, N. Harrison, C. Batista, L. Balicas, M. Jaime, P. Sharma, N. Kawashima, and I. Fisher, "Dimensional reduction at a quantum critical point," *Nature*, vol. 441, no. 7093, pp. 617–620, 2006. 5

[28] C. Rüegg, B. Normand, M. Matsumoto, A. Furrer, D. F. McMorrow, K. W. Krämer, H. U. Güdel, S. N. Gvasaliya, H. Mutka, and M. Boehm, "Quantum magnets under pressure: Controlling elementary excitations in $TiCuCl_3$," *Phys. Rev. Lett.*, vol. 100, p. 205701, May 2008. 5, 82

[29] S. Nakatsuji, K. Kuga, Y. Machida, T. Tayama, T. Sakakibara, Y. Karaki, H. Ishimoto, S. Yonezawa, Y. Maeno, E. Pearson, *et al.*, "Superconductivity and quantum criticality in the heavy-fermion system $\beta - YbAlB_4$," *Nature physics*, vol. 4, no. 8, pp. 603–607, 2008. 7, 82

[30] C. Petrovic, P. G. Pagliuso, M. F. Hundley, R. Movshovich, J. L. Sarrao, J. D. Thompson, Z. Fisk, and P. Monthoux, "Heavy-fermion superconductivity in $CeCoIn_5$ at 2.3 k," *Journal of Physics: Condensed Matter*, vol. 13, no. 17, p. L337, 2001. 7

[31] S. Jiang, H. Xing, G. Xuan, C. Wang, Z. Ren, C. Feng, J. Dai, Z. Xu, and G. Cao, "Superconductivity up to 30Kin the vicinity of the quantum critical point in $BaFe_2(As_{1-x}P_x)_2$," *Journal of Physics: Condensed Matter*, vol. 21, no. 38, p. 382203, 2009. 7

[32] T. Valla, A. V. Fedorov, P. D. Johnson, B. O. Wells, S. L. Hulbert, Q. Li, G. D. Gu, and N. Koshizuka, "Evidence for quantum critical behavior in the optimally doped cuprate $Bi_2Sr_2CaCu_2O_{8+\delta}$," *Science*, vol. 285, no. 5436, pp. 2110–2113, 1999. 7

[33] T. Shibauchi, A. Carrington, and Y. Matsuda, "A quantum critical point lying beneath the superconducting dome in iron pnictides," *Annu. Rev. Condens. Matter Phys.*, vol. 5, no. 1, pp. 113–135, 2014. 7

[34] L. Zhu, M. Garst, A. Rosch, and Q. Si, "Universally diverging grüneisen parameter and the magnetocaloric effect close to quantum critical points," *Phys. Rev. Lett.*, vol. 91, p. 066404, Aug 2003. 7

[35] J. Kondo, "Resistance minimum in dilute magnetic alloys," *Progress of Theoretical Physics*, vol. 32, no. 1, pp. 37–49, 1964. 9

[36] S. Doniach, "The Kondo lattice and weak antiferromagnetism," *Physica B+C*, vol. 91, pp. 231 – 234, 1977. 10

[37] S. Doniach, *Phase Diagram of the* Kondo *Lattice*, pp. 179–185. Boston, MA: Springer US, 1987. 10

[38] P. Coleman, C. Pépin, Q. Si, and R. Ramazashvili, "How do fermi liquids get heavy and die?," *Journal of Physics: Condensed Matter*, vol. 13, no. 35, p. R723, 2001. 13, 53

[39] R. Küchler, N. Oeschler, P. Gegenwart, T. Cichorek, K. Neumaier, O. Tegus, C. Geibel, J. A. Mydosh, F. Steglich, L. Zhu, and Q. Si, "Divergence of the grüneisen ratio at quantum critical points in heavy fermion metals," *Phys. Rev. Lett.*, vol. 91, p. 066405, Aug 2003. 14

[40] M. Nicklas, M. Brando, G. Knebel, F. Mayr, W. Trinkl, and A. Loidl, "Non-fermi-liquid behavior at a ferromagnetic quantum critical point in $Ni_xPd_{1-x}$," *Phys. Rev. Lett.*, vol. 82, pp. 4268–4271, May 1999. 14

[41] D. K. Singh, A. Thamizhavel, J. W. Lynn, S. Dhar, J. Rodriguez-Rivera, and T. Herman, "Field-induced quantum fluctuations in the heavy fermion superconductor cecu2ge2," *Scientific Reports*, vol. 1, pp. 117 EP –, Oct 2011. Article. 14

[42] T. Suzuki, T. Goto, A. Tamaki, T. Fujimura, Y. Ōnuki, and T. Komatsubara, "Elastic soft mode and crystalline field effect of Kondo lattice substance: $CeCu_6$," *J. Phys. Soc. Jpn.*, vol. 54, no. 7, pp. 2367–2370, 1985. 14, 18, 53, 66, 83

[43] K. Yamada, I. Hirosawa, Y. Noda, Y. Endoh, Y. Ōnuki, and T. Komatsubara, "Neutron scattering studies on structural phase transition in $CeCu_6$and $LaCu_{6-x}$," *J. Phys. Soc. Jpn.*, vol. 56, no. 10, pp. 3553–3557, 1987. 14, 18, 66, 83, 100

[44] Y. Ōnuki, Y. Shimizu, and T. Komatsubara, "Magnetic property of a new Kondo lattice intermetallic compound: $CeCu_6$," *Journal of the Physical Society of Japan*, vol. 53, no. 4, pp. 1210–1213, 1984. 14, 16

[45] G. R. Stewart, Z. Fisk, and M. S. Wire, "New Ce heavy-fermion system: $CeCu_6$," *Phys. Rev. B*, vol. 30, pp. 482–484, Jul 1984. 14, 16

[46] A. Amato, D. Jaccard, J. Flouquet, F. Lapierre, J. Tholence, R. Fisher, S. Lacy, J. Olsen, and N. Phillips, "Thermodynamic and transport properties of $CeCu_6$," *J. Low Temp. Phys.*, vol. 68, no. 5-6, pp. 371–397, 1987. 16, 17

[47] J. Rossat-Mignod, L. Regnault, J. Jacoud, C. Vettier, P. Lejay, J. Flouquet, E. Walker, D. Jaccard, and A. Amato, "Inelastic neutron scattering study of cerium heavy fermion compounds," *Journal of Magnetism and Magnetic Materials*, vol. 76, pp. 376 – 384, 1988. 16, 135

[48] L. Regnault, W. Erkelens, J. Rossat-Mignod, J. Flouquet, E. Walker, D. Jaccard, A. Amato, and B. Hennion, "A neutron scattering study of magnetic excitations in the heavy fermion compound $CeCu_6$," *Journal of Magnetism and Magnetic Materials*, vol. 63, pp. 289 – 292, 1987. 16, 135

[49] Regnault, L. P., Erkelens, W. A. C., Rossat-Mignod, J., Jacoud, J. L., Flouquet, J., Mignot, J. M., Walker, E., Jaccard, D., Amato, A., and Vettier, C.,

"Temperature and magnetic field dependence of magnetic correlations in the heavy fermion compound $CeCu_6$," *J. Phys. Colloques*, vol. 49, pp. C8–773–C8–774, 1988. 16

[50] Y. Ōnuki, Y. Shimizu, and T. Komatsubara, "Anisotropic magnetic property of Kondo lattice substance: $CeCu_6$," *Journal of the Physical Society of Japan*, vol. 54, no. 1, pp. 304–311, 1985. 16, 17

[51] A. Amato, D. Jaccard, E. Walker, and J. Flouquet, "Transport properties of $CeCu_6$ single crystals," *Solid State Communications*, vol. 55, no. 12, pp. 1131 – 1133, 1985. 17

[52] H. von Löhneysen, A. Neubert, T. Pietrus, A. Schröder, O. Stockert, U. Tutsch, M. Loewenhaupt, A. Rosch, and P. Wölfle, "Magnetic order and transport in the heavy-fermion system $CeCu_{6-x}Au_x$," *The European Physical Journal B – Condensed Matter and Complex Systems*, vol. 5, no. 3, pp. 447–455, 1998. 17, 75, 78

[53] H. Löhneysen, A. Schröder, and O. Stockert, "Magnetic fluctuations in $CeCu_{6-x}Au_x$ at the nonmangetic-magnetic quantum phase transition," *Solid State Commun.*, vol. 303–304, no. 0, pp. 480 – 488, 2000. 17, 78

[54] O. Stockert, H. Löhneysen, A. Rosch, N. Pyka, and M. Loewenhaupt, "Spin dynamics at the magnetic instability in $CeCu_{6-x}Au_x$," *Physica B: Condensed Matter*, vol. 259–261, no. 0, pp. 376 – 377, 1999. 17, 20, 53, 75, 76, 78

[55] O. Stockert, H. v. Löhneysen, W. Schmidt, M. Enderle, and M. Loewenhaupt, "Quantum criticality and scaling of the magnetic response in $CeCu_{6-x}Au_x$," *J. of Low Temp. Phys.*, vol. 161, no. 1-2, pp. 55–66, 2010. 17, 78

[56] H. Löhneysen, C. Pfleiderer, A. Schröder, and O. Stockert, "New results for quantum critical behavior in strongly correlated electron systems," *J. Phys. Chem. Solids*, vol. 63, no. 12, pp. 2155 – 2162, 2002. 17, 78

[57] O. Stockert, H. Löhneysen, A. Schröder, M. Loewenhaupt, N. Pyka, P. Gammel, and U. Yaron, "Incommensurate antiferromagnetism and magnetic correlations in $CeCu_{6-x}Au_x$," *Physica B: Condensed Matter : Condensed Matter*, vol. 230–232, no. 0, pp. 247 – 249, 1997. 17, 76, 78

[58] O. Stockert, A. Neubert, and H. Löhneysen, "Magnetic ordering of the heavy-fermion alloy $CeCu_{5.1}Ag_{0.9}$," *Physica B: Condensed Matter*, vol. 230–232, pp. 250 – 252, 1997. 17, 78

[59] A. Hamann, O. Stockert, V. Fritsch, K. Grube, A. Schneidewind, and H. v. Löhneysen, "Evolution of the magnetic structure in $CeCu_{5.5}Au_{0.5}$ under pressure towards quantum criticality," *Phys. Rev. Lett.*, vol. 110, p. 096404, Feb 2013. 17, 75

[60] M. Ruck, G. Portisch, H. G. Schlager, M. Sieck, and H. v. Löhneysen, "Structure and electrical resistivity of the heavy fermion compound $CeCu_5Au$," *Acta Crystallogr. Sect. B*, vol. 49, pp. 936–941, Dec 1993. 17, 60, 61, 89

[61] H. Asano, M. Umino, Y. Ōnuki, T. Komatsubara, F. Izumi, and N. Watanabe, "Neutron diffraction study on the low-temperature monoclinic form of $PrCu_6$," *J. Phys. Soc. Jpn.*, vol. 56, no. 7, pp. 2245–2247, 1987. 18, 83

[62] M. Nakazato, N. Wakabayashi, and Y. Ōnuki, "Structural studies on $RCu_6$ (R = Pr, Nd *and* Sm) at low temperatures," *J. Phys. Soc. Jpn.*, vol. 59, no. 11, pp. 4004–4009, 1990. 18, 83

[63] O. Stockert, H. v. Löhneysen, A. Rosch, N. Pyka, and M. Loewenhaupt, "Two-dimensional fluctuations at the quantum-critical point of $CeCu_{6-x}Au_x$," *Phys. Rev. Lett.*, vol. 80, pp. 5627–5630, Jun 1998. 20, 83, 129

[64] O. Stockert, M. Enderle, and H. v. Löhneysen, "Magnetic fluctuations at a field-induced quantum phase transition," *Phys. Rev. Lett.*, vol. 99, p. 237203, Dec 2007. 20

[65] H. Löhneysen, O. Stockert, and M. Enderle, "Magnetic fluctuations at the field-tuned vs. concentration-tuned quantum phase transition in $CeCu_{6-x}Au_x$," *Journal of Magnetism and Magnetic Materials*, vol. 310, no. 2, Part 1, pp. 822 – 827, 2007. 20, 53

[66] H. v. Löhneysen, C. Pfleiderer, T. Pietrus, O. Stockert, and B. Will, "Pressure versus magnetic-field tuning of a magnetic quantum phase transition," *Phys. Rev. B*, vol. 63, p. 134411, Mar 2001. 20

[67] O. Isnard, J. Pierre, D. Fruchart, L. Romaka, and R. Skolozdra, "Crossover from Kondo lattice to antiferromagnetic ordering in the $CeCu_{6-x}Sn_x$ phase," *Solid State Commun.*, vol. 113, no. 6, pp. 335 – 340, 1999. 23, 56

[68] Q. Si, S. Rabello, K. Ingersent, and J. L. Smith, "Locally critical quantum phase transitions in strongly correlated metals," *Nature*, vol. 413, no. 6858, pp. 804–808, 2001. 25, 26, 27, 53

[69] Q. Si, S. Rabello, K. Ingersent, and J. L. Smith, "Local fluctuations in quantum critical metals," *Phys. Rev. B*, vol. 68, p. 115103, Sep 2003. 25, 26, 27, 110

[70] Q. Si, "The local quantum critical point and non-fermi liquid properties," *Journal of Physics: Condensed Matter*, vol. 15, no. 28, p. S2207, 2003. 26

[71] D. R. Grempel and Q. Si, "Locally critical point in an anisotropic Kondo lattice," *Phys. Rev. Lett.*, vol. 91, p. 026401, Jul 2003. 26, 121

[72] J.-X. Zhu, S. Kirchner, R. Bulla, and Q. Si, "Zero-temperature magnetic transition in an easy-axis Kondo lattice model," *Phys. Rev. Lett.*, vol. 99, p. 227204, Nov 2007. 26, 121

[73] M. T. Glossop and K. Ingersent, "Magnetic quantum phase transition in an anisotropic Kondo lattice," *Phys. Rev. Lett.*, vol. 99, p. 227203, Nov 2007. 26, 121

[74] E. Abrahams, J. Schmalian, and P. Wölfle, "Strong-coupling theory of heavy-fermion criticality," *Phys. Rev. B*, vol. 90, p. 045105, Jul 2014. 28

[75] E. Abrahams and P. Wölfle, "Critical quasiparticle theory applied to heavy fermion metals near an antiferromagnetic quantum phase transition," *Proceedings of the National Academy of Sciences*, vol. 109, no. 9, pp. 3238–3242, 2012. 28, 110

[76] C. M. Varma, "Quantum criticality in quasi-two-dimensional itinerant antiferromagnets," *Phys. Rev. Lett.*, vol. 115, p. 186405, Oct 2015. 29, 110

[77] V. Aji and C. M. Varma, "Topological excitations near the local critical point in the dissipative two-dimensional $xy$ model," *Phys. Rev. B*, vol. 82, p. 174501, Nov 2010. 29

[78] L. Zhu, Y. Chen, and C. M. Varma, "Local quantum criticality in the two-dimensional dissipative quantum xy model," *Phys. Rev. B*, vol. 91, p. 205129, May 2015. 29, 110

[79] J. Czochralski, "A new method for the measurement of the crystallization rate of metals," *Zeitschrift für physikalische Chemie*, vol. 92, pp. 219–221, 1918. 32

[80] G. Shirane, S. M. Shapiro, and J. M. Tranquada, *Neutron Scattering with a Triple-Axis Spectrometer*. Cambridge university press, 2002. 38

[81] G. L. Squires, *Introduction to the theory of thermal neutron scattering*. Cambridge university press, 2012. 38, 40, 42, 43

[82] A.-J. Dianoux and G. Lander, *Neutron data booklet*. OCPscience, 2003. 38

[83] M. F. Collins, *Magnetic critical scattering*. Oxford University Press, 1989. 38

[84] T. Chatterji, *Neutron scattering from magnetic materials*. Gulf Professional Publishing, 2005. 38

[85] L. Van Hove, "Correlations in space and time and born approximation scattering in systems of interacting particles," *Phys. Rev.*, vol. 95, pp. 249–262, Jul 1954. 41

[86] L. Poudel, C. de la Cruz, E. A. Payzant, A. F. May, M. Koehler, V. O. Garlea, A. E. Taylor, D. S. Parker, H. B. Cao, M. A. McGuire, W. Tian, M. Matsuda, H. Jeen, H. N. Lee, T. Hong, S. Calder, H. D. Zhou, M. D. Lumsden, V. Keppens, D. Mandrus, and A. D. Christianson, "Structural and magnetic phase transitions in $CeCu_{6-x}T_x$ ($t = ag, pd$)," *Phys. Rev. B*, vol. 92, p. 214421, Dec 2015. 52, 89, 128, 135

[87] S. Friedemann, N. Oeschler, S. Wirth, C. Krellner, C. Geibel, F. Steglich, S. Paschen, S. Kirchner, and Q. Si, "Fermi-surface collapse and dynamical scaling near a quantum-critical point," *Proc. Natl. Acad. Sci. U.S.A.*, vol. 107, no. 33, pp. 14547–14551, 2010. 53

[88] M. C. Aronson, R. Osborn, R. A. Robinson, J. W. Lynn, R. Chau, C. L. Seaman, and M. B. Maple, "Non-fermi-liquid scaling of the magnetic response in $UCu_{5-x}Pd_x$ ($x = 1, 1.5$)," *Phys. Rev. Lett.*, vol. 75, pp. 725–728, Jul 1995. 53

[89] P. Coleman, "Heavy fermions: Dimensions are critical," *Nature materials*, vol. 11, no. 3, pp. 185–187, 2012. 53

[90] S. Paschen, T. Lühmann, S. Wirth, P. Gegenwart, O. Trovarelli, C. Geibel, F. Steglich, P. Coleman, and Q. Si, "Hall-effect evolution across a heavy-fermion quantum critical point," *Nature*, vol. 432, no. 7019, pp. 881–885, 2004. 53

[91] L. Jiao, Y. Chen, Y. Kohama, D. Graf, E. D. Bauer, J. Singleton, J.-X. Zhu, Z. Weng, G. Pang, T. Shang, J. Zhang, H.-O. Lee, T. Park, M. Jaime, J. D. Thompson, F. Steglich, Q. Si, and H. Q. Yuan, "Fermi surface reconstruction and multiple quantum phase transitions in the antiferromagnet $CeRhIn_5$," *Proc. Natl. Acad. Sci. U.S.A.*, vol. 112, no. 3, pp. 673–678, 2015. 53

[92] M. Vrtis, J. Jorgensen, and D. Hinks, "Structural phase transition in $CeCu_6$," *Physica B+C*, vol. 136, no. 1âĂŞ3, pp. 489 – 492, 1986. 53, 66

[93] T. Goto, T. Suzuki, A. Tamaki, T. Fujimura, Y. Ōnuki, and T. Komatsubara, "Elastic properties of the Kondo lattice compound $CeCu_6$," *J. Magn. Magn. Mater.*, vol. 63–64, pp. 309–311, 1987. 53, 79

[94] H. Löhneysen, A. Germann, and A. Schröder, "Volume dependence of magnetic ordering in $CeCu_{6-x}Au_x$ heavy fermion alloys," *Physica B: Condensed Matter*, vol. 163, no. 1-3, pp. 144 – 146, 1990. 53

[95] G. Fraunberger, B. Andraka, J. S. Kim, U. Ahlheim, and G. R. Stewart, "Magnetic behavior of $CeCu_{6-x}Ag_x$," *Phys. Rev. B*, vol. 40, pp. 4735–4739, Sep 1989. 56, 75, 76

[96] A. Germann, A. Nigam, J. Dutzi, A. Schröder, and H. v. Löhneysen, "Magnetic ordering in the heavy-fermion alloys $CeCu_{6-x}Au_x$ and $CeCu_{6-x}Au_x$," *Le Journal de Physique Colloques*, vol. 49, no. C8, pp. C8–755, 1988. 56

[97] A. K. Gangopadhyay, J. S. Schilling, E. Schuberth, P. Gutsmiedl, F. Gross, and K. Andres, "Incipient magnetic order in $CeCu_6$," *Phys. Rev. B*, vol. 38, pp. 2603–2607, Aug 1988. 56

[98] K. Heuser, E.-W. Scheidt, T. Schreiner, and G. R. Stewart, "Inducement of non-fermi-liquid behavior with a magnetic field," *Phys. Rev. B*, vol. 57, pp. R4198–R4201, Feb 1998. 56

[99] J. Rodríguez-Carvajal, "Recent advances in magnetic structure determination by neutron powder diffraction," *Physica B: Condensed Matter*, vol. 192, no. 1-2, pp. 55 – 69, 1993. 59, 86

[100] A. Wills, "A new protocol for the determination of magnetic structures using simulated annealing and representational analysis (sarah)," *Physica B: Condensed Matter*, vol. 276–278, no. 0, pp. 680 – 681, 2000. 59

[101] S. Mock, C. Paschke, A. Schröder, J. Sereni, M. Sieck, and H. Löhneysen, "Magnetic and thermodynamic properties $CeCu_{6-x}Au_x$ for $0 \leq x \leq 2$," *Physica B: Condensed Matter*, vol. 199, pp. 39–41, 1994. 61

[102] P. Blaha, K. Schwarz, G. K. H. Madsen, D. Kvasnicka, and J. Luitz, *WIEN2K, An Augmented Plane Wave + Local Orbitals Program for Calculating Crystal Properties*. Karlheinz Schwarz, Techn. Universität Wien, Austria, 2001. 66, 86

[103] J. P. Perdew, K. Burke, and M. Ernzerhof, "Generalized gradient approximation made simple," *Phys. Rev. Lett.*, vol. 77, pp. 3865–3868, Oct 1996. 66, 86

[104] H. Asano, M. Umino, Y. Hataoka, Y. Shimizu, Y. Ōnuki, T. Komatsubara, and F. Izumi, "The crystal structure of $LaCu_6$," *J. Phys. Soc. Jpn.*, vol. 54, no. 9, pp. 3358–3361, 1985. 70

[105] G. R. Stewart, "Heavy-fermion systems," *Rev. Mod. Phys.*, vol. 56, pp. 755–787, Oct 1984. 71, 82

[106] J. H. Shim, K. Haule, and G. Kotliar, "Modeling the localized-to-itinerant electronic transition in the heavy fermion system $CeIrIn_5$," *Science*, vol. 318, no. 5856, pp. 1615–1617, 2007. 71

[107] K. Held, A. K. McMahan, and R. T. Scalettar, "Cerium volume collapse: Results from the merger of dynamical mean-field theory and local density approximation," *Phys. Rev. Lett.*, vol. 87, p. 276404, Dec 2001. 71

[108] M. B. Zölfl, I. A. Nekrasov, T. Pruschke, V. I. Anisimov, and J. Keller, "Spectral and magnetic properties of $\alpha$- and $\gamma-$Ce from dynamical mean-field theory and local density approximation," *Phys. Rev. Lett.*, vol. 87, p. 276403, Dec 2001. 71

[109] A. K. McMahan, K. Held, and R. T. Scalettar, "Thermodynamic and spectral properties of compressed ce calculated using a combined local-density approximation and dynamical mean-field theory," *Phys. Rev. B*, vol. 67, p. 075108, Feb 2003. 71

[110] K. Haule, V. Oudovenko, S. Y. Savrasov, and G. Kotliar, "The $\alpha \rightarrow \gamma$ transition in ce: A theoretical view from optical spectroscopy," *Phys. Rev. Lett.*, vol. 94, p. 036401, Jan 2005. 71

[111] A. Zheludev, *ResLib 3.4*. Oak Ridge National Laboratory, 2007. 72

[112] M. J. Cooper and R. Nathans, "The resolution function in neutron diffractometry. I. the resolution function of a neutron diffractometer and its application to phonon measurements," *Acta Crystallographica*, vol. 23, no. 3, pp. 357–367, 1967. 72

[113] J. M. Lawrence and S. M. Shapiro, "Magnetic ordering in the presence of fast spin fluctuations: A neutron scattering study of $CeIn_3$," *Phys. Rev. B*, vol. 22, pp. 4379–4388, Nov 1980. 75

[114] K. Heuser, E.-W. Scheidt, T. Schreiner, and G. R. Stewart, "Disappearance of hyperscaling at low temperatures in non-fermi-liquid $CeCu_{5.2}Ag_{0.8}$," *Phys. Rev. B*, vol. 58, pp. R15959–R15961, Dec 1998. 76

[115] H. Löhneysen, M. Sieck, O. Stockert, and M. Waffenschmidt, "Investigation of non-fermi-liquid behavior in $CeCu_{6-x}Au_x$," *Physica B: Condensed Matter*, vol. 223–224, no. 0, pp. 471 – 474, 1996. 78

[116] S. K. Goh, D. A. Tompsett, P. J. Saines, H. C. Chang, T. Matsumoto, M. Imai, K. Yoshimura, and F. M. Grosche, "Ambient pressure structural quantum critical point in the phase diagram of $(Sr,Ca)_3Rh_4Sn_{13}$," *Phys. Rev. Lett.*, vol. 114, p. 097002, Mar 2015. 79, 82, 107

[117] L. E. Klintberg, S. K. Goh, P. L. Alireza, P. J. Saines, D. A. Tompsett, P. W. Logg, J. Yang, B. Chen, K. Yoshimura, and F. M. Grosche, "Pressure- and composition-induced structural quantum phase transition in the cubic superconductor $(Sr,Ca)_3Ir_4Sn_{13}$," *Phys. Rev. Lett.*, vol. 109, p. 237008, Dec 2012. 79, 82, 107

[118] L. Poudel, A. F. May, M. R. Koehler, M. A. McGuire, S. Mukhopadhyay, S. Calder, R. E. Baumbach, R. Mukherjee, D. Sapkota, C. de la Cruz, D. J. Singh, D. Mandrus, and A. D. Christianson, "Candidate elastic quantum critical point in $LaCu_{6-x}Au_x$," *Phys. Rev. Lett.*, vol. 117, p. 235701, Nov 2016. 81

[119] T. Park, F. Ronning, H. Q. Yuan, M. B. Salamon, R. Movshovich, J. L. Sarrao, and J. D. Thompson, "Hidden magnetism and quantum criticality in the heavy fermion superconductor $CeRhIn_5$," *Nature*, vol. 440, pp. 65–68, Mar 2006. 82

[120] N. D. Mathur, F. M. Grosche, S. R. Julian, I. R. Walker, D. M. Freye, R. K. W. Haselwimmer, and G. G. Lonzarich, "Magnetically mediated superconductivity in heavy fermion compounds," *Nature*, vol. 394, pp. 39–43, Jul 1998. 82

[121] S. Sachdev, "Quantum criticality: Competing ground states in low dimensions," *Science*, vol. 288, no. 5465, pp. 475–480, 2000. 82, 110

[122] B. Lake, D. A. Tennant, and S. E. Nagler, "Novel longitudinal mode in the coupled quantum chain compound $KCuF_3$," *Phys. Rev. Lett.*, vol. 85, pp. 832–835, Jul 2000. 82

[123] M. Kenzelmann, Y. Chen, C. Broholm, D. H. Reich, and Y. Qiu, "Bound spinons in an antiferromagnetic $s = 1/2$ chain with a staggered field," *Phys. Rev. Lett.*, vol. 93, p. 017204, Jul 2004. 82

[124] R. Oppermann and H. Thomas, "Critical behaviour at the displacive limit of structural phase transitions," *Zeitschrift für Physik B Condensed Matter*, vol. 22, no. 4, pp. 387–396, 1975. 82

[125] R. Folk, H. Iro, and F. Schwabl, "Critical dynamics of elastic phase transitions," *Phys. Rev. B*, vol. 20, pp. 1229–1244, Aug 1979. 82

[126] T. Schneider, H. Beck, and E. Stoll, "Quantum effects in an $n$-component vector model for structural phase transitions," *Phys. Rev. B*, vol. 13, pp. 1123–1130, Feb 1976. 82

[127] Y. T. Millev and D. I. Uzunov, "Critical dynamics of zero-temperature structural phase transitions," *Journal of Physics C: Solid State Physics*, vol. 16, no. 21, p. 4107, 1983. 82

[128] J. F. Scott, "Soft-mode spectroscopy: Experimental studies of structural phase transitions," *Rev. Mod. Phys.*, vol. 46, pp. 83–128, Jan 1974. 82

[129] R. Morf, T. Schneider, and E. Stoll, "Nonuniversal critical behavior and its suppression by quantum fluctuations," *Phys. Rev. B*, vol. 16, pp. 462–469, Jul 1977. 82

[130] S. E. Rowley, L. J. Spalek, R. P. Smith, M. P. M. Dean, M. Itoh, J. F. Scott, G. G. Lonzarich, and S. S. Saxena, "Ferroelectric quantum criticality," *Nat Phys*, vol. 10, pp. 367–372, May 2014. Article. 82

[131] K. A. Müller and H. Burkard, "$SrTiO_3$: An intrinsic quantum paraelectric below 4 k," *Phys. Rev. B*, vol. 19, pp. 3593–3602, Apr 1979. 82

[132] E. L. Venturini, G. A. Samara, M. Itoh, and R. Wang, "Pressure as a probe of the physics of $^{18}O$ – substituted $SrTiO_3$," *Phys. Rev. B*, vol. 69, p. 184105, May 2004. 82

[133] S. U. Handunkanda, E. B. Curry, V. Voronov, A. H. Said, G. G. Guzmán-Verri, R. T. Brierley, P. B. Littlewood, and J. N. Hancock, "Large isotropic negative thermal expansion above a structural quantum phase transition," *Phys. Rev. B*, vol. 92, p. 134101, Oct 2015. 82

[134] W. C. Yu, Y. W. Cheung, P. J. Saines, M. Imai, T. Matsumoto, C. Michioka, K. Yoshimura, and S. K. Goh, "Strong coupling superconductivity in the

vicinity of the structural quantum critical point in $(Sr,Ca)_3Rh_4Sn_{13}$," *Phys. Rev. Lett.*, vol. 115, p. 207003, Nov 2015. 82, 107, 110

[135] P. K. Biswas, Z. Guguchia, R. Khasanov, M. Chinotti, L. Li, K. Wang, C. Petrovic, and E. Morenzoni, "Strong enhancement of *s*-wave superconductivity near a quantum critical point of $(Ca)_3Ir_4Sn_{13}$," *Phys. Rev. B*, vol. 92, p. 195122, Nov 2015. 82, 107

[136] C. N. Kuo, C. W. Tseng, C. M. Wang, C. Y. Wang, Y. R. Chen, L. M. Wang, C. F. Lin, K. K. Wu, Y. K. Kuo, and C. S. Lue, "Lattice distortion associated with fermi-surface reconstruction in $(Sr)_3Rh_4Sn_{13}$," *Phys. Rev. B*, vol. 91, p. 165141, Apr 2015. 82, 107

[137] C. N. Kuo, H. F. Liu, C. S. Lue, L. M. Wang, C. C. Chen, and Y. K. Kuo, "Characteristics of the phase transition near 147Kin $(Sr)_3Rh_4Sn_{13}$," *Phys. Rev. B*, vol. 89, p. 094520, Mar 2014. 82, 107

[138] A. F. Fang, X. B. Wang, P. Zheng, and N. L. Wang, "Unconventional charge-density wave in $(Sr)_3Ir_4Sn_{13}$ cubic superconductor revealed by optical spectroscopy study," *Phys. Rev. B*, vol. 90, p. 035115, Jul 2014. 82, 107

[139] C. Fang, H. Yao, W.-F. Tsai, J. Hu, and S. A. Kivelson, "Theory of electron nematic order in LaFeAsO," *Phys. Rev. B*, vol. 77, p. 224509, Jun 2008. 82, 105

[140] C. Xu, M. Müller, and S. Sachdev, "Ising and spin orders in the iron-based superconductors," *Phys. Rev. B*, vol. 78, p. 020501, Jul 2008. 82, 105

[141] E. Fradkin and S. A. Kivelson, "Electron nematic phases proliferate," *Science*, vol. 327, no. 5962, pp. 155–156, 2010. 82, 105

[142] M. Zacharias, I. Paul, and M. Garst, "Quantum critical elasticity," *Phys. Rev. Lett.*, vol. 115, p. 025703, Jul 2015. 83

[143] E. Brück, A. Nowack, N. Hohn, E. Paulus, and A. Freimuth, "Transport properties and point-contact spectra of $ReCu_6$ with re = la, ce, pr," *Z. Phys. B - Cond. Mat.*, vol. 63, no. 2, pp. 155–162, 1986. 83

[144] A. Togo and I. Tanaka, "First principles phonon calculations in materials science," *Scripta Materialia*, vol. 108, pp. 1 – 5, 2015. 86

[145] P. E. Blöchl, "Projector augmented-wave method," *Phys. Rev. B*, vol. 50, pp. 17953–17979, Dec 1994. 86

[146] G. Kresse and D. Joubert, "From ultrasoft pseudopotentials to the projector augmented-wave method," *Phys. Rev. B*, vol. 59, pp. 1758–1775, Jan 1999. 86

[147] D. J. Singh and L. Nordstrom, *Planewaves, Pseudopotentials, and the LAPW method*. Springer Science & Business Media, 2006. 86

[148] M. A. Carpenter, E. K. Salje, and A. Graeme-Barber, "Spontaneous strain as a determinant of thermodynamic properties for phase transitions in minerals," *Eur. J. Mineral*, vol. 10, pp. 621–691, 07 1998. 88

[149] C. Kittel, *Introduction to solid state physics*. Wiley, 2005. 96

[150] T. Herrmannsdörfer, F. Pobell, J. Sebek, and P. Svoboda, "Superconductivity in $LaCu_6$ and possible applications," *Physica C: Superconductivity*, vol. 388, pp. 565–566, 2003. 96

[151] E. K. Salje, "Ferroelastic materials," *Annu. Rev. Mater. Res.*, vol. 42, no. 1, pp. 265–283, 2012. 100

[152] H. Harima, A. Yanase, and A. Hasegawa, "Electronic structure and fermi surface of $LaCu_6$," *J. Phys. Soc. Jpn.*, vol. 59, no. 11, pp. 4054–4064, 1990. 100

[153] I. Pomeranchuk, "On the stability of a fermi liquid," *Sov. Phys. JETP*, vol. 8, p. 361, 1958. 105, 106

[154] D. C. Johnston, "The puzzle of high temperature superconductivity in layered iron pnictides and chalcogenides," *Advances in Physics*, vol. 59, no. 6, pp. 803–1061, 2010. 106

[155] G. K. Madsen and D. J. Singh, "Boltztrap. a code for calculating band-structure dependent quantities," *Computer Physics Communications*, vol. 175, no. 1, pp. 67 – 71, 2006. 106

[156] D. A. Tompsett, "Electronic structure and phonon instabilities in the vicinity of the quantum phase transition and superconductivity of $(Sr,Ca)_3Ir_4Sn_{13}$," *Phys. Rev. B*, vol. 89, p. 075117, Feb 2014. 107

[157] O. Arnold, J. Bilheux, J. Borreguero, A. Buts, S. Campbell, L. Chapon, M. Doucet, N. Draper, R. F. Leal, M. Gigg, V. Lynch, A. Markvardsen, D. Mikkelson, R. Mikkelson, R. Miller, K. Palmen, P. Parker, G. Passos, T. Perring, P. Peterson, S. Ren, M. Reuter, A. Savici, J. Taylor, R. Taylor, R. Tolchenov, W. Zhou, and J. Zikovsky, "Mantid-data analysis and visualization package for neutron scattering and {SR} experiments," *Nuclear Instruments and Methods in Physics Research Section A: Accelerators, Spectrometers, Detectors and Associated Equipment*, vol. 764, pp. 156 – 166, 2014. 113

[158] R. Ewings, A. Buts, M. Le, J. van Duijn, I. Bustinduy, and T. Perring, "Horace: Software for the analysis of data from single crystal spectroscopy experiments at time-of-flight neutron instruments," *Nuclear Instruments and Methods in Physics Research Section A: Accelerators, Spectrometers, Detectors and Associated Equipment*, vol. 834, pp. 132 – 142, 2016. 113

[159] R. T. Azuah, L. R. Kneller, Y. Qiu, P. L. Tregenna-Piggott, C. M. Brown, J. R. Copley, and R. M. Dimeo, "Dave: a comprehensive software suite for the reduction, visualization, and analysis of low energy neutron spectroscopic

data," *Journal of Research of the National Institute of Standards and Technology*, vol. 114, no. 6, p. 341, 2009. 113

[160] C. M. Varma, L. Zhu, and A. Schröder, "Quantum critical response function in quasi-two-dimensional itinerant antiferromagnets," *Phys. Rev. B*, vol. 92, p. 155150, Oct 2015. 128

[161] C. Stock, C. Broholm, F. Demmel, J. Van Duijn, J. W. Taylor, H. J. Kang, R. Hu, and C. Petrovic, "From incommensurate correlations to mesoscopic spin resonance in $YbRh_2Si_2$," *Phys. Rev. Lett.*, vol. 109, p. 127201, Sep 2012. 135

[162] P. Gegenwart, J. Custers, T. Tayama, K. Tenya, C. Geibel, O. Trovarelli, F. Steglich, and K. Neumaier, "Divergence of the heavy quasiparticle mass at the antiferromagnetic quantum critical point in $YbRh_2Si_2$," *Acta Physica Polonica. Series B*, vol. 34, no. 2, Part one, pp. 323–334, 2003. 135

[163] J. S. Helton, K. Matan, M. P. Shores, E. A. Nytko, B. M. Bartlett, Y. Qiu, D. G. Nocera, and Y. S. Lee, "Dynamic scaling in the susceptibility of the spin-$\frac{1}{2}$ kagome lattice antiferromagnet herbertsmithite," *Phys. Rev. Lett.*, vol. 104, p. 147201, Apr 2010. 137

# Appendix

# List of Publications

- Candidate Elastic Quantum Critical Point in $LaCu_{6-x}Au_x$, **L. Poudel**, A. F. May, M. R. Koehler, M. A. McGuire, S. Mukhopadhyay, S. Calder, R. E. Baumbach, R. Mukherjee, D. Sapkota, C. de la Cruz, D. J. Singh, D. Mandrus, and A. D. Christianson, Phys. Rev. Lett. **117**, 235701(2016)

- Anisotropic Exchange within Decoupled Tetrahedra in the Quantum Breathing Pyrochlore $Ba_3Yb_2Zn_5O_{11}$, J. G. Rau, L. S. Wu, A. F. May, **L. Poudel**, B. Winn, V. O. Garlea, A. Huq, P. Whitfield, A. E. Taylor, M. D. Lumsden, M. J. P. Gingras, and A. D. Christianson, Phys. Rev. Lett. **116**, 257204(2016)

- Influence of interstitial Mn on magnetism in the room-temperature ferromagnet $Mn_{1+\delta}Sb$, A. E. Taylor, T. Berlijn, S. E. Hahn, A. F. May, T. J. Williams, **L. Poudel**, S. Calder, R. S. Fishman, M. B. Stone, A. A. Aczel, H. B. Cao, M. D. Lumsden, and A. D. Christianson Phys. Rev. B **91**, 224418 (2015)

- Structural and magnetic phase transitions in $CeCu_{6-x}T_x$ ($T = Ag, Pd$) ($T$ = Ag, Pd), **L. Poudel**, C. de la Cruz, A. E. Payzant, A. F. May, M. Koehler, O. V. Garlea, A. E. Taylor, D. S. Parker, H. B. Cao, M. A. McGuire, W. Tian, M. Matsuda, H. Jeen, H. N. Lee, T. Hong, S. Calder, H. D. Zhou, M. D. Lumsden, V. Keppens, D. Mandrus and A. D. Christianson, Phys. Rev. B **92**, 214421(2015)

- Spectroscopic evidence for strong quantum spin fluctuations with itinerant character in $YFe_2Ge_2$, N. Sirica, F. Bondino, S. Nappini, I. Píš, **L. Poudel**, A.

D. Christianson, D. Mandrus, D. J. Singh, and N. Mannella, Phys. Rev. B **91**, 121102(R) (2015)

- Quantum critical fluctuations in the heavy fermion compound $Ce(Ni_{0.935}Pd_{0.065})_2Ge_2$, C. H. Wang, **L. Poudel**, A. E. Taylor, J. M. Lawrence, A. D. Christianson, S. Chang, J. A. Rodriguez-Rivera, J. W. Lynn, A. A. Podlesnyak, G. Ehlers, R. E. Baumbach, E. D. Bauer, K. Gofryk, F. Ronning, K. J. McClellan and J. D. Thompson, J. Phys. Condens. Matter, **27**, 015602(2015)

- Magnetism and electronic structure of $La_2ZnIrO_6$ and $La_2MgIrO_6$: Candidate $J_{\text{eff}} = \frac{1}{2}$ Mott insulators, Guixin Cao, Alaska Subedi, S. Calder, J.-Q. Yan, Jieyu Yi, Zheng Gai, **Lekhanath Poudel**, David J. Singh, Mark D. Lumsden, A. D. Christianson, Brian C. Sales, and David Mandrus, Phys. Rev. B **87**, 155136 (2013)

# Vita

Lekh was born in a small town in Nepal called Itahari. He started his school at Amarpur higher secondary school located at Amarpur, Pachthar, Nepal. He graduated from Vishwa Adarsha Higher Secondary School, Itahari in 2002. He completed Bachelor and Masters degree in physics from Tribhuvan University, Kathmandu, Nepal. Before and after his graduation, he served as a high school teacher in several places in Nepal. He joined the University of Tennessee, Knoxville in 2010. He worked with Professor David Mandrus for synthesis of materials and with Dr. Andrew D. Christianson for elastic and inelastic neutron scattering measurements during his PhD research. He completed his PhD in physics in May, 2017 and he is going to begin a postdoctoral research at NCNR, Gaithersburg.